SCREENING SUPPORT MATERIALS for TITANIUM DIOXIDE BASED CATALYSTS for GAS PHASE PHOTOCATALYTIC CO OXIDATION

A THESIS SUBMITTED TO
THE GRADUATE SCHOOL OF NATURAL AND APPLIED SCIENCES
OF
MIDDLE EAST TECHNICAL UNIVERSITY

BY

HANDE KILIÇ

IN PARTIAL FULFILLMENT OF THE REQUIREMENTS
FOR
THE DEGREE OF MASTER OF SCIENCE
IN
CHEMICAL ENGINEERING

JANUARY 2024

Approval of the thesis:

SCREENING SUPPORT MATERIALS for TITANIUM DIOXIDE BASED CATALYSTS for GAS PHASE PHOTOCATALYTIC CO OXIDATION

submitted by **HANDE KILIÇ** in partial fulfillment of the requirements for the degree of **Master of Science in Chemical Engineering, Middle East Technical University** by,

Prof. Dr. Halil Kalıpçılar
Dean, Graduate School of **Natural and Applied Sciences**

Prof. Dr. Pınar Çalık
Head of the Department, **Chemical Engineering**

Prof. Dr. Gürkan Karakaş
Supervisor, **Chemical Engineering Department, METU**

Examining Committee Members:

Prof. Dr. Halil Kalıpçılar
Chemical Engineering Department, METU

Prof. Dr. Gürkan Karakaş
Chemical Engineering Department, METU

Prof. Dr. Yusuf Uludağ
Chemical Engineering Department, METU

Prof. Dr. Ayşen Yılmaz
Chemistry Department, METU

Prof. Dr. Çiğdem Güldür
Chemical Engineering Department, Gazi University

Date: 18.01.2024

I hereby declare that all information in this document has been obtained and presented in accordance with academic rules and ethical conduct. I also declare that, as required by these rules and conduct, I have fully cited and referenced all material and results that are not original to this work.

Name, Last name: Hande, Kılıç

Signature:

ABSTRACT

SCREENING SUPPORT MATERIALS for TITANIUM DIOXIDE BASED CATALYSTS for GAS PHASE PHOTOCATALYTIC CO OXIDATION

Kılıç, Hande
Master of Science, Chemical Engineering
Supervisor: Prof. Dr. Gürkan Karakaş

January 2024, 143 pages

Indoor air quality (IAQ) health concerns have grown in recent decades. CO is one of the main pollutants. The study aimed to assess the photocatalytic activity of a TiO_2-SiO_2 layer synthesized by the sol-gel method on cellulose filter paper for the oxidation of CO at ambient temperature. The catalyst samples were synthesized by depositing a colloidal solution of TiO_2-SiO_2 over fabricated cellulose extraction thimbles. Prior to the synthesis, the fabricated cellulosic extraction thimbles were characterized using TGA and DTA techniques. The TiO_2-SiO_2 layer was characterized using XRD and BET. Alternative substrates, like commercial polypropylene (PP) air filter material and 304 stainless steel wire mesh, were tested. FT-IR spectroscopy was used to test CO gas photocatalytic activity. After the analysis of BET for the PP substrate, it is concluded that PP support has hydrophobic properties, rendering it unsuitable for coating applications. The alternate cellulose filter paper, which is believed to be utilized as a support material for catalyst coating, is notable for its distinctive specific surface area after the BET analysis. Thus, it can be inferred that cellulose support has the capability to be coated, resulting in a significant increase in surface area. The XRD patterns of the coated samples over cellulosic support material revealed that the titania material crystallized in the anatase phase. A recirculated batch reactor system with an FT-IR was established to assess the photocatalytic activity of the produced catalysts. During the photocatalytic activity tests, Using the cellulose filter paper as a support material, an unforeseen rise in CO_2 and CO levels was noticed under UV light. Following the control experiments When exposed to UV light, it may be inferred that the cellulose catalyst support material itself experiences a further rise in CO_2 and CO levels. An alternative support material, 304 stainless steel, resulted in a 30% CO_2 conversion.

Keywords: Photo catalysis, CO Oxidation, Titanium Dioxide, Cellulose Photo Degradation

ÖZ

TITANYUM DIOKSIT TEMELLI KATALIZORLERLE KARBON MONOKSITIN GAZ FAZINDA FOTOKATALITIK OKSIDASYONU ICIN DESTEK MALZEMESI SECIMI

Kılıç, Hande
Yüksek Lisans, Kimya Mühendisliği
Tez Yöneticisi: Prof. Dr. Gürkan Karakaş

Ocak 2024, 143 sayfa

İç mekan hava kalitesi (IAQ) ile ilgili sağlık endişeleri son yıllarda arttı. Bu kapsamda CO de ana kirleticilerden biridir. Çalışma, ortam sıcaklığında CO'nun oksidasyonu için selüloz filtre kağıdı üzerinde sol-gel yöntemiyle sentezlenen TiO_2-SiO_2 katmanının fotokatalitik aktivitesini değerlendirmeyi amaçladı. Katalizör numuneleri, üretilmiş selüloz ekstraksiyon yüksüklerinin üzerine kolloidal bir TiO_2-SiO_2 çözeltisinin biriktirilmesiyle sentezlendi. Sentez öncesinde, üretilen selülozik ekstraksiyon kartuşları TGA ve DTA teknikleri kullanılarak karakterize edildi. TiO_2-SiO_2 katalizörü XRD ve BET kullanılarak karakterize edildi. Ticari polipropilen (PP) hava filtresi malzemesi ve 304 paslanmaz çelik tel örgü gibi alternatif yüzeyler de test edildi. CO gazı fotokatalitik aktivitesini test etmek için FT-IR spektroskopisi kullanıldı. PP substrat için BET analizinin ardından, PP desteğinin hidrofobik özelliklere sahip olduğu ve bu nedenle kaplama uygulamaları için uygun olmadığı sonucuna varıldı. Katalizör kaplama için destek malzemesi olarak kullanıldığı düşünülen alternatif selüloz filtre kağıdı, BET analizi sonrasında selüloz desteğin kaplanabilme özelliğine sahip olduğu ve bunun sonucunda yüzey alanında önemli bir artış sağlandığı sonucuna varılabilir. Kaplanmış numunelerin selülozik destek malzemesi üzerindeki XRD analizleri, titanyum malzemesinin anataz fazında kristalleştiğini ortaya çıkardı. Üretilen katalizörlerin fotokatalitik aktivitesini değerlendirmek için FT-IR' lı yeniden sirkülasyonlu bir kesikli reaktör sistemi kuruldu. Destek malzemesi olarak selüloz filtre kağıdı kullanılarak yapılan fotokatalitik aktivite testleri sırasında, UV ışığı altında CO_2 ve CO seviyelerinde öngörülemeyen bir artış fark edildi. Kontrol deneylerinin ardından UV ışığına maruz bırakıldığında, selüloz katalizör destek malzemesinin kendisinin CO_2 ve CO seviyelerinde daha fazla artış yaşadığı ve bozunduğu sonucu çıkarılabilir. Bu noktadan sonra 304 paslanmaz çelik tel örgü yüzeyine kaplanan katalizör ile yapılan deneyler sonucunda CO_2 dönüşümü %30 olarak tespit edildi.

Anahtar Kelimeler: Fotokatalizör, CO Oksidasyonu, Titanyumdioksit, Selülozun Fotodegredasyonu

To My Beloved Family

ACKNOWLEDGMENTS

The author would like to express her sincere gratitude to her supervisor, Prof. Dr. Gürkan Karakaş, for his invaluable academic advice, direction, insight, and support throughout her studies.

This work is partially funded by Scientific Research Projects Coordination Unit (BAP) under grant number GAP-304-2021-10751.

For their unending love, support, and spiritual and material assistance during the studies, the author owes a great debt of gratitude to her parents, Tülay and Duran Kılıç. The author would also like to express her gratitude to her understanding brother Yiğit Anıl Kılıç for his wonderful company and sense of humor.

The author is indebted to her fellow suffering Ali Gürkan for his irreplaceable friendship, compassionate understanding, and useful contributions to the thesis.

The author is appreciative to her friends Ayşe Tuğçe Onur and Pınar Berberoğlu for their unparalleled support, understanding, and encouragement during the entire process of authoring her thesis.

Finally, the author wishes to express her heartfelt appreciation to Doğaç Çağıl, who has always been a constant source of friendship, tremendous support, and encouragement.

TABLE OF CONTENTS

LIST OF TABLES

TABLES

LIST OF FIGURES

FIGURES

LIST OF ABBREVIATIONS

ABBREVIATIONS

METU Middle East Technical University

CHE Chemical Engineering Department

PCO Photo Catalytic Oxidation

IAQ Indoor Air Quality

SEM Scanning Electron Microscopy

SiO_2 Silicon dioxide (Silica)

TGA Thermogravimetric Analysis

DTA Differential Thermal Analysis

TiO_2 Titanium dioxide

TTIP Titanium Tetra Iso Propoxide

XRD X-Ray Diffraction

BET Brunauer – Emmett – Teller

CHAPTER 1

INTRODUCTION

In the past twenty years, there has been a growing concern regarding the health impacts of poor indoor air quality. The term "indoor air quality" refers to a measurement of the pollutants that are present in the air inside a building, with "pollutants" being defined as toxic chemicals, particles, and biological contaminants. Pollution in the air inside buildings has been linked to several major health problems, including asthma, cardiovascular risks, and sick building syndrome (SBS).

SBS (Sick Building Syndrome) also known as SHS (Sick Home Syndrome), is an illness that can be contracted by breathing in the indoor air. According to the World Health Organization, the first definition includes a group of nonspecific symptoms such as irritation of the nose, eyes, and throat, mental weariness, and dizziness that may have a connection with the occupation of specific workplaces (World Health Organization, Indoor Air Pollutants: Exposure and Health Effects, 1983).

Due to the amount of time spent indoors, indoor air quality (IAQ) plays an essential role in maintaining health and safety. An adult spends the vast bulk of their life indoors. 60% at home, 25% at work, 5% in public, and 5% on public transportation (Watson, 2004).

According to the 2022 World Health Report, approximately 50% of the global population is subjected to indoor air pollution, primarily caused by the combustion of solid fuels (World Health Organization, Reducing Risks, Promoting Healthy Life, 2002).

The guidelines for IAQ had previously been set by the WHO. According to those guidelines, carbon monoxide (CO), formaldehyde, benzene, nitrogen dioxide (NO_2), naphthalene, radon, trichloroethylene, tetrachloroethylene, and polycyclic aromatic hydrocarbons are the pollutants that are selected as those that decrease IAQ and that are typically present in indoor air (World Health Organization, Guidelines for indoor air pollution: Selected Pollutants, 2010).

The quality of the cabins of vehicles used for public transportation is dependent on two major sources, which are referred to as vehicular and non-vehicular sources. In contrast, vehicular sources can be characterized as the emissions of vehicle fuels, which lower the quality of the interior air that is taken in through ventilation. Non-vehicular sources include things like indoor trim, adhesives, and paints, while vehicular sources include emissions from motor fuels. IAQ (in-door air quality) can be managed using one of three approaches: source management, ventilation, or air cleansing. These approaches are applicable to vehicular sources. In most cases, avoiding source control is impossible, particularly in metropolitan areas. Increasing ventilation could be useful, but it is not a viable solution because the air used for ventilation comes from the polluted air outside. The process of purifying the air appears to be the most viable option.

Current air filters that are routinely used for air cleaning are designed to collect various sizes of particles; however, they are often unsuccessful when it comes to the removal of gaseous or vapor phase contaminants as well as certain microorganisms (Zhong , Haghighat, Blondeau, & Kozinski, 2010). For this reason, air filters with catalytic properties that can convert pollutants into non-toxic or less-toxic substances may be an effective solution for improving the indoor air quality of public transit vehicles.

Particulate materials, such as aerosols, dirt, and dust, which are reducible to 99% with hepafilters, and gaseous pollutants, such as CO, VOCs, and NOx, which are promising in new technologies, are examples of the pollutants that can be found in ventilation air (Tartakovsky, et al., 2013).

Oxidation (for example, of CO and VOC) and reduction (for example, of NO_x) of those gaseous pollutants is the method that was very recently created to get rid of them. It's possible that thermal or catalytic processes will be used to accomplish the oxidation.

The gas phase thermal oxidation reaction of CO not only requires adequate combustible reactants (CO and O_2), but it must also maintain the flammability limit of the reactants, which is stated to be 12.2% for CO and 72.5% for O_2, which corresponds to higher concentrations than its hazardous level.

Elevated temperatures and an adequate amount of retention time are necessary for the thermal oxidation of volatile organic compounds (VOCs). requiring a retention period of 0.5 to 1 second to form bonds between molecules of oxygen and volatile organic compounds (VOCs). To achieve the thermal oxidation of volatile organic compounds (VOCs) into model molecules, the combustion chamber temperature needs to be maintained between 725 and 825°C.

Therefore, the thermal oxidation of CO and VOCs needs to take place at extremely elevated temperatures to overcome the activation energy of the reaction. This is true even if one disregards the other downsides. It's possible that the high-temperature exhaust gas could be used to preheat the converter. In this method, expenditures associated with the input of energy could be decreased.

Catalytic oxidation is another method that may be used, and it helps cut down on operational costs by lowering the amount of activation energy required and the reaction temperature substantially. During catalytic oxidation, the catalyst makes it possible for reactions to happen faster in a smaller volume. This cuts both the cost and the time needed.

In the literature, a variety of catalysts are employed for CO oxidation. The most popular are the reducible metal oxides MO_y (M = Cu, Zn, Co, and Fe) supported on inert oxides such as TiO_2, ZrO_2, SiO_2, CeO_2, etc. A noble metal (e.g., Pt, Au, Pd, etc.) spread across a reducible metal oxide gains relevance due to the positive effects they have on the reaction process.

Research conducted by Mirkelamoglu et al. studied the oxidation of carbon monoxide over palladium and sodium-promoted tin dioxide. The sol–gel technique was used to produce catalysts with compositions of 0.1 wt.% Na, 1 wt.% PdO/ SnO_2 and 1 wt.% PdO/ SnO_2 with a weight of 1%. Tin dioxide was found to have high-temperature CO oxidation activity, which occurred at temperatures higher than 250°C. It was shown that promotion by alkali and noble metals had a beneficial effect on operating temperature and reduced activation energy significantly (Mirkelamoglu & Karakas, 2006).

Volatile organic compounds (VOCs) are a significant category of air pollutants that are released into the atmosphere by various industrial operations and transportation activities. Catalytic oxidation is a highly advanced method employed for the removal of volatile organic compounds (VOCs) due to its ability to operate at lower temperatures compared to thermal oxidation. The primary catalysts used for VOC oxidation are typically noble metals, which exhibit excellent performance at moderate temperatures. However, these catalysts are expensive and exhibit poor stability when exposed to chloride compounds. Metal oxides such as iron (Fe), chromium (Cr), copper (Cu), manganese (Mn), and cobalt (Co) offer a more cost-effective option compared to precious metals when used as catalysts for volatile organic compound (VOC) oxidation. They have adequate activity, albeit less than noble metals, particularly at low temperatures (Delimaris & Ioannides, 2009).

As a result, both thermal and catalytic oxidation have restrictions, as thermal oxidation for CO and VOC oxidation requires temperatures greater than 600 and 800 °C, respectively, and has the mentioned limitations. Therefore, it will be useless for air purification needs. The catalytic oxidation, on the other hand, massively reduces the temperature requirements to those necessary for purifying automotive exhaust gases. As a result, room-temperature photocatalytic oxidation, a novel and promising option that is viable at low temperatures, was recently proposed to meet indoor air quality criteria. Consequently, room-temperature photocatalytic oxidation is a novel and promising method for combating indoor air pollution (PCO). The objective of this work was to evaluate the photocatalytic efficiency of a TiO_2-SiO_2 layer synthesized by the sol-gel technique over cellulose filter paper for the Co room temperature photo oxidation. The catalyst samples were synthesized by a colloidal solution of TiO_2-SiO_2 over fabricated cellulose extraction thimbles. Before the synthesis, the cellulosic extraction thimbles were analyzed using TGA (Thermogravimetric Analysis) and DTA (Differential Thermal Analysis) techniques. The deposited layer of TiO_2-SiO_2 was analyzed using X-ray diffraction (XRD) and Brunauer-Emmett-Teller (BET) techniques. The experiments were also conducted using commercial polypropylene (PP) air filter material and 304 stainless steel wire mesh as alternate substrates. Photocatalytic activity tests for the CO gas pollutant were conducted using FT-IR spectroscopy.

CHAPTER 2

LITERATURE SURVEY

2.1 Photocatalysis

Photocatalysts are materials that overcome the activation energy of a reaction by utilizing "photons" rather than other forms of energy, and they can vary the rate at which chemical reactions take place when they are exposed to light. Semiconductors absorb light and have been shown to be effective photocatalysts due to their suitable band gap structure.

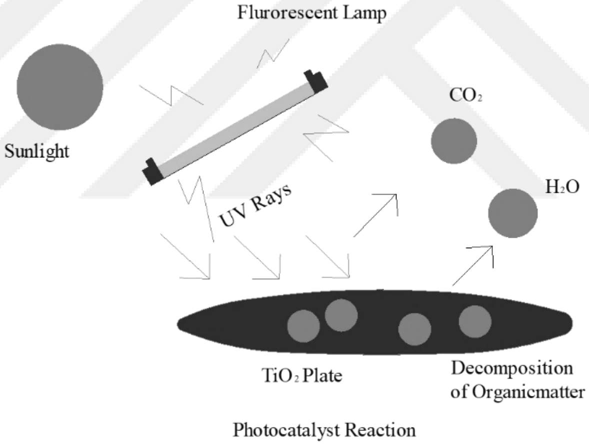

Figure 2.1 Concept of a Photocatalytic Reaction

The "conduction band" is defined as the range of electron energies sufficient to release an electron from its binding with its atom, allowing it to move freely within the atomic lattice of the material as a "delocalized electron." The "valence band" refers to the highest range of electron energies where electrons are normally present at absolute zero temperature. The "valence band" refers to the highest range of electron energies where electrons are normally present at absolute zero temperature.

Figure 2.2 depicts the schematic figure of those definitions.

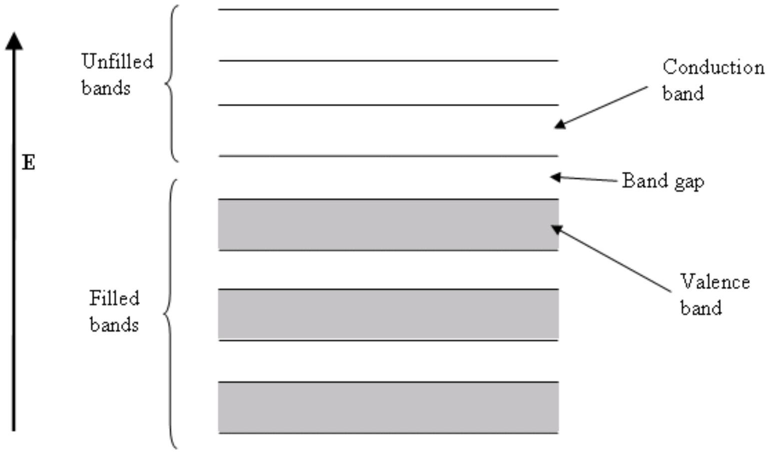

Figure 2.2 Band Gap Visual Basis

The difference in energy levels between a material's valence and conduction bands is called the band gap, and it can be used to classify semiconductor materials.

The band gap is often quite narrow in semiconductors. Because the photon energy supplied by a light source is greater than the band gap, pairs of electron holes are generated in the semiconductor. Because the charge will transfer between electron-hole pairs and adsorbed species (reactants) on the semi-conductor surface, the process of photooxidation takes place (Zhao & Yahn, 2003).

Semiconductors can be excited by light that has more energy than the band gap.

, which results in the formation of an electron–hole pair with a high amount of energy. Pure or doped semiconductors are typically utilized to create a photocatalyst for use in photocatalytic reactions. Metal oxides are compounds formed by the combination of a metal element with oxygen. These oxides exhibit a wide range of properties, depending on the specific metal and its oxidation state. Some metal oxides, particularly transition metal oxides, are known for their interesting semiconductor properties. The semiconducting properties of metal oxides arise from the interaction between the metal cations and oxygen anions in the crystal lattice.

The electronic structure of metal oxides allows them to have a band gap – a range of energy levels that electrons cannot occupy. This band gap determines the material's conductivity. The excitation of electrons in the valence band of the metal oxide (MO) is a significant stage in the photoreaction process. This is followed by the formation of free electrons and holes (e^- and h^+) with energy from the conduction band. As was indicated earlier, charge separation requires a specific amount of activation energy, which must be defeated by the energy of UV photons.

$$MO + h\nu \longrightarrow e^- + h^+ \quad (1)$$

Diffusion is the process that allows electrons and holes to transfer their charges to the surface of a particle. Charge carrier density and the mobility of the solid matrix are two of the most critical criteria that need to be considered to successfully transport electrons and holes. Recombination of the electron and the hole is caused by the lower mobility that results from faults and defects in the material. Charge separation, transport, and recombination rates of electrons and holes are the major factors that determine the photon efficiency of photocatalysts.

The absorbents of the ambient molecules (which in this case will be pollutants) that are capable of being absorbed by chemisorption or physisorption could react with the perfectly transmitted electron and hole pair over the metal oxide's surface. After that, free radicals will be formed because of the interaction of ad species and surface charges (electrons and holes). The photocatalytic reactions primarily consist of oxidation and reduction (also known as redox) reactions taking place by free radical mechanisms.

The charge pairs that exist on the surface of metal oxide react with absorbed oxygen and OH-ions that are originated from ambient humid air over the catalyst surface, and the following reactions take place.

$$O_2 - S + e^- \longrightarrow O_2^- - S \text{ Reduction of Oxygen } (2)$$

$$OH^- - S + h^+ \longrightarrow OH\cdot - S \text{ Oxidation by Hydroxide Ion } (3)$$

$$OH\bullet\text{-}S + OH\bullet\text{-}S \longrightarrow H_2O_2 - S$$ Reaction Between Hydroxyl Radicals (4)

The impurities and defects in the structure of a metal oxide prevent a continuous pathway from reaching the surface of the metal oxide pairs. This is because the impurities and defects are in the structure of the metal oxide. Because of this, they merged, causing a process known as charge recombination, which resulted in the release of heat (Li, Liu, Cai, Zhang, & Wang, 2010).

$$e^- + h^+ \longrightarrow \text{heat} \quad (5)$$

Metal oxides are known for their photocatalytic properties, and they have been extensively studied and employed in various applications, particularly in the fields of environmental remediation and energy conversion. Some of the notable metal oxides with photocatalytic properties include titanium dioxide (TiO_2), zinc oxide (ZnO), and tungsten trioxide (WO_3). Various other metal oxides, such as iron oxide (Fe_2O_3), cerium oxide (CeO_2), and others, also exhibit photocatalytic properties to varying extents.

The choice of metal oxide depends on factors such as band gap, stability, and suitability for specific applications.

The band gap has a direct relationship with the wavelength of light energy that is absorbed by the material. The band locations of a variety of semiconductors, together with certain chosen redox potentials, are depicted in Figure 2.3. Due to the fact that semiconductor metal oxides have a narrow band gap, they are able to absorb low-energy photons in the solar spectrum that have a long wavelength (Wang, Ang, & Tade, 2007).

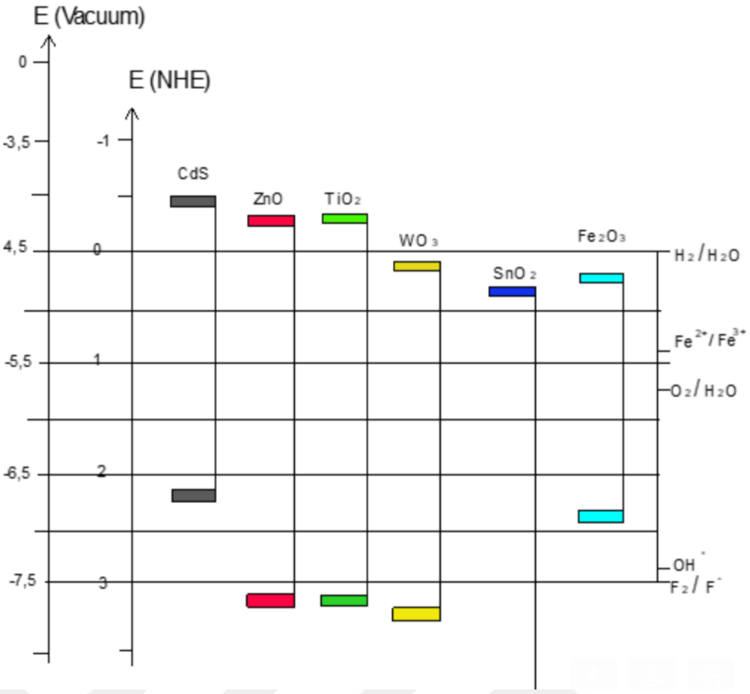

Figure 2.3 Band Positions of Several Semi-Conductors

(Top represents CB, bottom represents VB)

The band gap energy for anatase TiO_2 is approximately 3,2 eV, corresponding to a wavelength of around 387.5 nm. This means that anatase TiO_2 can absorb light with wavelengths shorter than 387.5 nm, primarily in the UV region, and the absorption edge extends into the visible range, but most of the absorption occurs in the UV range. The photocatalytic reaction is expressed as follows.

$$TiO_2 + h\nu \longrightarrow h^+ + e^- \quad (6)$$

In this reaction, h^+ and e^- have strong oxidation and reduction potential. TiO_2 is currently the catalyst that has been subjected to the most research for the photocatalytic reaction due to its acceptable band gap of 3,2 eV. For TiO_2 to be excited by light, the required wavelength is 388 nm, which is in the ultraviolet (UV) region (Wang, Ang, & Tade, 2007).

2.2 TiO$_2$ Based Photocatalysts

Anatase, rutile, and brookite are the three primary types of crystal structures that can be found in titanium oxide (Figure 2.4). The distortion of each octahedral and the assembly patterns of the octahedral chains are two aspects that differentiate the three different crystal formations. It is possible to think of anatase as being constructed from octahedral that are connected at their vertices; rutile has connections at its edges; and brookite has connections at both its vertices and its edges (Carp, Huisman, & Reller, 2004).

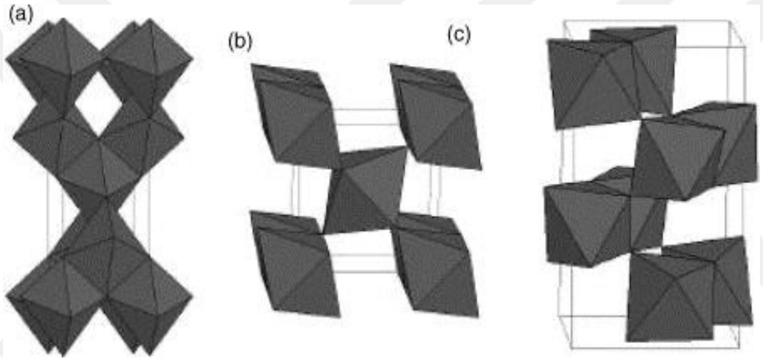

Figure 2.4 Crystal structures of anatase (a), rutile (b), and brookite (c)

Titanium dioxide (TiO$_2$) is a widely used photocatalyst with diverse applications, particularly in environmental remediation and renewable energy production. Some notable uses of TiO$_2$ photocatalysis are water splitting, degradation of organic pollutants, photocatalytic disinfection, photocatalytic reduction of carbon dioxide, self-cleaning surfaces, hydrogen production, and air purification (CO, NOx, VOC, and CO$_2$ reduction). This thesis scope is for CO oxidation.

2.3 Steps of Photocatalytic Reaction of TiO$_2$

The initial stage of heterogeneous photocatalytic processes involves the generation of electron-hole pairs through the absorption of photons by TiO$_2$, provided that the photons possess energy levels exceeding the energy band gap.

$$TiO_2 + \text{photon } (h\upsilon) \rightarrow TiO_2\ (h^+ + e^-)\ (7)$$

The created holes react with the electron of the adsorbate e.g., surface hydroxyl groups.

$$h^+ + RX_{ads} \rightarrow RX^+_{ads}\ (8)$$

$$h^+ + H_2O_{ads} \rightarrow \bullet OH\ _{ads} + H^+\ (9)$$

$$h^+ + OH^-_{ads} \rightarrow \bullet OH\ _{ads}\ (10)$$

The generated electrons are transferred to the adsorbed electron acceptor e.g., molecular oxygen.

$$O_{ads} + e^- \rightarrow O^-_{ads}\ (11)$$

$$e^- + O_2 \rightarrow O_2^-\ (12)$$

The subsequent stages, known as electron transfer processes, hold the most importance since they generate the major oxidant radicals. The superoxide anion can proceed with the reaction in an aqueous phase and produce hydrogen peroxide, a highly oxidizing chemical. The process of photoconversion of hydrogen peroxide also results in the formation of hydroxyl radicals (•OH).

$$H^+ + O_2^- \rightarrow \bullet HO_2\ (13)$$

$$H^+ + O_2^- + \bullet HO_2 \rightarrow H_2O_2 + O_2\ (14)$$

$$H_2O_2 + h\upsilon \rightarrow 2\ \bullet OH\ _{ads}\ (15)$$

The hydroxyl radicals and superoxide anions are highly reactive species for oxidizing adsorbed organic pollutants. These radicals oxidize the organic compounds, while reduction processes and the chain reaction, launched by light absorption, ended (Kirbas, 2014).

Electron-hole recombination can take place prior to the transfer to the particle's surface because of lattice defects, impurities, and imperfections. Additionally, the lack of electron scavengers (O_2 and H_2O) can cause the recombination of electrons and holes rather than photocatalytic chain reactions. Thus, the recombination of electron and hole decreases the activity of the photocatalyst (Grela, Coronel, & Colussi, 1996).

2.4 CO Photocatalytic Oxidation

Photocatalytic materials serve as a framework or structure to bolster and optimize the efficacy of photocatalysts in photocatalytic reactions. Photocatalysis is a process that utilizes a catalyst and light to initiate and propel chemical processes. Photocatalytic materials have the capacity to impact the catalytic activity, stability, and efficiency of the photocatalyst. Gas-phase oxidation in photocatalysts uses materials that can utilize light energy to enhance oxidation reactions in the gas phase. Various photocatalytic materials can enhance the catalytic activity of catalysts when they are employed to oxidize carbon monoxide (CO) in the gas phase. The choice of a particular support material is often determined by the desired characteristics and intended use of the photocatalyst. For the purposes of this thesis, a TiO_2 photocatalyst has been selected for CO photocatalytic oxidation.

2.4.1 CO Photocatalytic Oxidation over TiO_2 Photocatalyst

As was discussed in the earlier sections, due to the exceptional qualities that TiO_2 possesses as a semiconductor, it has been the subject of a significant amount of research for CO degradation. The photocatalytic oxidation of CO with TiO_2 offers several advantages in the presence of UV light, including the fact that it can take place at room temperature, and atmospheric pressure, and without the addition of any heat source. These heterogeneous reactions’ product is carbon dioxide (CO_2).

The photocatalytic oxidation of carbon monoxide (CO) into carbon dioxide (CO_2) with oxidants such as nitrogen oxides (NO), nitrogen dioxide oxides (N_2O), and oxygen (O_2) occurred efficiently on a Mo/ SiO_2 with a high molybdenum dispersion when exposed to ultraviolet light. This reaction was shown to work well on Mo/ SiO_2 with a high CO conversion rate of 100% and CO selectivity of 99% after 180 min of

UV light irradiation, showing that it is a better photocatalyst than TiO_2 (P25) (Kamagewa, Takeuchi, Matsuoka, & Anpo, 2006).

Metal oxide catalysts, particularly those based on TiO_2, are frequently used to promote the catalytic oxidation of CO to CO_2. Moretti et al, studied a set of CuO-ZnO/ TiO_2 ternary catalysts synthesized using co-precipitation and subsequently analyzed using X-ray powder diffraction (XRPD), N_2 physisorption at 77 K, temperature-programmed reduction/oxidation (H_2-TPR/TPO), and FT-IR studies of low-temperature adsorbed CO. The catalysts underwent testing and were determined to be effective in the selective oxidation of CO (CO-PROX) in gas streams with high hydrogen content. Their catalytic performance was then compared to that of the binary systems CuO/ZnO and CuO/TiO_2. The catalysts composed of CuO-ZnO on TiO_2 exhibited significant CO conversion rates and demonstrated complete selectivity towards CO oxidation within the temperature range of 65–120°C, which is of significant importance in technology. The most optimal sample among the investigated CuO-ZnO/TiO_2 ternary systems was $Cu_{17}Zn_{46}Ti_{37}$. This sample had a weight ratio of CuO/ZnO = 0,36 and CuO/TiO_2 = 0,46. It exhibited a Tconv 50% of 110 8C and achieved 100% selectivity towards CO_2. In addition, the catalyst exhibited long-term stability for a duration of 90 hours, even in the presence of 15 volume percent of carbon dioxide (CO_2). The Cu/Zn/Ti ternary oxide catalysts exhibit characteristics of a synergistically interacting electronic system, with Zn and Ti oxide exerting a noteworthy influence on the chemical properties and stability of the copper species. The catalytic performances of the material are determined by the intimate interaction, which seems to be dependent on the oxide molar ratios. Titania exhibits a preference for reducing Cu^{2+} in CO-PROX conditions and stabilizing its reduced forms. On the other hand, ZnO, due to its basic nature, enables the presence of Cu^{+} species on the catalyst surface (Moretti, et al., 2008).

It is probable that the noble metal-doped catalysts will bring the temperature down, allowing the oxidation to take place at room temperature.

Pt is another example of a noble metal that finds widespread application in the photocatalytic destruction of CO. A typical platinum loading of ~3% was achieved with photo deposition directly on a glass plate that had been coated with TiO_2. Platinum deposition on TiO_2 significantly increased the photooxidation rate of carbon monoxide (CO) in the concentration range of 30–500 ppmv, in contrast to the much slower oxidation rates observed by naked TiO_2 samples. In the presence of oxygen, the rate at which CO_2 is produced via photosynthesis is quantifiable. There is a strong relationship between the PCO rates and the amounts of Pt that are deposited on TiO_2. The size of the Pt particles that were deposited in this investigation is on the order of a few nanometers, and some of the Pt/ TiO_2 samples show appreciable activity for CO oxidation even when the conditions are dark (Hwang, Lee, & Choi, 2013).

In addition, the photocatalytic activity of TiO_2 and SiO_2/ TiO_2 with Pd doping is investigated for its ability to oxidize CO. At room temperature, 0,1wt% Pd doped equivalents are put through their paces for research. With a rate constant of 0,063 $s^{-1}g_{cat}^{-1}$, it was found that a sample containing 80% SiO_2/ TiO_2 exhibited the maximum photocatalytic activity. Because increasing Ti=2 loading reduces the surface area, the CO adsorption rate drops when the loading level is increased. The photooxidation activities, on the other hand, are increased when the SiO_2 ratio is increased. Because of this, Pd doping was shown to be beneficial in creating efficient catalysts for the oxidation of CO at room temperature (Yetisemeyen, 2010).

The effect of calcination and reduction treatment on the photocatalytic activity of carbon monoxide oxidation on Pt/ TiO_2 was investigated by Zhang et al. According to the findings, the best temperature for calcination of CO photocatalytic activity was found to be 673 K over a period of two hours in air. A higher temperature was found to be detrimental to the process of increasing CO photocatalytic activity. At a temperature of 773 K, a reduction in the atmosphere's concentration of hydrogen dioxide can help restore the lost photocatalytic activity of CO oxidation (Zhang, Jin, Zhang, Zhanh, & Dang, 2005).

2.5 Substrate Materials for TiO_2 Photocatalyst

Numerous studies have widely investigated the utilization of TiO_2 as a photocatalyst on various substrates for the purpose of photocatalytic oxidation. Titanium dioxide (TiO_2) is a highly versatile photocatalyst acclaimed for its capacity to promote oxidation reactions upon exposure to light, particularly ultraviolet (UV) radiation. Here is a summary of the applications of TiO_2 photocatalyst on various substrates for the purpose of photocatalytic oxidation.

- Filter Paper Substrates
- Metal Substrates (Aluminum, Stainless Steel): The applications are usually referred to as outdoor surfaces, building facades, and air purification.
- Concrete and Cementitious Materials: The applications usually refer to facades, construction materials, and outdoor surfaces.
- Polymeric Materials (Plastics, Polymers): Applications for these surfaces are usually antimicrobial coatings, air purification, and self-cleaning plastics.
- Textiles and Fabrics: Applications include self-cleaning fabrics and antimicrobial textiles.
- Glass Surfaces: The applications usually refer to self-cleaning windows and glass surfaces.
- Ceramic Surfaces
- Foam Ni Substrates

In this study, PP Commercial Filter Paper, fabricated cellulosic extraction thimbles, and 304 stainless steel wire mesh were used as alternative substrates for CO photocatalytic oxidation with TiO_2-SiO_2 photocatalyst under UV irradiation.

2.5.1 Studies with Filter Paper Substrate Materials

The photocatalytic activity of a photocatalyst-coated filter paper measuring 4,5 cm by 13 cm was measured at ethanol concentrations ranging from 50 to 200 mg per cubic meter (Model VOC). The "Rapid Khoten" process was utilized in the production of paper sheets with different base weights (60, 100, and 200 g m^{-2}) These paper sheets measured 20 cm in diameter. In a continuous gas-flow reactor made of stainless steel, research was conducted on the photocatalytic performance of papers loaded with TiO_2/ SiO_2 (diameter, 22 mm; volume, 10 mL). The tests for both stability and activity have been carried out, and the results have been compared to those of a commercial paper. As a consequence of this, the ideal photocatalytic performance of the silica-titania paper sheet has been demonstrated in the room-temperature degradation of ethanol, attaining a competitive activity of as high as 3.86 mg TiO_2^{-1} min^{-1} with an incidence intensity of 14.4 mW cm^{-2} in the process (Adjimi, et al., 2014).

Gao et al. conducted research on a composite thin film made of super hydrophobic TiO_2/ EP (Amorphous Titanium Dioxide and Epoxy Resin). It was possible to create filter paper with super hydrophobicity by adhering a micro/nano structure of amorphous titanium dioxide to the surface of the filter paper using a material with low surface energy. The structure of the super-hydrophobic thin film that is applied to the surface of the filter paper is exceptionally stable as a result of the coupling agent (KH 550), which is an essential component in the bonding process that involves amorphous titanium dioxide and epoxy resin. The results of the observations indicated that the wettability of the filter paper samples changed from super-hydrophilicity to super-hydrophobicity when the water contact angle was 153 ± 1^{o}. The effects of water–oil separation and UV-resistance provided by the super-hydrophobic filter paper were also the focus of some of the experiments that were designed. After the experiments, the pre-prepared super-hydrophobic filter paper functioned effectively and easily in water–oil separation while also maintaining its anti-UV property for an extended period of time. The utilization of super-hydrophobic filter paper in practical settings is made possible through the utilization of this method. The procedure for the experiment is outlined below**.** Simply dipping filter paper in a solution containing amorphous titanium dioxide and an epoxy resin dissolved in acetone with OTS (octadecyl trichlorosilane) hydrophobization was all that was required to successfully create super-hydrophobic filter paper. The ultra-oleophilic filter paper exhibited remarkable chemical stability and resistance to UV rays, in addition to its remarkable super-hydrophobicity and super-oleophilicity. KH-550 was utilized for the very first time to bridge amorphous titanium dioxide and epoxy resin to improve the dimensional stability of super-hydrophobic filter paper (Gaoa, et al., 2015).

Huang et al. conducted their research on a sticky super hydrophobic filter paper that was created by dip-coating with a fluorinated waterborne epoxy emulsion. Based on a waterborne bisphenol-A novolac epoxy emulsion, a coating that is both extremely hydrophobic and oleophilic was fabricated for use in oil filter paper. To impart hydrophilic groups (carboxyl) and C-C double bonds onto the epoxy resin, modification agents in the form of benzoic acid (BA) and maleic anhydride (MA) were utilized. In addition, the free radical solution polymerization of dodecafluoroheptyl methacrylate (DFMA) monomer was utilized to produce the fluorinated waterborne epoxy emulsion. The covalently bound fluorinated chains in the monomer have a low free energy, which causes the surface energy of the solidification polymers to be sufficiently reduced. This results in the polymers exhibiting superhydrophobic behavior while maintaining their super-oleophilic nature. Surfaces that have been prepared have a sticky quality that demonstrates a static water contact angle of 152° for a 5μL droplet and does not allow the sample to slide off even when it is held in an inverted position. As an impregnating agent for filter paper, this synthetic emulsion is not only easy to use but also very convenient. A super-hydrophobic and super-oleophilic filter paper was fabricated for the separation of oil and water. The combination of low-free-energy fluorinated chains with the rough structure of the filter paper enhances the non-wetting of water while keeping the intrinsic wetting of oil, leading to super-hydrophobicity and superoleophobicity. Compared with the methods reported recently, the method in this paper is comparatively economic, facile, and timesaving. It can be readily realized without special equipment, reagents, or complex process control. Moreover, this method is versatile for substrates that can bear elevated temperature (Huang, Wen, Cheng, & Yang, 2012).

TiO_2 nanobelt-based materials were researched by Wang et al. TiO_2 nanobelt-based materials, such as TiO_2 nanobelts, acid-corroded (AC) TiO_2 nanobelts, and their silver-loaded products, known as Ag/ TiO_2 nanobelt and Ag/ AC TiO_2 nanobelt, were used as fillers to make cellulose-based composite papers having photocatalytic activity and antibacterial effects. Acid-corroded TiO_2 nanobelts that have been corroded by acid (referred to as AC TiO_2 nanobelts) were synthesized using an acid-assisted hydrothermal method. These materials, which included TiO_2 nanobelts, acid-corroded (AC) TiO_2 nanobelts, and their silver-loaded products, denoted respectively by Ag/ TiO_2 nanobelt and Ag/ AC TiO_2 nanobelt, were used as fillers to prepare cellulose-based composite papers with photocatalytic activity and antibacterial effects. In this hybrid structure, cellulose fibers retain the basic structure and physical and chemical properties of traditional paper, TiO_2 nanobelts play a key role in endowing photocatalysis properties for the paper, and silver nanoparticles give the paper an antibacterial property. The paper’s photocatalytic degradation effect on Methyl Orange (MO) solution and stability in repeated use were enhanced by increasing the mass fraction of TiO_2 nanobelts in the paper. The highest Methyl Orange degradation property is found in paper that contains 40 wt% of TiO_2 nanobelts, and the ratio of Methyl Orange in solution that is degraded after 4 hours of exposure to a 30 W UV lamp is getting close to 100%. The photocatalytic activity of the paper contains 40% TiO_2 nanobelt was maintained after three runs of repeated application. The hybrid paper-based photocatalyst's stability can be decreased because of acid's ability to cause surface corrosion of TiO_2 nanobelts, which paradoxically can improve the photocatalytic property. Paper's capacity for photocatalysis and its ability to inhibit the growth of microorganisms are both enhanced when silver particles are loaded onto the surfaces of TiO_2 nanobelts. After 2 hours, the photocatalytic degradation can be observed (Wang, et al., 2012).

2.5.2 Studies with Metal Substrates

Ivanova et al. worked on the photocatalytic efficiency of TiO_2, which was fixed onto three distinct metal substrates (stainless steel, copper, and titanium), was examined by employing dichloroacetic acid (DCA) and oxalic acid (OA) as representative compounds. The immobilization of TiO_2 was achieved by a unique approach known as Cold Spraying. The photocatalytic degradation tests were conducted in two cycles on each TiO_2-coated metal substrate. In the first cycle, either OA or DCA acid was degraded, while in the second cycle, the acid that was not employed in the first cycle was deteriorated. The HSU CGT Kinetics 8000 prototype was utilized to conduct Cold Spraying. Nitrogen was employed as the process gas, along with a standard type 24 WC-Co nozzle and the PF4000 powder feeder from CGT, Amping, Germany. The powder feed rate remained consistent at 0.22 g/s, while the traverse speed of the spray cannon was held steady at 320 mm/s. The TiO_2 coatings were Cold sprayed using process conditions of a gas temperature of 800 ℃ and a gas pressure of 4 MPa. The substrates were secured at a distance of 60 mm. The TiO_2 coatings were achieved with a single pass of cold spraying. The photocatalytic degradation of the two model compounds, namely OA and DCA, on metal substrates coated with TiO_2 shown that OA can be more effectively destroyed through photocatalysis compared to DCA. Additionally, using OA after a first cycle with DCA aids in the restoration of the surface. Copper, when used as a substrate material, was discovered to be photochemically active, resulting in the production of basic species that are discharged into the aqueous system. Stainless steel and titanium are more appropriate substrate materials for photocatalytic environmental applications (Ivanova, et al., 2013).

Shang et al. studied the high photocatalytic activities of TiO_2 films (50–360 nm) on a stainless steel webnet by the sol–gel method. The stainless steel webnet was chosen as a catalyst support due to its malleability for engineering purposes and its ability to withstand different forms of corrosion. Moreover, the extensive surface area of the stainless steel webnet allows for a greater number of active sites where TiO_2 can be deposited compared to typical supports. During the experiment, a 60-mesh stainless steel webnet was initially washed with 0.1M hydrochloric acid and then with distilled water. Next, a pre-dried stainless steel webnet measuring 16 cm × 10,5 cm was immersed in the sol for 10 seconds and subsequently spun at a high velocity to create a wet gel layer. Following the drying process at a temperature of 80 ℃, the substrate that had been coated with a TiO_2 dry-gel film was then subjected to a heating process at a rate of 5 ℃ per minute until it reached a temperature of 400 ℃. Subsequently, it was calcined at 400 ℃ for a duration of 10 minutes in an oven with an air. The thickness of the TiO_2 layer was controlled by iteratively immersing it and subjecting it to heat treatment. The TiO_2 films underwent 1-4 cycles, with corresponding thicknesses of 50, 140, 250, and 360 nm. As the thickness of the TiO_2 film increased, the diffusion of the substrate was limited from the surface, resulting in the formation of a more flawless crystallization of the TiO_2 film. The enhanced photocatalytic activity of the TiO_2 film was attributed to its increased thickness and improved crystallization. This was assessed by measuring the efficiency of photocatalytic oxidation of gaseous formaldehyde in a cylindrically flowing photoreactor. Once the thickness of the TiO_2 layer surpasses around 250 nm, its photocatalytic activity remains constant. This suggests that the photocatalytic process was exclusively influenced by a certain thickness of the TiO_2 sheet (Shang, Li, & Zhu, 2003).

2.6 CO Photocatalytic Oxidation Reaction Kinetics with TiO_2 Catalysts

The photocatalytic oxidation of carbon monoxide (CO) with titanium dioxide (TiO_2) entails a series of complex reactions. The kinetics of TiO_2-based photocatalysis can be described by the Langmuir-Hinshelwood (L-H) kinetic model, a widely employed framework for heterogeneous photocatalytic processes. In the Langmuir-Hinshelwood model, it is assumed that the reactants (CO in this study) undergo adsorption onto the surface of the photocatalyst prior to the occurrence of the reaction.

The adsorption isotherms of the TiO_2 photo catalyst could be well fitted with the Langmuir Model, whereas the photo catalytic oxidation rate of the pollutants could be described by the Langmuir Hinshelwood Model (Jinze, Zhu, & Burda, 2014).

The models described below.

$$\text{Langmuir isotherm :} \quad q_{\mathrm{e}} = \frac{q_{\mathrm{m}} b C_{\mathrm{e}}}{1 + b C_{\mathrm{e}}}$$

$$\text{Langmuir–Hinshelwood rate law :} \quad r_0 = \frac{kKC_0}{1 + KC_0}$$

- qe: Amount of the adsorbed pollutant
- qm: Maximal adsorbance capacity of the medium
- b: Equilibrium adsorption constant
- Ce: Equilibrium concentration
- ro: Pollutant degradation rate
- k: Reaction kinetic constant
- K: Equilibrium adsorption constant
- Co: Initial Pollutant Concentration

CHAPTER 3

EXPERIMENTAL

In this study, the photocatalytic activity of sol gel synthesized TiO_2-SiO_2 layer over cellulosic filter paper was evaluated for a room-temperature CO oxidation reaction. The catalyst samples were synthesized by using a colloidal solution of TiO_2-SiO_2, which was deposited over fabricated cellulosic extraction thimbles. Before the synthesis, the fabricated cellulosic extraction thimbles were characterized by TGA and DTA techniques. The characterizations of the TiO_2-SiO_2-deposited layer were conducted using XRD and BET techniques. The experiments were also conducted using commercial PP (polypropylene) air filter material and 304 stainless steel wire mash as substrates. The photocatalytic activity tests were conducted by FT-IR spectroscopy for the CO gas pollutant. The experimental work done can be arranged as follows:

- Catalyst Synthesis
- Preparation of the Catalyst Filter Papers
- Substrates and Catalyst Characterization
- Photocatalytic Activity

3.1 Catalyst Synthesis

3.1.1 Materials for The Catalyst Synthesis

The chemicals used for the synthesis of the colloidal catalyst solution are listed as:

- Precursor: Titanium (IV) isopropoxide [TTIP, $C_{12}H_{28}O_4Ti$, 97%] by Aldrich (CAS Number: 546-68-9)

- Catalyst: Acetic acid [Glacial acetic acid, CH_3CO_2H, 99.8-100.5%] by Sigma-Aldrich (CAS Number: 64-19-7)
- Support Material: LUDOX SM-30 colloidal silica [SiO_2, 30 wt. % suspension in H_2O] by Aldrich (CAS Number: 7631-86-9)
- DI Water by METU CHE Laboratories

3.1.2 Substrates for The Catalyst Coating

The substrates used for the synthesis of the colloidal catalyst solution are listed as:

- Commercial PP Filter Paper
- Cellulose Extraction Thimbles 30*80mm by Filter-LAB
- 304 Stainless Steel Wire Mesh (300mesh; 45µm) – 7,5*2,2 cm each

3.1.3 Pretreatment of The Substrates

The cellulose extraction thimbles and the commercial PP filter are used without any pretreatment.

The pretreatment of the 304 stainless steel wire mesh substrate is established with an alkali pretreatment. The wire mesh samples were washed out with distilled water and immersed in a 0.01M KOH solution for 1 hour. After the etching process, the substrates were rinsed with DI H_2O until the ultimate PH reached 7. Then the substrates dried at 100 °C for 1 hour.

3.1.4 Synthesis of The Sol-Gel Colloidal Solution

The sol-gel synthesis method was used to prepare a TiO_2-SiO_2 colloidal solution (Brinker & Scherer, 1990). For this purpose, 30 ml of Ti (IV) isopropoxide was poured into 60 ml of acetic acid by dropwise and continuous stirring of precursor and acetic acid. To prepare the titania-silica mixed oxide nanoparticles, LUDOX was used as silica precursor. The ratio of TiO_2/SiO_2 by mole was selected as 0,5 and the proper amount of H_2O in silica suspension was calculated. After two hours of continuous stirring of precursor and acetic acid, a 21,7 ml of deionized H_2O and 8,3 ml of LUDOX was added very slowly in the mixture and the forming colloidal solution left on the magnetic stirrer for 24h to complete reaction. The final clear solution was used for the substrate coating by a dip coating method.

The process reaction is given as:

$$Ti(OCH(CH_3)_2)_4 + 2H_2O \rightarrow TiO_2 + 4(CH_3)_2CHOH \quad (16)$$

The final clear solution was used for the substrate coating by a dip coating method.

The summary of one of the procedures is shown below in Figure 3.1.

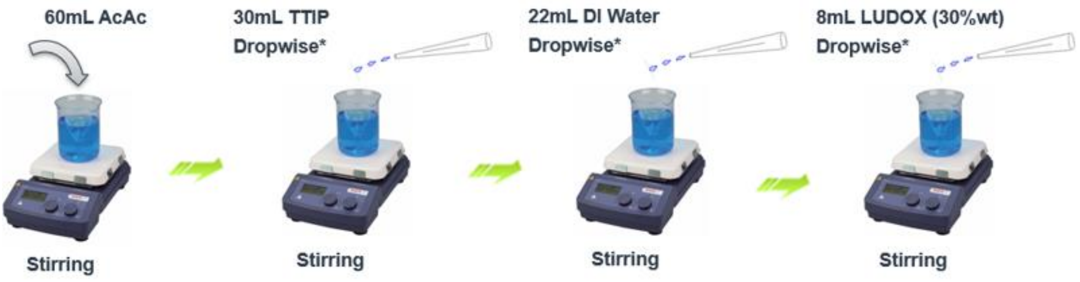

Figure 3.1 Synthesis of The Sol-Gel Solution

3.2 Preparation of The Catalyst Films on Substrates – Dip Coating

The dip coating method used for the coating of the catalysts from the sol-gel colloidal solution. The filter paper substrates (commercial and cellulosic) were immersed into the solution with a speed of 20 mm/s and withdrawn with a speed of 2 mm/s while the solution is mixed by magnetic stirrer slowly. The coated samples then dried in an oven with a set value of 100°C, overnight. The coatings for immersed one time through the dip coating.

Some of the samples are not heat treated to see the drying effect on the catalyst efficiency. The number of immersions also changed during the experiment as a catalyst amount parameter to see the efficiency of the TiO_2 catalyst.

The stainless-steel wire mesh samples were coated similarly, after the drying 1h at 100°C in the oven in between the number of immersions, the coated samples were heat treated in a preheated tubular furnace (Protherm 1000W, PTF 12/50/250) under air atmosphere. The heat treatment, calcination, was conducted at 500°C for 30 minutes.

Figure 3.2 summarizes the schematic configuration of the coating system below.

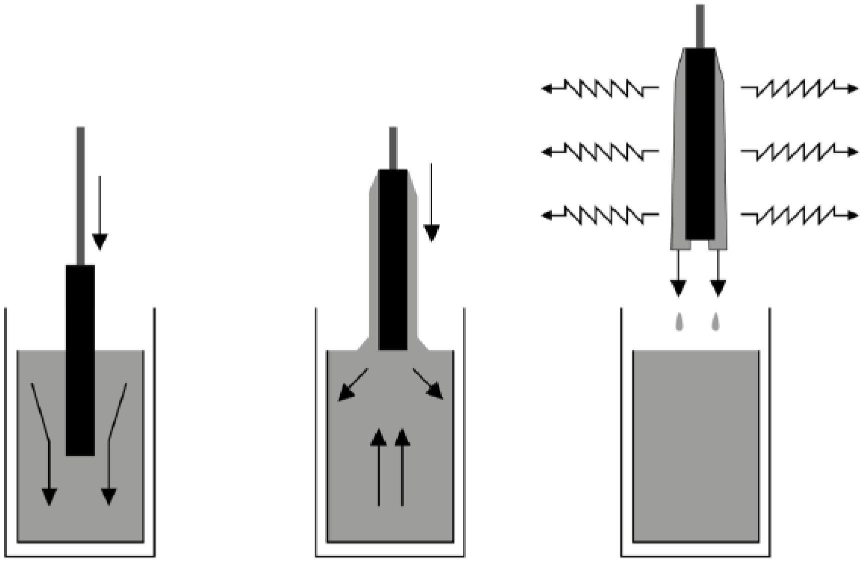

Figure 3.2 Dip Coating Method

3.2.1 Calibration of Dip Coating Equipment

Equipment used for dip coating is calibrated additionally to ensure that the dip and withdrawal rates are accurate. The equipment's maximum and minimum velocity indications are roughly 20 and 2, respectively. With the known dipping distance of

7 cm, the time is evaluated and utilized to specify the actual dip and withdrawal rates by altering the equipment configuration.

The graph of the velocity and dip/withdrawal rate was created in accordance with this data. The findings of the equipment's set parameters and the corresponding real dipping and withdrawal rates are presented in Table 3.1 and Figure 3.3, respectively.

Table 3.1 The Dip Coating Calibration Data

Set Value	Time Spent (Konometer)	Time Spent (s)	Real Withdrawal Velocity (mm/s)
2	14'25"78	866	0,087
3	6'36"36	397	0,189
4	4'42"62	283	0,265
5	3'26"65	207	0,362
6	2'45"44	166	0,452
7	2'18"96	139	0,540
8	1'56"56	117	0,641
9	1'46"35	106	0,707
10	1'31"89	92	0,815
11	1'23"98	84	0,893
12	1'15"01	75	1,000
13	1'9"00	69	1,087
14	1'3"63	64	1,172
15	1'1"28	61	1,229
16	55"52	56	1,339
17	52"76	53	1,415
18	48"82	49	1,531
19	46"80	47	1,596
20	44"91	45	1,704

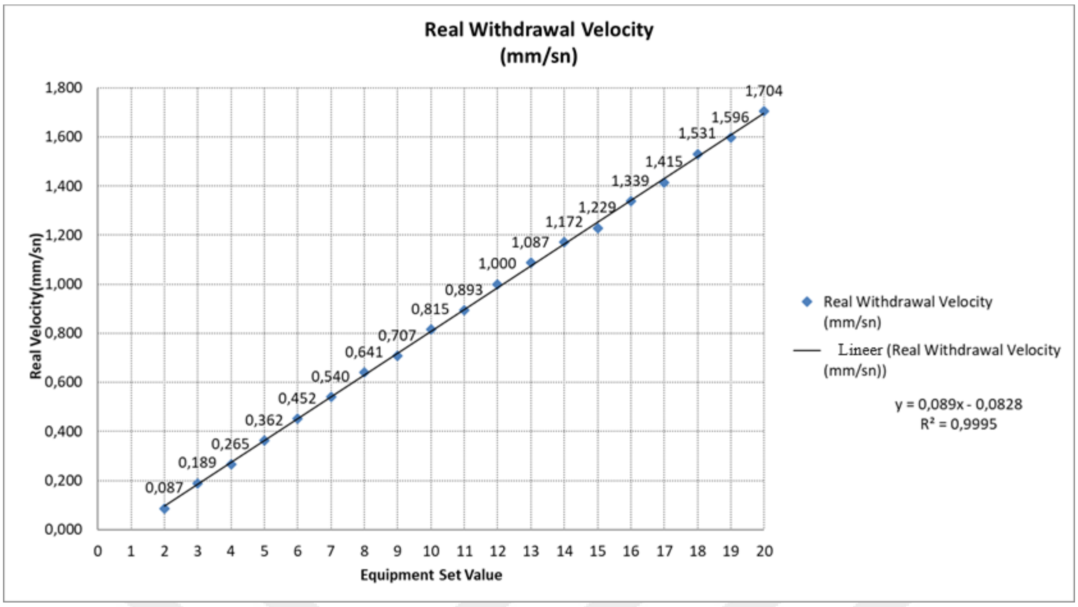

Figure 3.3 Real Time Withdrawal Rate of the Dip Coating Equipment

With the assistance of Figure 3.3 the following has determined.

- The withdrawal rate 2 represents a removal rate of 0.087 mm/s.
- The dipping rate 20 gives a depth of 1,704 mm/s.

3.3 Substrates and Catalyst Characterizations

The substrate samples and TiO_2/ SiO_2 coated samples were characterized to analyze the crystalline structure, surface area, chemical structure, surface morphology and catalyst composition by using TGA/DTA, XRD, BET techniques.

3.3.1 Thermal Analysis

Heat resistance of the substrate samples are critical to optimize and decide the curing and the calcination temperature during the catalyst synthesis. In order to comprehend the heat resistance of the commercial filter paper and cellulosic support materials, thermal gravimetric analysis (TGA/ DTA) conducted for the cellulose extraction thimble substrates. The goal of this analysis is to determine drying and calcining conditions for sol-gel synthesized TiO_2-SiO_2 catalyst layer. Shimadzu DTG-60H Differential Thermal Gravimetric Analyzer in METU CHE Department was used for analysis. By applying10°C/min heating rate under N_2 flow up to 500°C.

3.3.2 Brunauer Emmett Teller (BET) Analysis

The Brunauer Emmett Teller (BET) method was applied to determine the specific surface area by nitrogen adsorption measurements. The data were documented using the Micromeritics Gemini V system. Before the experiment, the samples underwent degassing at a temperature of 110°C for a duration of 12 hours in the presence of the ambient environment, in order to remove all gas molecules from the surface. The procedure of removing gases was conducted in a furnace. Nitrogen was utilized as an inert gas, and the surface area of the samples was determined by measuring nitrogen adsorption isotherms at a temperature of 77 K in METU Laboratories.

3.3.3 X-Ray Diffraction (XRD) Analysis

The crystal structure and crystallite size of TiO_2-SiO_2 layer were analyzed by using X-Ray Diffraction (XRD) analysis. The device measures the brag angle theta (θ) between the plane and the X-ray as it is sent to the catalyst's crystallographic center and scattered by atoms. The relative intensities of the peaks on the graph, which are detected when the intensity for each reflection is plotted against the scattering angle (2θ), are the crucial data from which the structure is ascertained. Using a CuKα source, the XRD (Rigaku Ultima IV Diffractometer in METU Central Lab) examination of the catalyst was performed between 10 and 90 degrees at a grazing angle of 0,5 degrees. The wavelength of the Cu source is 0,15405 nm. The Rigaku PDXL XRD Analyses Software was used for identification and comparison with reference peaks of various substances. to capture the standard peaks of the various substances.

3.4 Photocatalytic Activity Tests

Photocatalytic activity tests of synthesized catalyst samples were conducted by using a re-circulated batch reactor system. The time course of gas phase composition within the reactor was measured and monitored in-situ by recirculating reaction gas mixture through FT-IR spectrometer gas transmission cell.

3.4.1 Experimental Set-Up

The set-up consists of a glass cylinder (by Alltech) which is connected six gate port valve, gas pump for the recirculation, quartz reactor with UV lamps and in-situ FT-IR gas sampling cell and a computer for collecting the data (Figure 3.4). The system built by stainless steel 1/8 inches tubing.

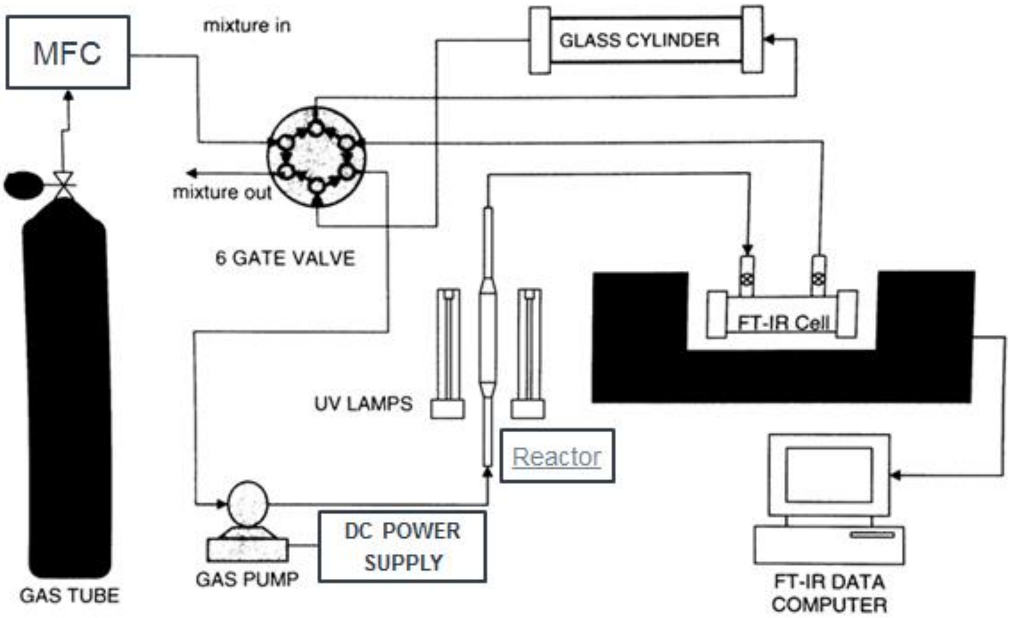

Figure 3.4 Experimental Set-Up

The six port (gate) valve of the system was used to introduce predetermined volume of carbon monoxide in glass cylinder into air atmosphere in photoreactor-FTIR-

Pump loop. Before the experiments, the catalyst sample was placed in photoreactor, and reactor is connected into system. Carbon monoxide-helium gas mixture was passed through six port valve, gas cylinder and send into hood (filling operation). When the system is ready, six port valve was switched and the carbon monoxide in the glass cylinder was mixed with the air within the system (recirculation mode). The formation of homogeneous mixture of CO-air was controlled by monitoring transmittance between 2025-2225 cm^{-1} through FTIR. When the homogeneous mixture is obtained, the photocatalytic reaction was started by switching on the UV lamps around photoreactor. The initial concentration of carbon monoxide in reaction mixture was adjusted by changing the volume of glass cylinder. For this purpose, Teflon cylinders with pre-calibrated volumes were used which are inserted in the glass cylinder to reduce the filled carbon monoxide-helium gas mixture volume. The gas volume injected into glass cylinder was calculated from the difference between the empty glass cylinder and total volume of Teflon cylinders inserted in experiment. The details of filling and recirculation modes are given below.

- Filling
- Recirculation

In the filling position, the glass cylinder was swept filled with a known volume of CO/He gas mixture (%5 CO in He by volume) with a flow rate of 50mL/ min which was controlled with a mass flow controller. The gas mixture within the glass cylinder is maintained at ambient pressure by exhaust line which is opened into hood.

In the recirculation position, the gas mixture, filled to the glass cylinder with a known volume, was sent into the closed system of reactor - FTIR pump loop. This gas recirculated till the concentration of carbon monoxide in reaction mixture reaches steady state (Figure 3.5). The recirculation of gas mixture is achieved by turning on the diaphragm type gas pump which is driven by 12 VDC.

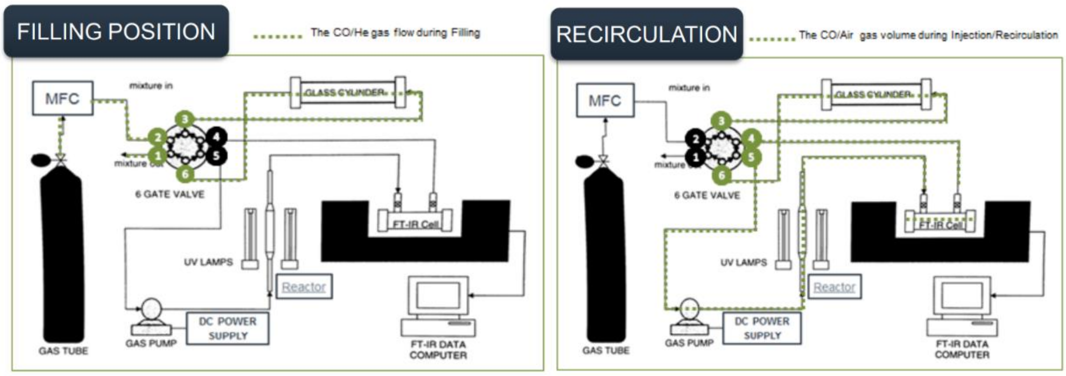

Figure 3.5 Filling and Recirculation Positions of the Six-Port Valve

3.4.2 Reactor Design

The reactor is built by quartz tubing to allow UV irradiation at 254 nm and was equipped with catalyst holder, inlet, and outlet for gas mixture. In order to achieve isothermal operation around room temperature, the reactor system is equipped with two external cooling fans to remove heat generated in UV lamps. Two 36-Watt 254 nm lamps were used for irradiation.

In order to overcome the problem of leakage through quartz-metal connections chemical sealants were used. The drawing of photocatalytic reactor is shown in Figure 3.6.

The reactor system has been designed to prevent excess heat within the reactor system, which causes an increase in gas volume and produces inaccurate conversion statistics. The number of fans was two, and the number of UV lamps was also two.

In order to overcome the problem of leakage, the reactor, which should be designed such that the filter paper can be replaced at any moment for synthesis parameter analysis, was fixed without mechanical means; instead, chemical sealants were utilized. The reactor design represented in the Figure 3.6.

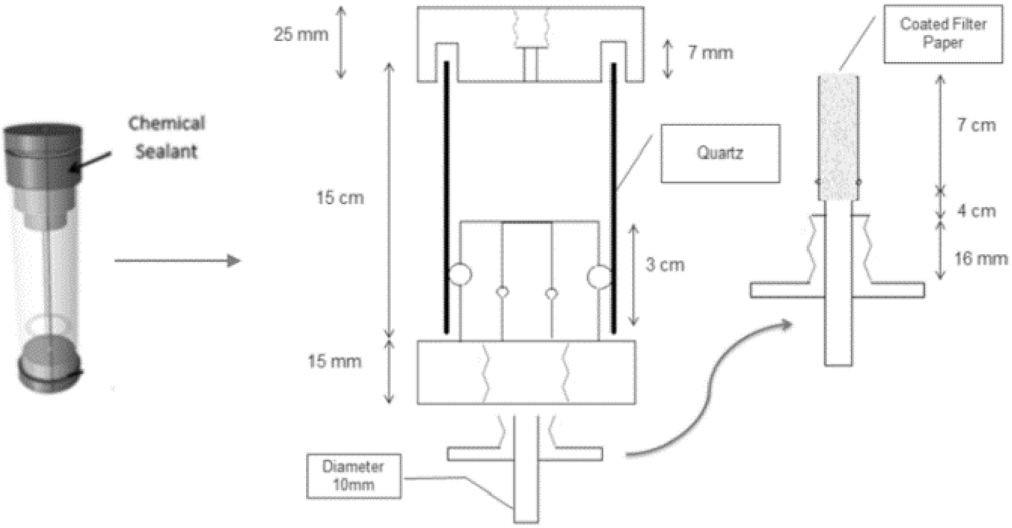

Figure 3.6 Photocatalytic Reactor Unit

3.4.3 Calibration of the Experimental Setup for The Photocatalytic Activity Tests

The system has been calibrated in order to conduct a quantitative analysis of the CO and CO_2 concentrations in the system during the reaction. For this reason, each CO and CO_2 absorbance measurement should be given as concentration values.

3.4.3.1 Filling Mode

In this mode, the glass cylinder depicted in Figure 3.4 of the Experimental Setup was filled with a predetermined concentration of He/ CO combination. With the aid of an intake valve, the 6 port valve permits the admission of the 5% CO in He gas combination. The tube's gas mixes are sent to port 2 and then passed through port 3, which is the glass cylinder's inlet. The output of the glass cylinder is then exposed to the room via port 6. In the filling position, the pump was closed and in the circulated system, room air was existing.

The schematic representation of the He/CO gas mixture flow during the filling mode is given below as Figure 3.7.

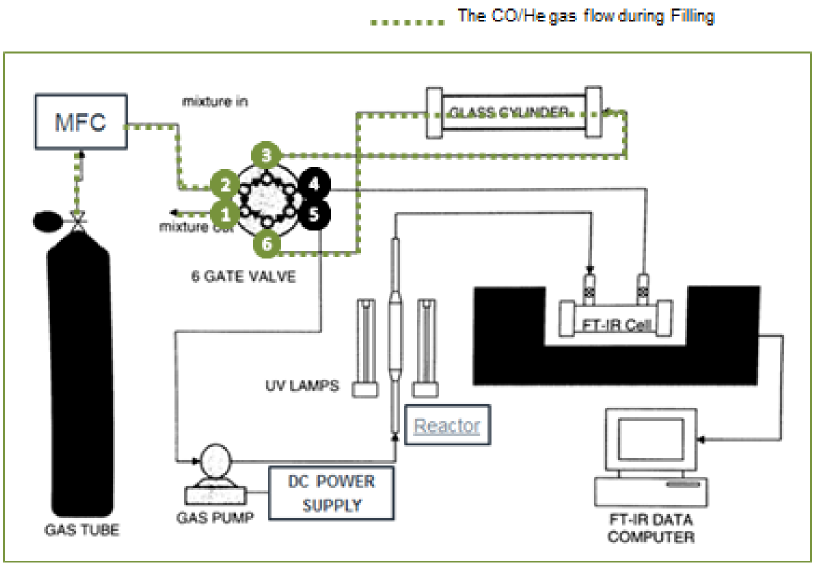

Figure 3.7 Filling Mode

3.4.3.2 Injection/Recirculation Mode

In the injection mode, which was initiated by switching the button, the gas in the glass cylinder began to enter the reactor system and FTIR. First, the gas from the tube is turned off by closing the valve, and then the pump is turned on. Now, the gas in the glass cylinder flows through port 6 to the pump entrance, which is port 5.

This gas is pumped and then transported to the reactor. The reactor's outflow is connected to the FTIR, enabling analysis. The exit of the FTIR re-enters port 3 (which is the input of the glass cylinder via port 6). The known volume of gas in the glass cylinder is then mixed with room air and cycled throughout the entire analysis.

The schematic representation of the Air/CO gas mixture flow during the filling mode is given below as Figure 3.8.

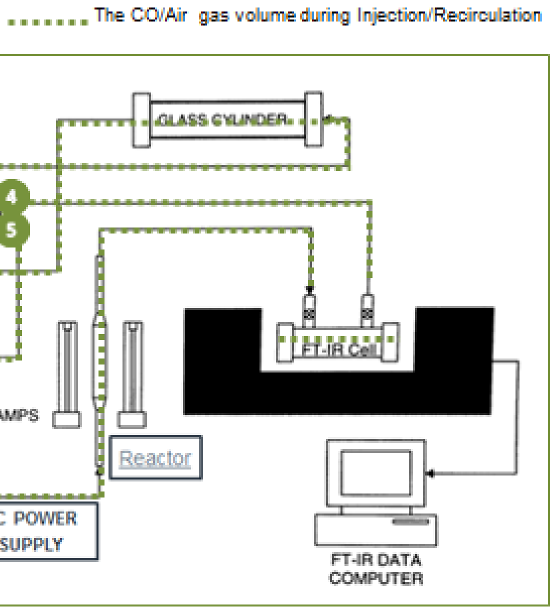

Figure 3.8 Injection/ Recirculation Mode

3.4.3.3 FTIR Calibration for CO Concentration Measurements

The CO concentration used in the experiments and FTIR measurements were calibrated by using known volumes of glass cylinder and cylindrical Teflon inserts. For this purpose, the glass cylinder is set to a known volume, and it is filled with 5% CO in He at ambient pressure and temperature in the filling position of six gate valves while room air is being fed by the gas pump through empty reactor - FTIR cell loop. The volume of empty reactor, connecting tubes and FTIR cell loop was determined by using physical dimensions. Bruker Equinox-55 FT-IR spectrophotometer was used for measurements. Before the CO is introduced into air in reactor, background scan spectrum was collected in order to determine the reference line. Then, CO/ He mixture in glass cylinder with known volume was introduced into the system by switching six port valves into recirculation mode and circulated pump was switched on and CO-air mixture recirculation was started. FT-IR spectrum of the gas mixture is monitored around 2025-2225 cm^{-1} wave number and system is recirculated in dark till steady state peak height of CO is achieved. This procedure was repeated on a variety of gas cylinder volumes to obtain different CO concentrations within the reaction system and corresponding FTIR transmission/ absorption peak heights were determined. Absorbance peaks of each concentration against a certain wavenumber range was recorded by the OPUS software.

The obtained 3rd order polynomial calibration equation was used to determine the time course CO concentration measurements during photocatalytic activity measurements.

3.4.3.3.1 Calculation of CO/He Gas Mixture Volume for the Test System

Gas tube: 5% CO in He = 50000 ppm CO in He

As the system switches to recirculation/injection mode, the CO concentration within the glass cylinder decreases. The known volume and concentration of the He/CO mixture gas were mixed with the recirculation system's room air.

The following equation can be used to determine the new concentration of CO in air.

$$V_A \times N_A = (V_A + V_B) \times N_B$$

Where;

- N_A is the concentration of the CO in CO/He mixture which is 50000ppm.
- V_A is the volume of the glass cylinder (cm^3) which is 128$cm^{3.}$
- V_A+V_B is the volume of the total recirculation system (cm^3)
- N_B is the concentration of the CO in air (ppm)

The system volume (V_B) calculated with the data in Table 3.2.

Table 3.2 Data for the System Volume Calculation

Item	Detail	Volume (cm^3)	Total System Volume (cm^3)
Piping	Port 3 - Glass Cylinder	22,15	613,25 (V_B)

Table 3.2 (continued) Data for the System Volume Calculation

	Glass Cylinder – 6		
	Port 6 - Port 5		
	Port 5 – Pump		
	Pump – Reactor		
	Reactor - $FTIR_{in}$		
	$FTIR_{out}$ - Port 4		
	Port 4 - Port 3		
Reactor	Inner Volume	167	
FTIR Cell	Inner Volume	424,1	

Since the V_A, N_A, and V_A+V_B values are known, it is straightforward to calculate different N_B (CO concentration in Air) by varying the V_A value. Teflon samples with a volume of 14,14cm^3 contribute to the dilution of the system volume. The glass cylinder filled with varying amounts of Teflon samples altered the V_A value and allowed the N_B to be calculated for varying volumes of V_A. This procedure changed the CO concentration in He to the CO concentration in air.

Sample calculation for without any Teflon sampling.

The N_A = 50000ppm

V_A+V_B= 741,25cm^3

V_A= 128cm^3

Thus, N_B (CO concentration in air) is.

$128\times50000= (741,25) \times N_B$

N_B=8634 ppm

Other arbitrary volumes of CO/He mixture and their corresponding CO/Air compositions are included in Table 3.3.

Table 3.3 CO/He Volumes and The Calculated CO Concentrations in Air

#of Teflon Samples	V_A (cm^3)	N_A (ppm)	V_A+V_B (cm^3)	N_B (ppm)
0	128	50000	741,25	8634
1	113,86	50000	727,11	7830
2	99,72	50000	712,97	6993
3	85,58	50000	698,83	6123
4	71,44	50000	684,69	5217
5	57,3	50000	670,55	4273
6	43,16	50000	656,41	3288
7	29,02	50000	642,27	2259
8	14,88	50000	628,13	1184
Full	0	50000	613,25	0

3.4.3.3.2 Calculation of the Absorbance-Concentration Equation for CO

For each concentration of CO in air, data were taken by FTIR to plot the absorbance peaks of each concentration. Those calibration curves are as seen in Figure 4.8.

In order to get the calibration third order equation, CO concentration was plotted against absorbance at the average wavenumber point of 2174,35 - 2170,49 cm^{-1}.

The data found for the calibration are given in Table 3.4.

On the average wavelength, CO concentration vs absorbance is plotted as Figure 3.9.

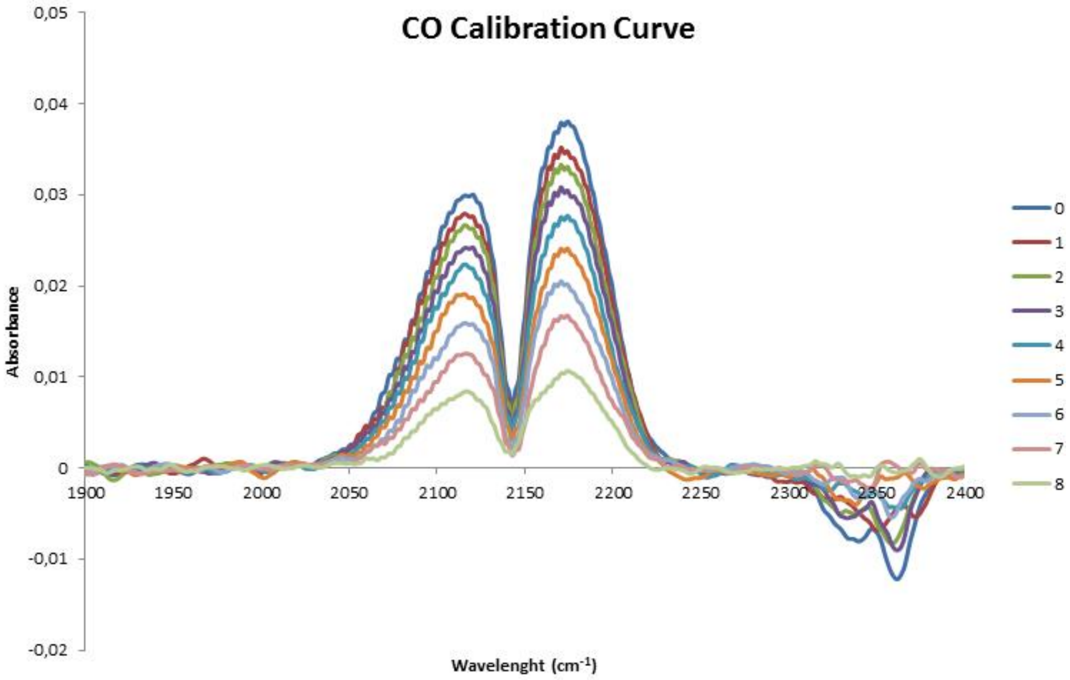

Figure 3.9 Calibration curves for CO obtained by FTIR during the dark re-circulation of several concentrations of CO in air.

Table 3.4 CO/He volumes and their absorbance values for CO concentrations in air

V_A (cm^3)	C_{CO} (ppm)	Absorbance (Av. Max OPUS Data)
128	8634	0,037845791
113,86	7830	0,034821774
99,72	6993	0,033015411
85,58	6123	0,030477808
71,44	5217	0,027478637
57,3	4273	0,023969476
43,16	3288	0,020229493
29,02	2259	0,01663362
14,88	1184	0,010499149
Empty	0	0

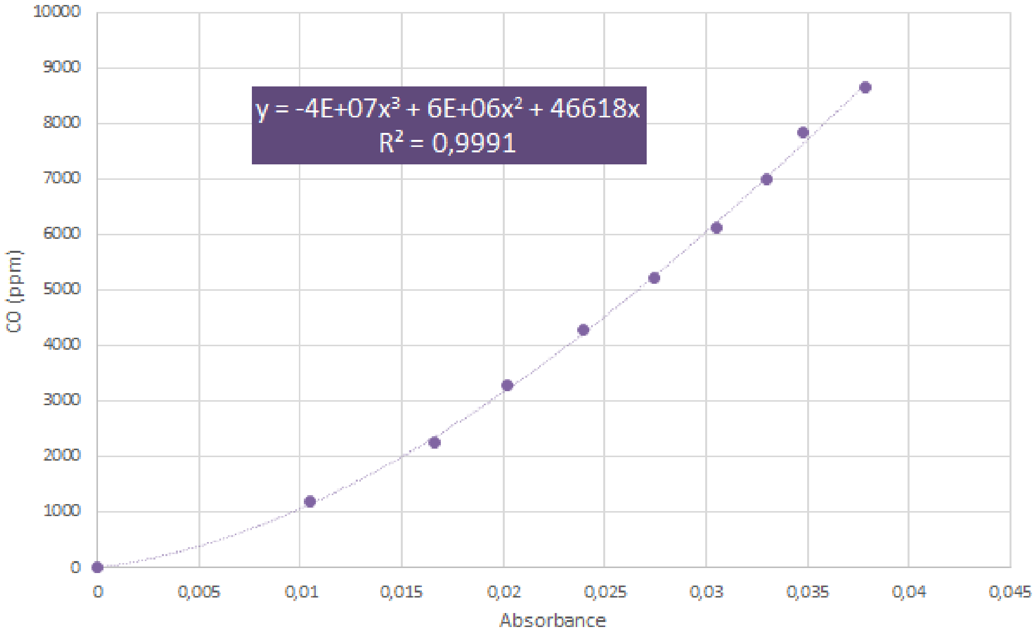

Figure 3.10 CO Concentration values in air wrt Abs on Wavelength

The third order equation of the curve passing through the data above is:

$$y = -4E+07x^3 + 6E+06x^2 + 46618x$$
$$R^2 = 0,9991$$

Where y (= C_{CO}) is CO concentration in air in ppm and x (= A) is absorbance. The concentration values for each CO peak could be calculated from the absorbance data using this equation. The optimal data for the CO peak was determined to be the maximum average of the absorbance values between 2174,35cm^{-1} and 2170,49cm^{-1}.

These wavelengths will now be utilized for quantitative CO analysis.

3.4.3.4 FTIR Calibration for CO_2 Concentration Measurements

The FTIR system was also calibrated for CO_2 absorbance peaks to determine the concentration and formation rate of reaction product. For this purpose, similar calibration work was performed by using 99,9% CO_2 gas. The system was fixed to a known volume by using standardized tubing attached to the 6-port valve.

The CO_2 concentration was measured between 2250-2400 cm^{-1} wavenumber range.

A 3rd order equation for the CO_2 concentration was developed using the CO_2 calibration data. The formula used to determine the CO_2 concentration for each sample output during the tests of photocatalytic activity.

3.4.3.4.1 Calculation of CO_2 Volume for the Test System

Gas tube: 99,9% CO_2 by Air Products

As the system switches to recirculation/ injection mode, the CO_2 concentration in the 6-port gate decreases.

The known volume and concentration of the CO_2 gas mixed with the room air in the recirculation system, as determined by standardized sampling. The following equation can be used to determine the new CO_2 air concentration.

$$V_A \times N_A = (V_A+V_B) \times N_B$$

Where;

- N_A is the concentration of the CO_2 in which is 1000000ppm.
- V_A is the volume of the standardized samplings (cm^3)
- V_A+V_B is the volume of the total recirculation system (cm^3)
- N_B is the concentration of the CO_2 in air (ppm)

The total system volume (V_B) calculated as follows in Table 3.5.

Table 3.5 Calculation Data of The System

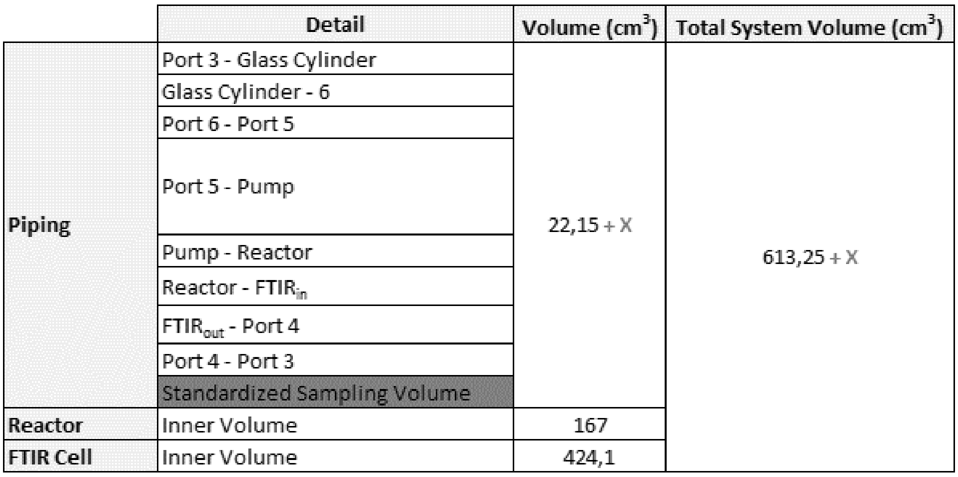

	Detail	Volume (cm^3)	Total System Volume (cm^3)
Piping	Port 3 - Glass Cylinder	22,15 + X	613,25 + X
	Glass Cylinder - 6		
	Port 6 - Port 5		
	Port 5 - Pump		
	Pump - Reactor		
	Reactor - $FTIR_{in}$		
	$FTIR_{out}$ - Port 4		
	Port 4 - Port 3		
	Standardized Sampling Volume		
Reactor	Inner Volume	167	
FTIR Cell	Inner Volume	424,1	

Since V_A, N_A, VA+V_B, and standardized sampling values are known, varied N_B (CO_2 concentration in Air) can be easily determined by varying the standardized sampling volume. Changing the value of V_A enables the N_B computation for varying V_A volumes. This process converts the CO_2 concentration to the CO_2 concentration in air.

Sample calculation for standardized sampling of 5mL.

- N_A = 1000000ppm
- V_A+V_B= 623,25cm^3
- V_A= 5cm^3

Thus, N_B (CO concentration in air) is.

$$5 \times 1000000 = (623,25) \times N_B$$

$$N_B = 8022 \text{ ppm}$$

Other arbitrary volumes of CO_2 mixture and their corresponding CO_2/Air compositions are included in Table 3.6.

Table 3.6 CO/He Volumes and Their Calculated CO Concentrations in Air

		%100 CO_2 in Air						
V_A (cm^3)	N_A (ppm)	VFTIR	Vreactor	Vpipeline	V Additinal Pipeline (mL)	V_B (sistem cm^3)	V_A+V_B (cm^3)	N_B (ppm)
5	1000000	424,1	167	22,15	5	618,25	623,25	8022
3,4	1000000				3,4	616,65	620,05	5483
1	1000000				1	614,25	615,25	1625
0,5	1000000				0,5	613,75	614,25	814
0	1000000				0	613,25	613,25	0

3.4.3.4.2 Calculation of the Absorbance-Concentration Equation for CO_2

For each concentration of CO_2 in air, data were taken by FTIR to plot the absorbance peaks of each concentration. Those calibration curves are given in Figure 3.11.

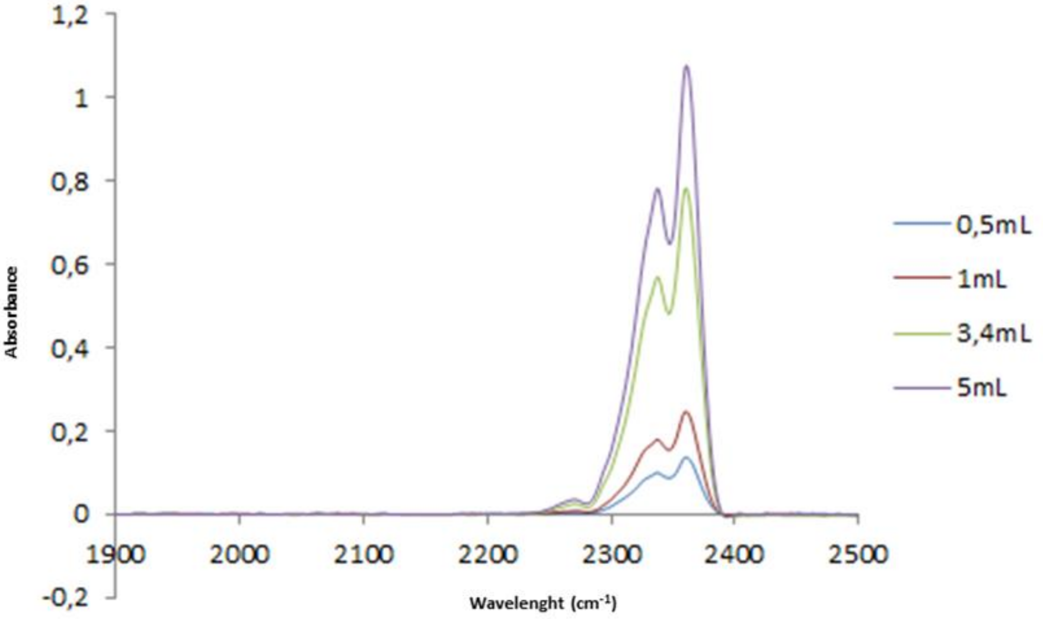

Figure 3.11 Calibration Curves for CO_2 Obtained by FTIR During the Dark Re-circulation of Several Concentrations of CO_2 in Air

CO_2 concentration was plotted against absorbance at the average wavenumber range of 2362,37 - 2358,51 cm^{-1} to obtain the calibration equation for the third order.

The results of the calibration are presented in Table 3.7.

Figure 3.12 depicts the relationship between CO concentration vs absorbance at the average wavelength.

Table 3.7 CO_2 Volumes and Their Calculated CO_2 Concentrations in Air

V_A (cm^3)	C_{CO2} (ppm)	Absorbance (Av. Max OPUS Data)
5	8022	1,064299808
3,4	5483	0,774258274
1	1625	0,243847849
0,5	814	0,135193507
0	0	0

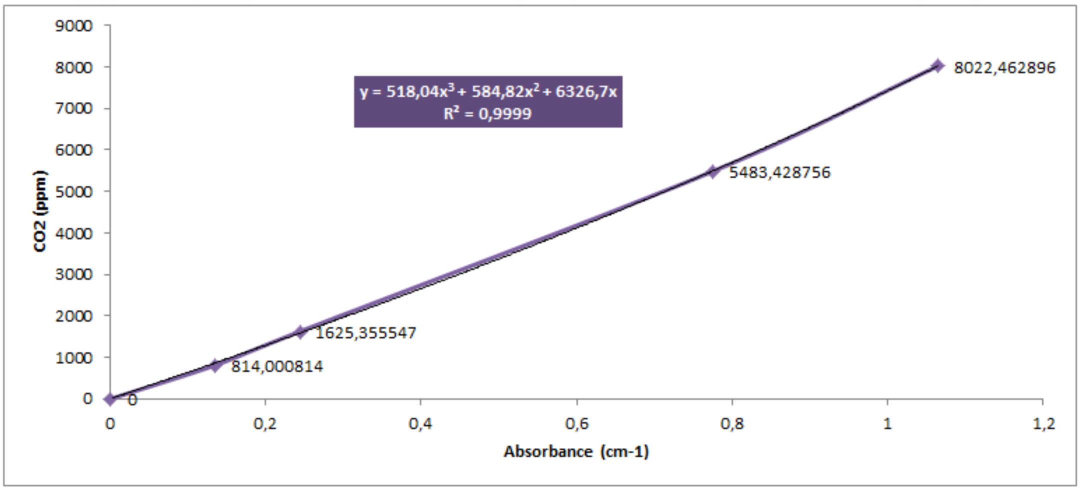

Figure 3.12 CO_2 Concentration Values in Air wrt Abs on Wavelength

The third order equation of the curve passing through the data is:

$$y = 518{,}04x^3 + 584{,}82x^2 + 6326{,}7x$$
$$R^2 = 0{,}9999$$

Where y (= C_{CO2}) is CO_2 concentration in air in ppm and x (= A) is absorbance. With that equation, the concentration values for each CO_2 peak could be evaluated from the absorbance data. The optimal data for the CO_2 peak was determined to be the maximum average of absorbance values between wavelengths 2362,37 and 2358,51 cm^{-1}. These wavelengths will now be used for quantitative CO_2 analysis.

CHAPTER 4

RESULTS AND DISCUSSION

In this study several catalysts containing TiO_2/ SiO_2 molar ratio of 0,5 were synthesised and coated over substrates cellulose filter paper, PP commercial filter paper and 304 stainless steel wire mesh as support alternatives.

4.1 Catalyst Preparation

Catalyst samples were prepared by using sol-gel method as introduced in the previous chapter. The catalysts are coated over different substrates by using dip coating method. The number of immersions was kept one for the experiments. Reference notation refers to an un-coated substrate.

Table for the codes, which described in experimental method, are shared below.

Table 4.1 Code of Samples

No	**Sample Code**	**Substrate**	**Cat. (g)**	**Oven (h)**	**Oven T^{o}C**
1	TiO_2/ SiO_2 Com_1	Commercial	0,060	48	100
2	TiO_2/ SiO_2 Com_2	Commercial	0,025	24	100
3	TiO_2/ SiO_2 Com_Ref	Commercial	N/A	N/A	N/A
4	TiO_2/ SiO_2 C_1	Cellulose	0,853	48	100
5	TiO_2/ SiO_2 C_2	Cellulose	1,472	24	100
6	TiO_2/ SiO_2 C_3	Cellulose	0,687	24	100
7	TiO_2/ SiO_2 C_4	Cellulose	0,863	24	100
8	TiO_2/ SiO_2 C_Ref	Cellulose	N/A	N/A	N/A

Table 4.1 (continued) Code of Samples

9	TiO_2/ SiO_2 S_1 wo Calc	Stainless Steel	0,433	24	100
10	TiO_2/ SiO_2 S_2 with Calc	Stainless Steel	0,433	0,5	500
11	TiO_2/ SiO_2 S_Ref	Stainless Steel	N/A	N/A	N/A

4.2 Characterization

4.2.1 Thermal Analysis for Substrates

4.2.1.1 TGA Analysis of Commercial PP Filter Paper

In order to determine the maximum temperature that can be applied for drying and calcination treatments, the thermal properties of support materials were characterized by using TGA-DTA Analysis under N_2 flow.

The test held on up to 900°C degrees with 10°C/min ramp rate. The result of the TGA analysis given as Figure 4.1.

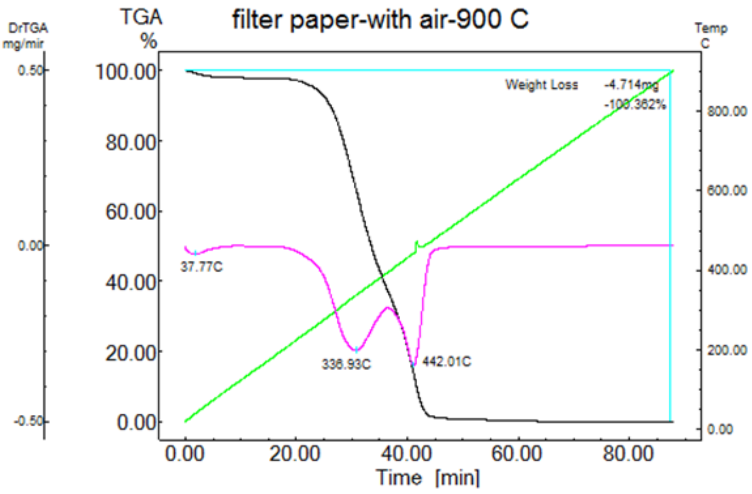

Figure 4.1 TGA-DTA of Commercial Filter Paper

As a result, it may be deduced that the filter paper decomposes under N_2 at about 250°C. Therefore, after the dip coating, calcination of the samples with filter paper is not applicable. Since no calcination for HC’s are possible for this temperature, the drying temperature choosen as 100°C for water evaporation.

4.2.1.2 TGA Analysis of Cellulose Filter Paper

In order to determine calcination and drying temperature of sol-gel prepared TiO_2/SiO_2 over cellulose filter paper TGA- DTA Analysis of support material was conducted under N_2 flow. The test held on up to 500°C degrees with 10°C/ min intervals. The result of the TGA analysis given as Figure 4.2.

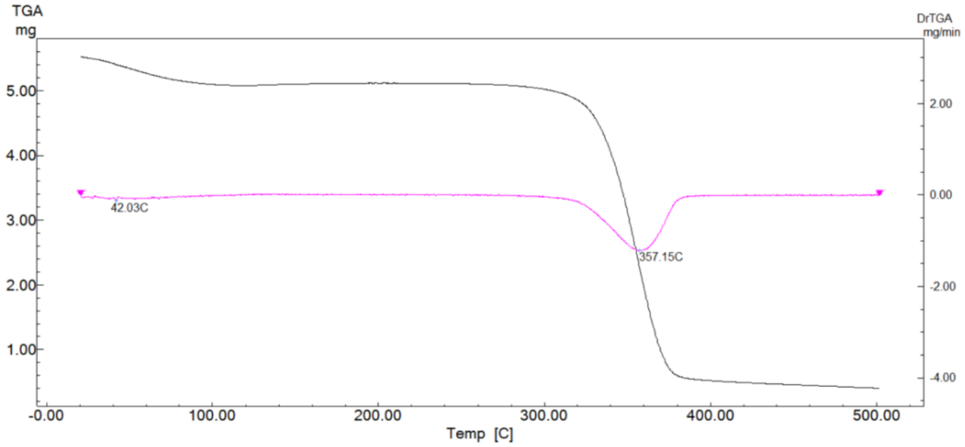

Figure 4.2 TGA-DTA of Cellulose Filter Paper

At the beginning of the scan, there is a slight weight drop that can be attributed to water evaporation. The significant weight loss observed at 357℃, indicates the decomposition of the cellulose.

Consequently, it may be determined that the filter paper decomposes at roughly around 250°C. Therefore, calcination of the samples after dip coating is not applicable for the filter paper sample. The drying temperature choosen as 100 degrees Celsius for water evaporation.

4.2.1.3 TGA Analysis of 304 Stainless-Steel Wire Mesh Support

Since the stainless steel mesh wire substrate is a metal and it is known that SS304 material is stable within the temperature range of 25-830°C for continuous service which is below the calcination temperature range of sol-gel synthesised TiO_2/SiO_2 samples. Therefore no TGA/DTA characterization was made for SS304 mesh wire samples.

4.2.2 Brunauer – Emmett – Teller (BET) Analysis

The textural properties of the samples of sol gel synthesized TiO_2/ SiO_2 coated over selected support materials were analyzed by nitrogen absorption -Brunauer-Emmett-Teller (BET) technique.

4.2.2.1 BET Analysis for TiO_2 – SiO_2 Coated PP Commercial Filter Paper

The BET results are summarized in Table 4.2. Reference represents the uncoated bare support material surface area.

Table 4.2 Summary for BET Surface Area for Commercial Sample

Sample Number	Sample Code	BET Surface Area (m^2/gr)
1	TiO_2/SiO_2 Com_1	4,2
2	TiO_2/SiO_2 Com_2	2,2
3	TiO_2/SiO_2 Com_Ref	2,1

As a result the commercial filter paper the catalyst is not reached inside the pores. The commercial filter paper is hydrophobic and can not be used for coating purposes. The alternative cellulose filter paper type will be used as a support material for catalys coating.

4.2.2.2 BET Analysis for TiO_2 – SiO_2 Coated Cellulosic Filter Paper

The BET results are summarized in Table 4.3. Reference represents the uncoated bare support material surface area.

Table 4.3 Summary for BET Surface Area for Cellulosic Sample

Sample Number	Sample Code	Bare Weight (g)	Coated Weight (g)	Catalyst Loading (g)	BET Surface Area (m^2/gr)
4	TiO_2/ SiO_2 C_1	3,6980	4,5513	0,8533	54,1
5	TiO_2/ SiO_2 C_2	3,5545	5,0261	1,4716	52,86
8	TiO_2/ SiO_2 C_Ref	3,2152	-	-	0,3923

As a result, it can be concluded that TiO_2/ SiO_2 C_1 and TiO_2/SiO_2 C_2 shows no significant difference. Increasing the drying time has no effect on the catalyst surface area. They are both coated and increased the surface area.

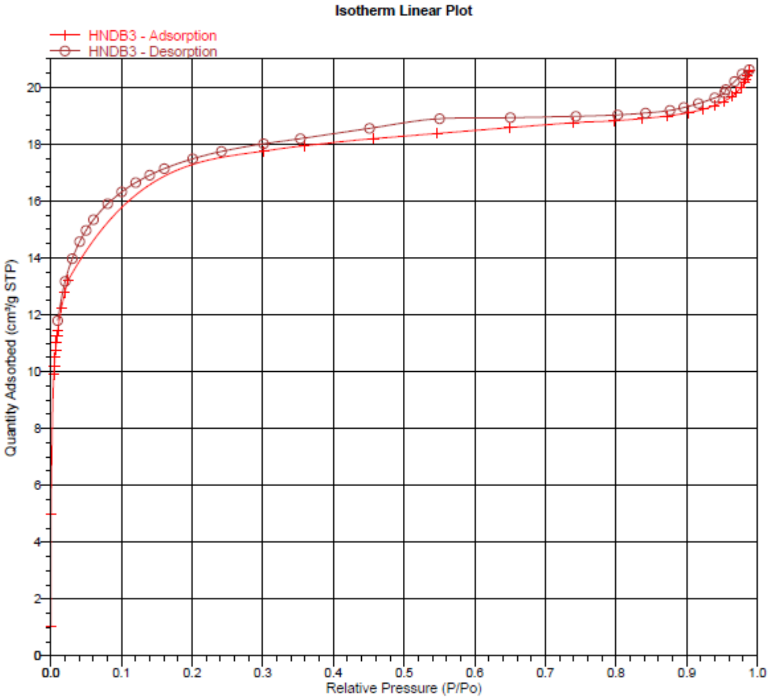

Figure 4.3 Absorption/ Desorption Curve of Sample 1

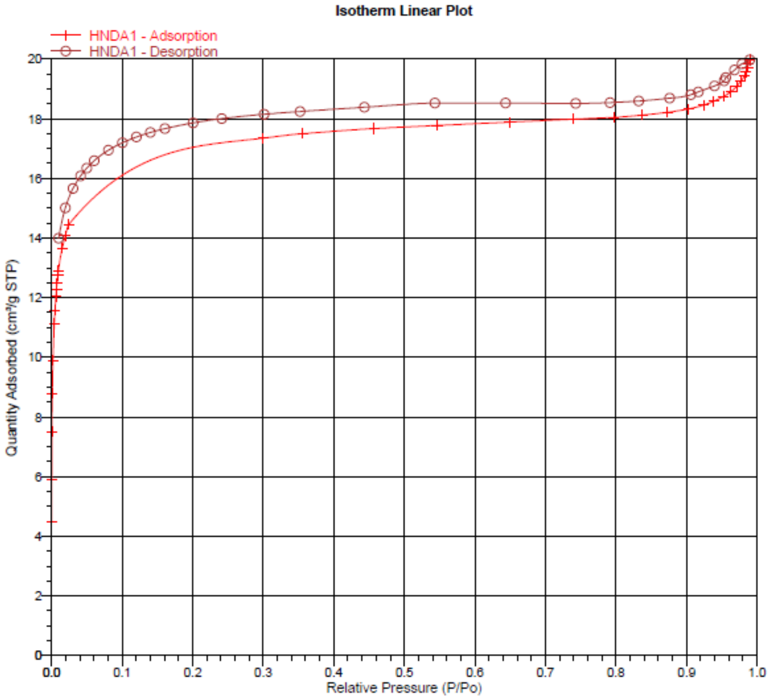

Figure 4.4 Absorption/ Desorption Curve of Sample 2

4.2.3 X-Ray Diffraction Analysis

X-ray diffraction analyses of the coated filter samples were performed to investigate the crystal phase of TiO_2 and crystallite size. Previous XRD analyses performed by Bilal et.al, showed that calcined unsupported TiO_2/ SiO_2 samples prepared by using the same method results with amorphous silica and TiO_2 in anatase phase (Bayram, 2009). The anatase form of the TiO_2 has a higher photocatalytic activity than other forms, rutile and brookite for most of the photocatalytic reactions. Phase transition from anatase to rutile above 500°C heat temperature has been reported in literature extensively. The samples treated below are not heat treated. Table 4.4 below [JADE software database] indicates the seven distinctive peaks of possible anatase and rutile TiO_2 phases with 2-Theta values and crystal surfaces.

Table 4.4 2-Theta Values of TiO_2 with respect to Crystal Structure

Crystal Structure	**#**	**I (fix)**	**I (var)**	**h k l**	**2-Theta**
Anatase TiO_2	1	100	100	1 0 1	25.3
	2	10	14	1 0 3	36.9
	3	20	29	0 0 4	37.8
	4	10	15	1 1 2	38.6
	5	35	65	2 0 0	48.1
	6	20	41	1 0 5	53.9
	7	20	42	2 1 1	55.1
Rutile TiO_2	1	100	86	1 1 0	27.5
	2	50	56	1 0 1	36.1
	3	8	9	2 0 0	39.2
	4	25	32	1 1 1	41.2
	5	10	13	2 1 0	44.1
	6	60	100	2 1 1	54.3
	7	20	34	2 2 0	56.6

The XRD patterns of TiO_2-SiO_2 over filter paper is shown in Figure 4.5. The XRD patterns of the samples reveals that the TiO_2 is in anatase phase. A sharp main peak at 2θ 25° is observed which is attributed to the anatase phase ICDD PDF Card No: 01-070-6826 (Kirbas, 2014).

Samples showed a broad peak around 5-10 2-theta interval is assigned into amorphous structure of SiO_2.

It can be concluded the the titania is shown as anatase and the amorphous silicate is shown at the beginning.

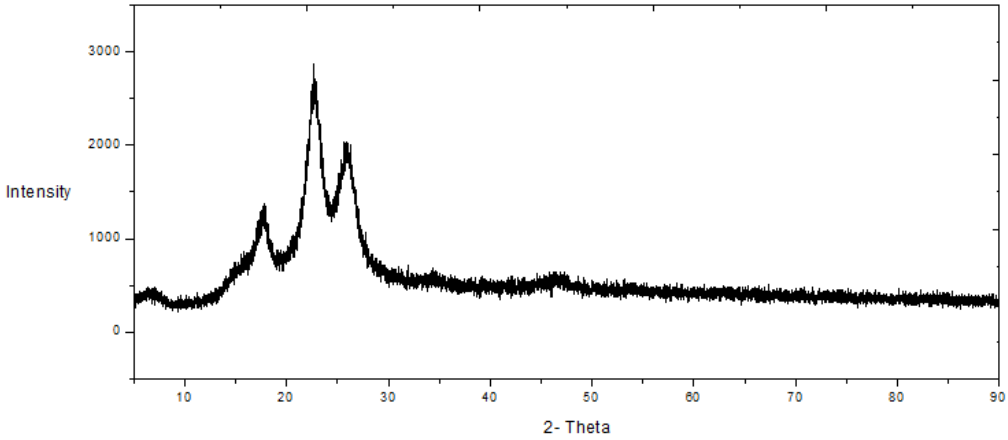

Figure 4.5 XRD Patterns of TiO_2-SiO_2 films under N_2 Atmosphere

4.3 Photocatalytic Activity Tests

4.3.1 Control Experiments

4.3.1.1 Leakage Test

Since the system is designed to recirculate the gas mixture in a closed loop, any leak can result in a misleading reaction. Thus, the leakage test was conducted to verify the experimental setup. The leak tests were conducted by injection the proper amount of CO gas into the reactor system and initiating the gas recirculation by switching on the diaphragm pump. In leak tests, the reactor was kept empty, in dark and no catalyst was used. CO level within the system was checked periodically (every 10 minutes) by measuring the absorption peak intensity of CO. Figure 4.6 depicts the CO peaks during the leakage test.

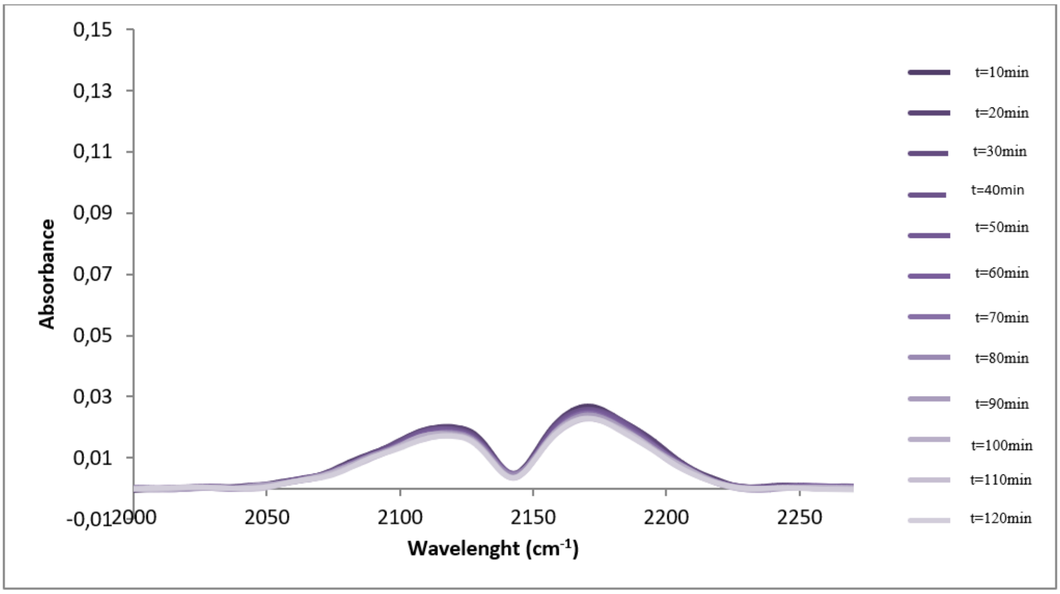

Figure 4.6 Leakage Test CO Peaks

As a result, no significant difference was noticed for the recirculating gas in the empty reactor. The CO concentration after 2 hours in the dark does not differ significantly from its concentration at t=10 minutes. Hence, it may be inferred that the new reactor system's seal is adequate. As indicated in the graph, there is no substantial variation in CO concentration (2025-2225 cm^{-1}), confirming that CO and air are mixed uniformly. The leakage test held in the beginning of each experiment to ensure the seal of the set-up.

4.3.1.2 Control Experiments Without the Quartz Reactor and Without the Catalyst under UV Irradiation

The reactor was constructed by using adhesives, heat-resistant tapes, quartz, and metal structure. Therefore, the stability of these materials under UV irradiation is critical to differentiate CO_2 formation between the decomposition of materials used in reactor assembly and CO oxidation. Therefore, another control experiment conducted to check the stability of materials used in reactor assembly under UV irradiation. This was accomplished by removing the reactor from the system and connecting the pipes with a connector (stainless steel 1/8-inch tubing) as indicated in Figure 4.7.

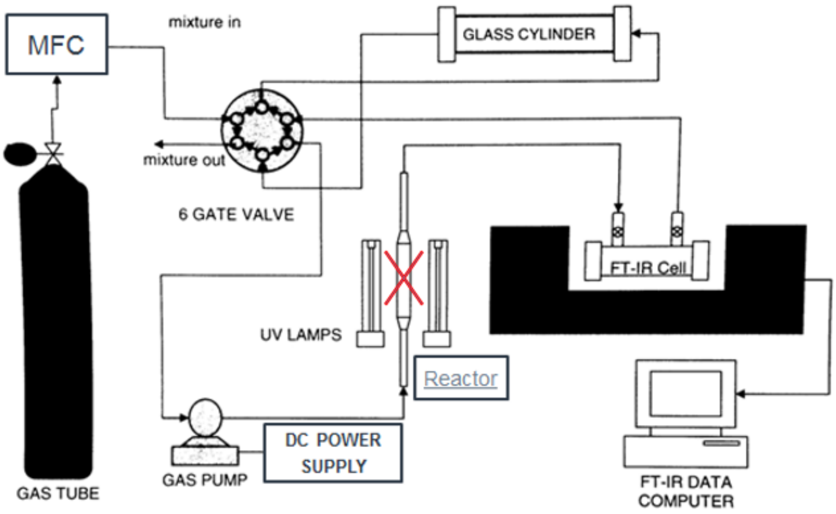

Figure 4.7 Experimental Setup for The Without Reactor Analysis

Prior to the test, the system was filled with fresh air. The proper amount of CO gas was introduced into the system, and gas recirculation was initiated by turning on the diaphragm pump.

During the recirculation of CO gas, FT-IR, and OPUS® software monitored the IR bands for CO and CO_2 against a wavenumber range of 1900-2500 cm^{-1}.

In order to see the appropriate mixing of CO and air in the reaction system, the mixing period was conducted, and the stability of the FT-IR spectrometer was ensured by executing the initial stage of experiments in the dark. The original dark period data was fixed at 9,5 hours. The second part of the experiments was initiated by turning on the light source in the irradiation chamber once the FT-IR spectrum had assessed the steady conditions. The light remained on for 10 hours, beginning at t=571 minutes.

In summary.

- Dark: 9,5h
- Light: 16,5h

Figure 4.8 depicts the time-dependent FT-IR spectra of the gas phase during the catalyst experiment.

As seen in the spectra, there was no variation in the CO peak intensities during the dark period (2025-2225 cm^{-1}). After illumination the adsorbed CO remained unchanged, precision of CO level change is around 500-900pmm, the average value remained in the precision limit. At the end, minimal decreases were obtained. In contrast, the CO_2 level increased to 740 ppm.

The change in CO absorbance with respect to wavelength was converted to CO and CO_2 Concentration vs. Absorbance data using the 3rd order calibration equation calculated in the previous section, with the correction for the entire system volume. For this experiment, the concentration data at room temperature for the catalyst is computed.

The data was given in Table A.1 in appendices.

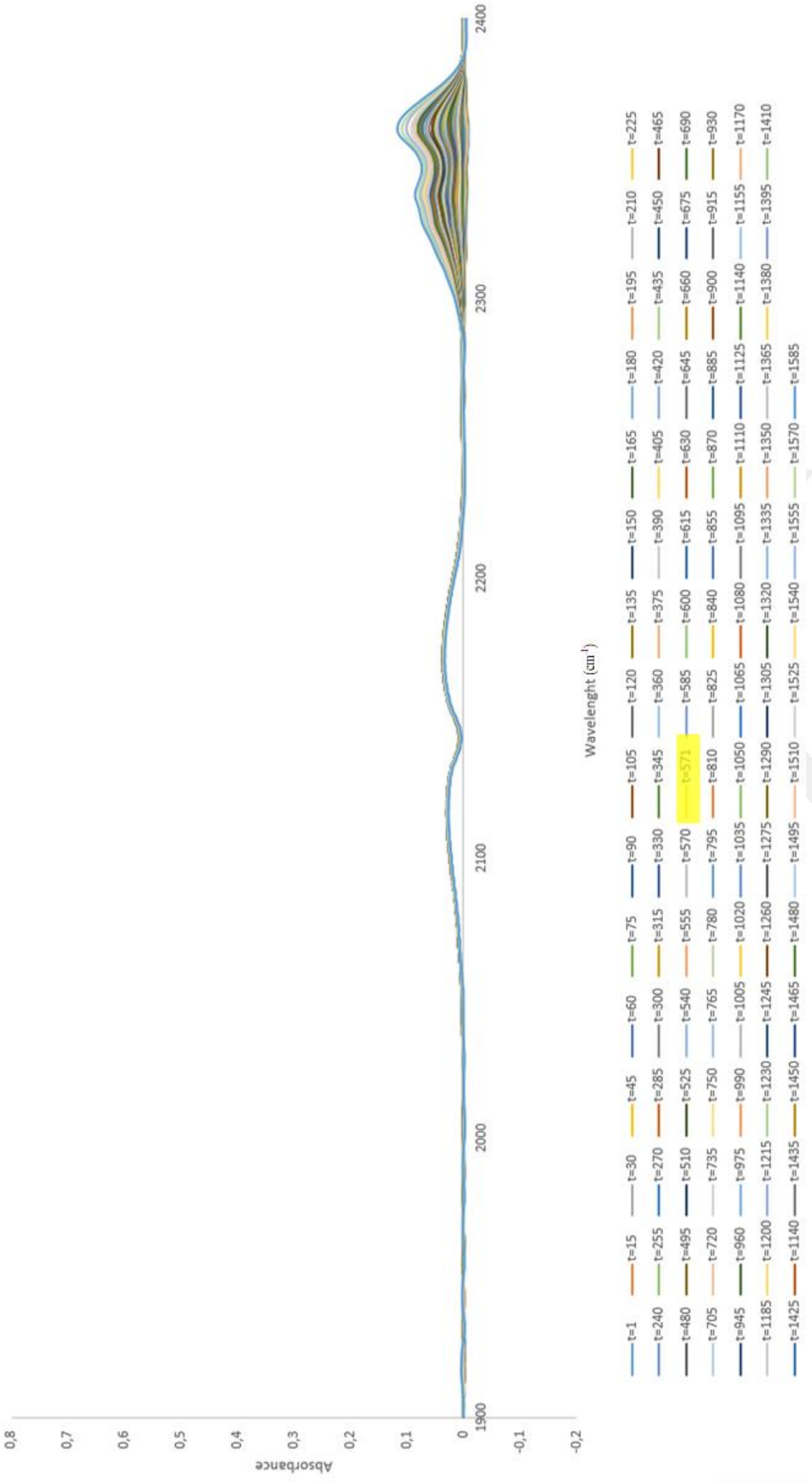

Figure 4.8 The Experiment Results for Without Reactor and Catalyst

The CO and CO_2 concentration with time and percent conversion with respect to time graph can be found in Figure 4.9.

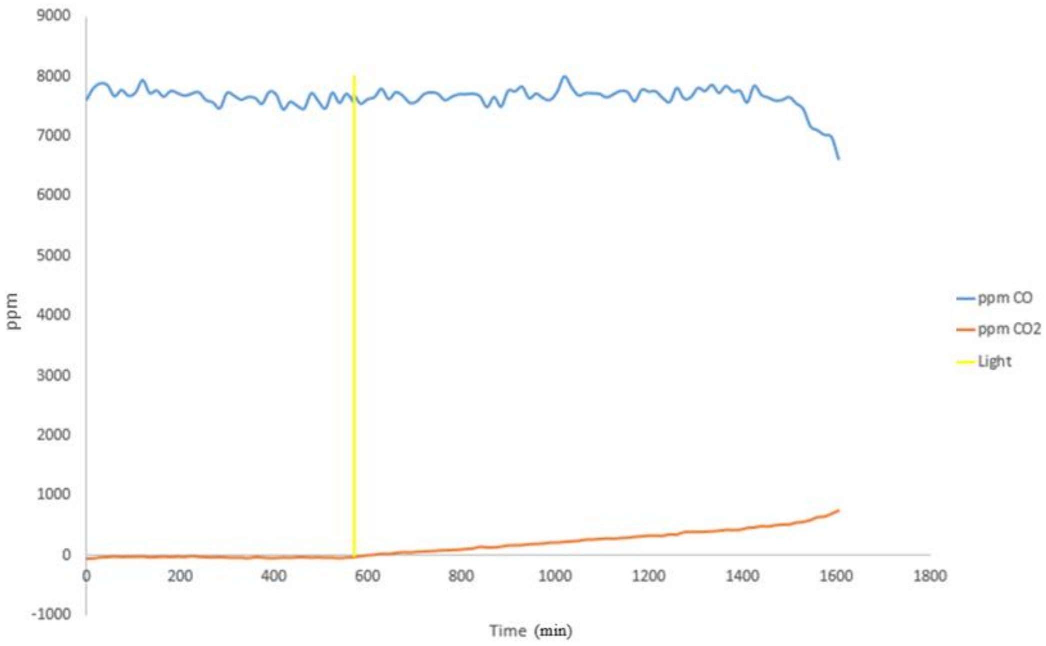

Figure 4.9 CO and CO_2 Concentration vs Time at Room Temperature for w/o Catalyst and w/o Reactor Control Experiment

The slight increase in CO_2 peak intensities, especially under UV illumination, is evidence of the impact of heat. This effect fixed by addition of a cooling period for each experiment. It can be claimed that the connections contribute no further oxidation as CO concentrations have not decreased significantly.

4.3.1.3 Control Experiments with Empty Reactor wo Catalyst Support Experiments

Empty reactors must be inspected in order to detect any disturbances originating from the reactor, such as leakage or oxidation. Consequently, a new experiment planned for this approach.

The catalyst removed from the reactor. The system was subsequently filled with fresh air prior to the experiment. The proper amount of CO gas was injected into the system, and gas recirculation was initiated by activating the diaphragm pump. During the recirculation of CO gas, FT-IR, and OPUS® software monitored the IR bands for CO and CO_2 against a wavenumber range of 1900-2500 cm^{-1}.

To observe the perfect mixing, adsorption of CO on the surface, and the stability of the FT-IR spectrometer, the mixing period of CO with air in the reaction system was conducted and the initial stage of experiments were conducted in the dark. The initial dark period data was fixed at 12 hours. The second phase of the experiments was initiated by turning on the light source in the irradiation chamber after the FT-IR spectrum had assessed the steady conditions. The UV light remained on for 12 hours, beginning at t=720 minutes.

As a summary.

- Dark: 12h
- Light: 12h

In Figure 4.10 the time course of FT-IR spectra of gas phase during the experiment of the catalyst is presented. In Figure 4.11, the separated CO peaks are given.

As it is seen from the spectra, the CO peak intensities decreased in the dark period slightly – which is slightly in between the precision level as it is indicated in the no reactor experiment. The CO_2 value has not changed. After the last dark period, the CO_2 value changes are ignorable.

Thus, it can be concluded that the empty reactor has no effect on CO_2 production and can be used safely. The change of CO absorbance with respect to wavelength for the bare catalyst support data was converted to the CO and CO_2 Concentration vs Absorbance data with the help of the 3rd order calibration equation calculated in the previous sections. The concentration data under room temperature for catalyst afterwards is calculated for the empty reactor.

The data was given in Table A.2 in appendices.

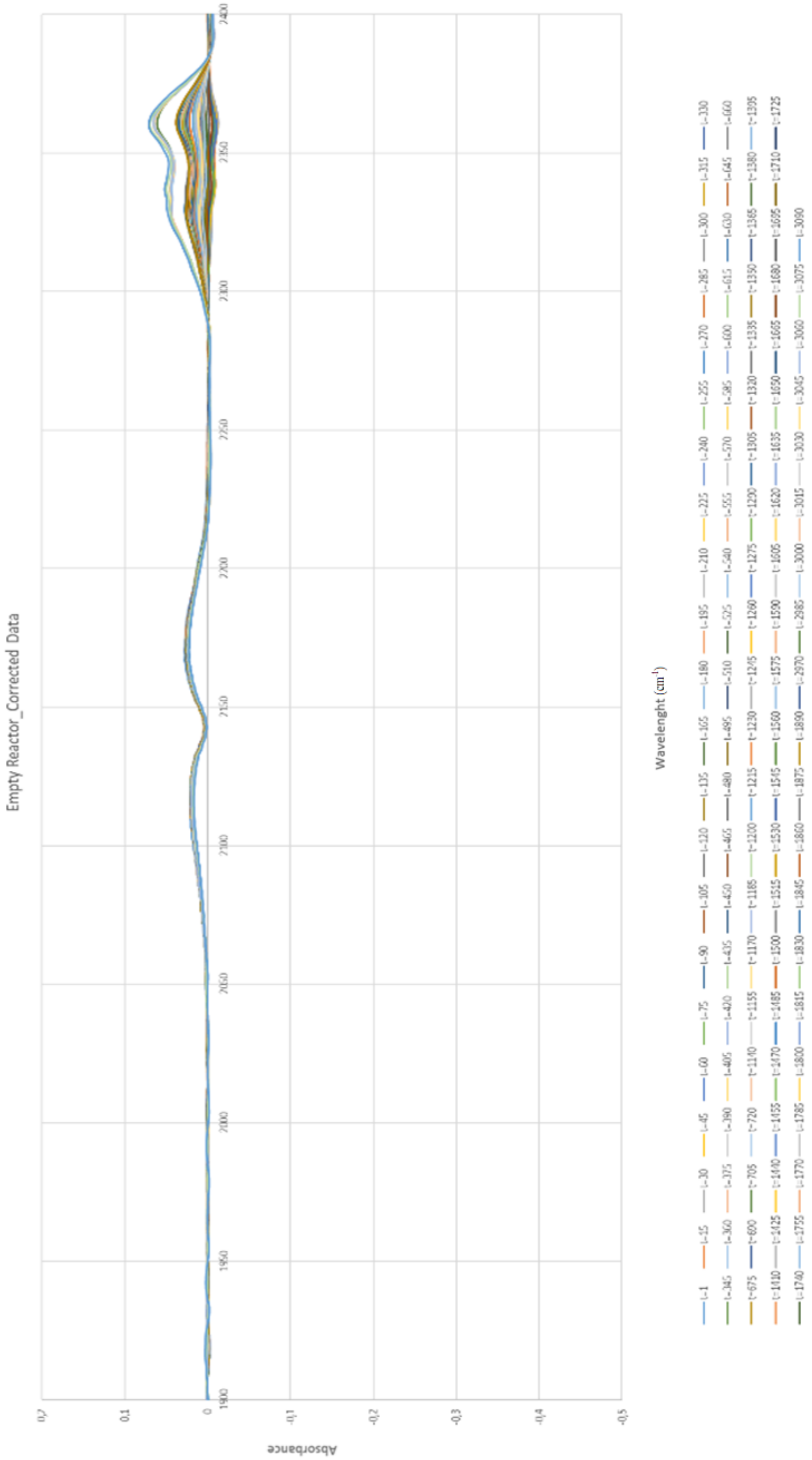

Figure 4.10 The Experiment Results of the Empty Reactor with UVC Lamp

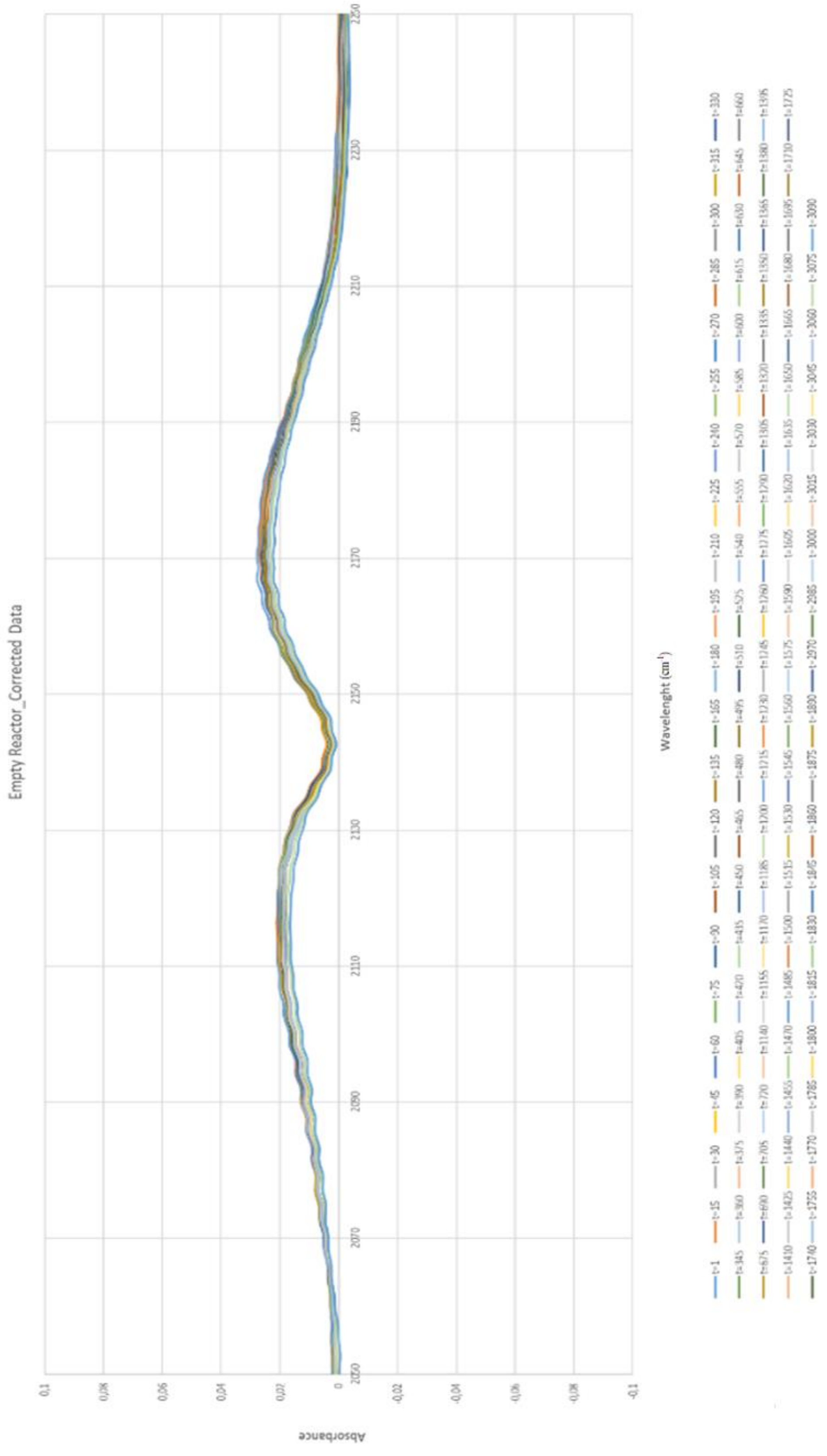

Figure 4.11 CO data extracted from Figure 4.10

The CO and CO_2 concentration with time and percent conversion with respect to time graph can be found in Figure 4.12.

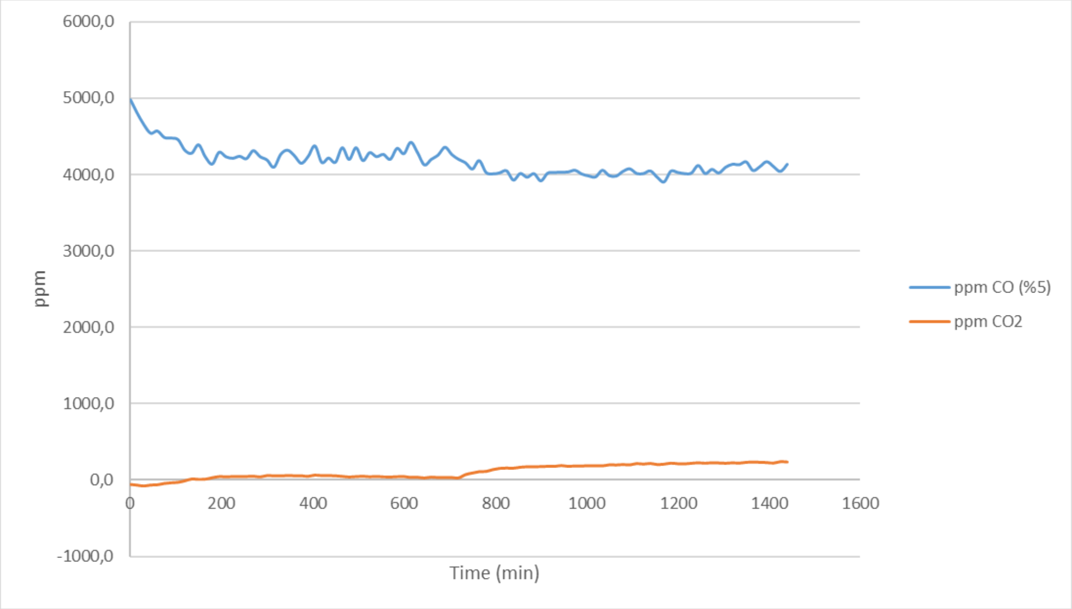

Figure 4.12 CO and CO_2 Concentration vs Time at Room Temperature for Empty Reactor on UVC

It can be concluded that, no additional oxidation comes from the empty reactor itself.

4.3.1.4 Control Experiments with Cellulosic Catalyst Support TiO_2/ SiO_2 C_Ref wo Catalyst Experiments

The catalyst support material is a Cellulose Extraction Thimbles. If any decomposition comes from the non-coated bare filter paper this can results a misleading with the data results. For that purpose, a new control experiment held on.

The catalyst removed from the reactor. And a new bare catalyst support (the cellulose extraction thimble) added to the system. Then, the system was filled with fresh air prior to experiment. The proper volume of CO gas was injected into the system and the gas was started to re-circulate by turning on the diaphragm pump.

During the re-circulation of CO gas, the IR bands for CO and CO_2 against a wavenumber range of 1900-2500 cm^{-1} was followed by FT-IR with the help of OPUS® software.

The mixing period of CO with air in the reaction system was performed and FT-IR spectrometer stability was assured by performing initial stage of experiments in dark to see the perfect mixing, adsorption of CO over the surface and stable FT-IR spectra were obtained during the dark initial period of the experiments. The dark initial period data was fixed to 2h. After the steady conditions assessed by FT-IR spectrum, the second phase of the experiments were started by turning on the UV light source in irradiation chamber. The light kept open for 10h and started at t=121min.

At the end, to eliminate any heat effect from the lamps, the system kept 11h in the dark. With that, the steady conditions have been reached. The dark period at the end kept in 11h.

As a summary.

- Dark: 2h
- Light: 10h
- Dark:11h

In Figure 4.13 the time course FT-IR spectra of gas phase during the experiment of the catalyst is presented. In Figure 4.14, the separated CO peaks are given.

As it is seen from the spectra, the CO peak intensities decreased in the dark period from 5280ppm to 4534ppm (2025-2225 cm^{-1}). After light illuminated the CO peak intensities tend to increase again till 4850ppm. After the dark period at the end the value was kept at 4890ppm. It is higher in comparison to the previous experiments where a decrease observed within the precision limits.

The CO_2 value increased to a little in the dark period (2h) which can be neglected. After light illumination, CO_2 concentration increases to 1080ppm. After the last dark period, the CO_2 value decreased to 957ppm. As a summary CO_2 value increased from 0 ppm to 957ppm.

Without any cellulose filter the CO_2 value at the end was observed as 235ppm. Thus, it can be concluded that the difference directly comes from the bare support material with the CO reactant.

With the aid of the 3rd order calibration equation calculated in the preceding sections, the change in CO absorbance with respect to wavelength for the bare catalyst support data was converted to the CO and CO_2 Concentration vs. Absorbance data. The concentration data at room temperature for the remaining catalyst is calculated for the catalyst support by itself.

The data was given in Table A.3 in appendices.

Figure 4.13 The Experiment Results of the Bare Catalyst Support Material

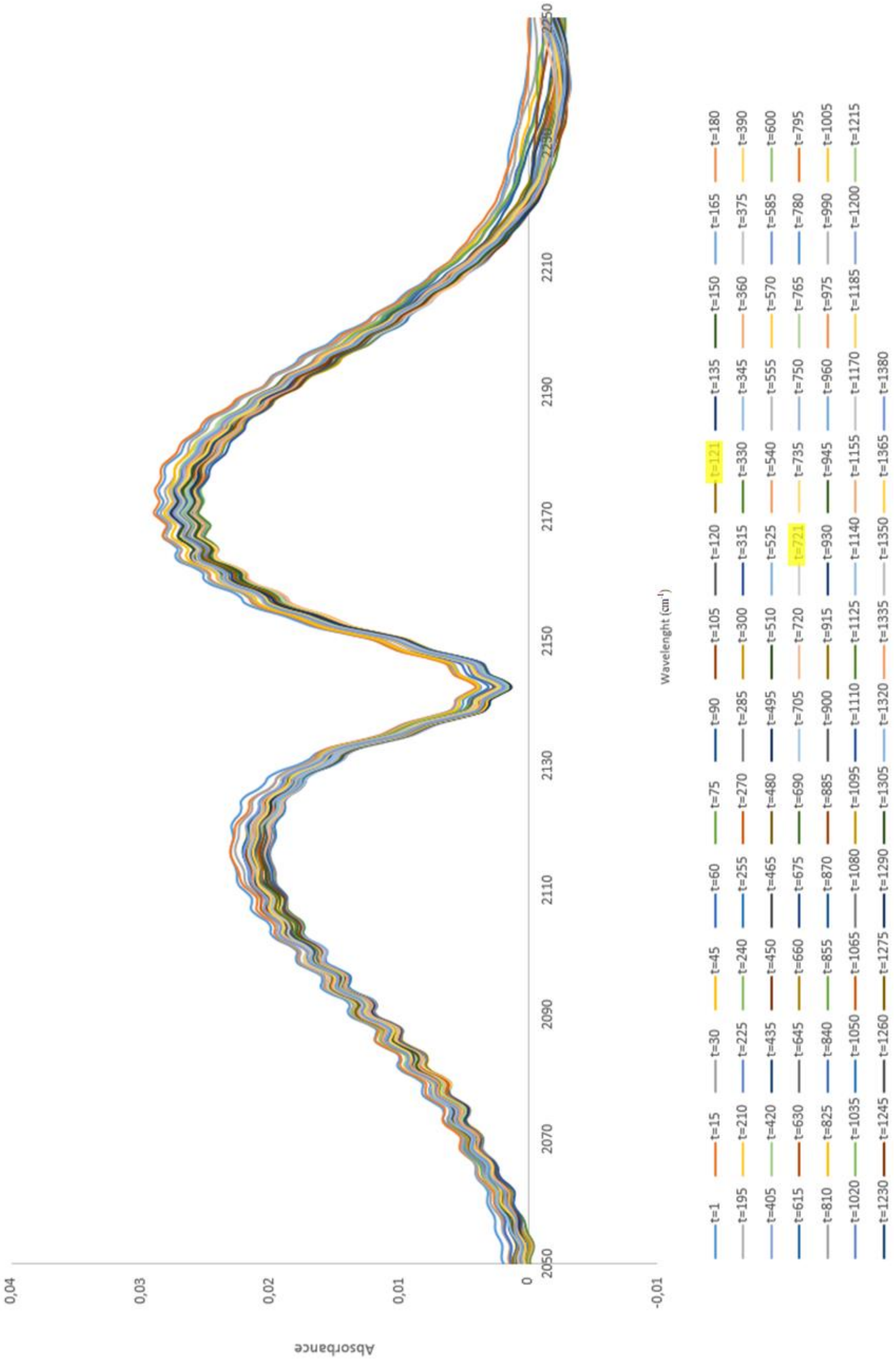

Figure 4.14 CO data extracted from Figure 4.13

The CO and CO_2 concentration with time and percent conversion with respect to time graph can be found in Figure 4.15.

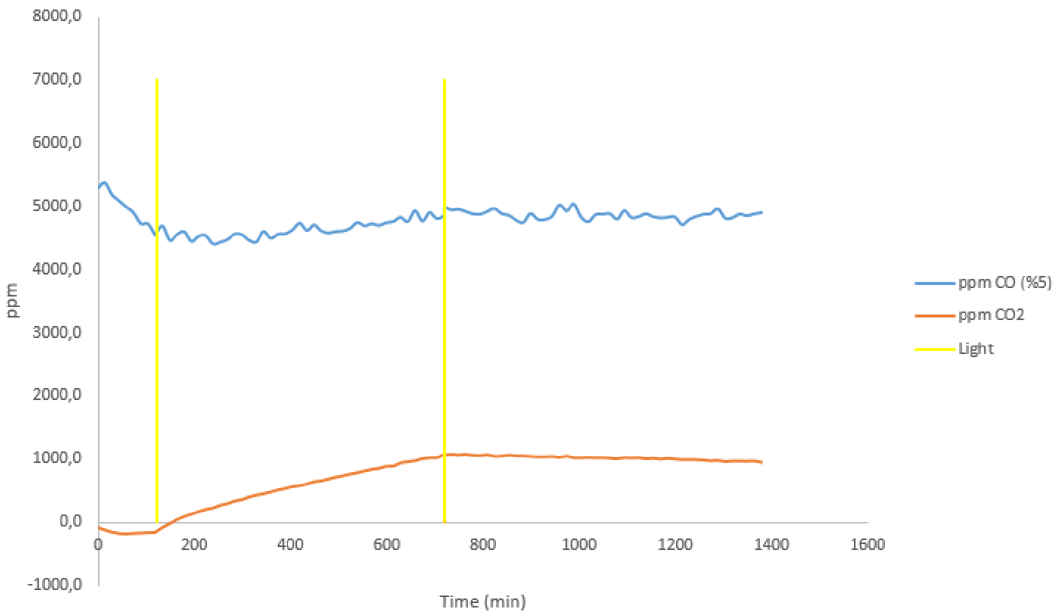

Figure 4.15 CO and CO_2 Concentration vs Time at Room Temperature for Bare Catalyst Support

After exposure to light, the CO_2 absorption bands (2250-2450 cm^{-1}) grew with time. Compared to the data for an empty reactor, the increase in CO_2 peak intensities, particularly in the light, is evidence of additional reaction. With the cooling period, the heat effects are eliminated, yet the decomposition of the cellulose seems obvious.

Under UV irradiation, it can be concluded that there is additional increase in CO_2 and CO from the catalyst support material itself, which are the products of cellulose decomposition. Experiments will be conducted without the addition of CO to determine whether the decomposition directly originates from the substrate or the gas as well.

4.3.1.5 Control Experiments with Bare Cellulosic Catalyst Support TiO_2/SiO_2 C_Ref without CO Experiments

The CO_2 increase in the bare support material should be justified. A new control experiment held by a new reactant (fresh air), and it will be checked if any difference will be detected with comparison to the CO reactant itself.

The catalyst removed from the reactor. And a new bare catalyst support (the cellulose extraction thimble) added to the system. Then, the system was filled with fresh air prior to experiment. That fresh air rinsed the system, and the fresh air was started to re-circulate by turning on the diaphragm pump.

During the re-circulation of fresh room air, the IR bands for CO and CO_2 against a wavenumber range of 1900-2500 cm^{-1} was followed by FT-IR with the help of OPUS® software.

The mixing period of air in the reaction system was performed and FT-IR spectrometer stability was assured by performing initial stage of experiments in dark in order to see the perfect mixing and stable FT-IR spectra were obtained during the dark initial period of the experiments. The dark initial period data was fixed to 2h. After the steady conditions assessed by FT-IR spectrum, the second phase of the experiments were started by turning on the light source in irradiation chamber. The light kept open for 10h and started at t=121min.

At the end, to eliminate any heat effect from the lamps, the system kept 11h in the dark. With that, the steady conditions have been reached. The dark period at the end kept in 11h.

As a summary.

- Dark: 2h
- Light: 10h
- Dark:11h

In Figure 4.16 the time course FT-IR spectra of gas phase during the experiment of the catalyst is presented. In Figure 4.17, the separated CO peaks are given.

The comparison of CO absorbance with calibration work allowed us to observe any adsorption or reaction of CO over the surface in the dark period. As it is seen from the spectra there is no significant CO peak intensities (2025-2225 cm^{-1}) in the dark period. After light illuminated the CO peak intensities tend to increase to 197ppm. After the dark period at the end the value kept increasing and reached 321ppm. This value is the addition CO value for bare cellulose experiment when precision factor eliminated.

The CO_2 value increased to a little in the dark period (2h) which can be neglected. After light illumination, CO_2 concentration increases to 1102ppm. After the last dark period, the CO_2 value decreased to 1036ppm. As a summary CO value increased from 0 ppm to 1036ppm.

Without any cellulose filter and CO intake the CO value should be remained zero at the end, but it was observed as 321ppm. Thus, it can be concluded that cellulose burned into CO and some CO_2 as well.

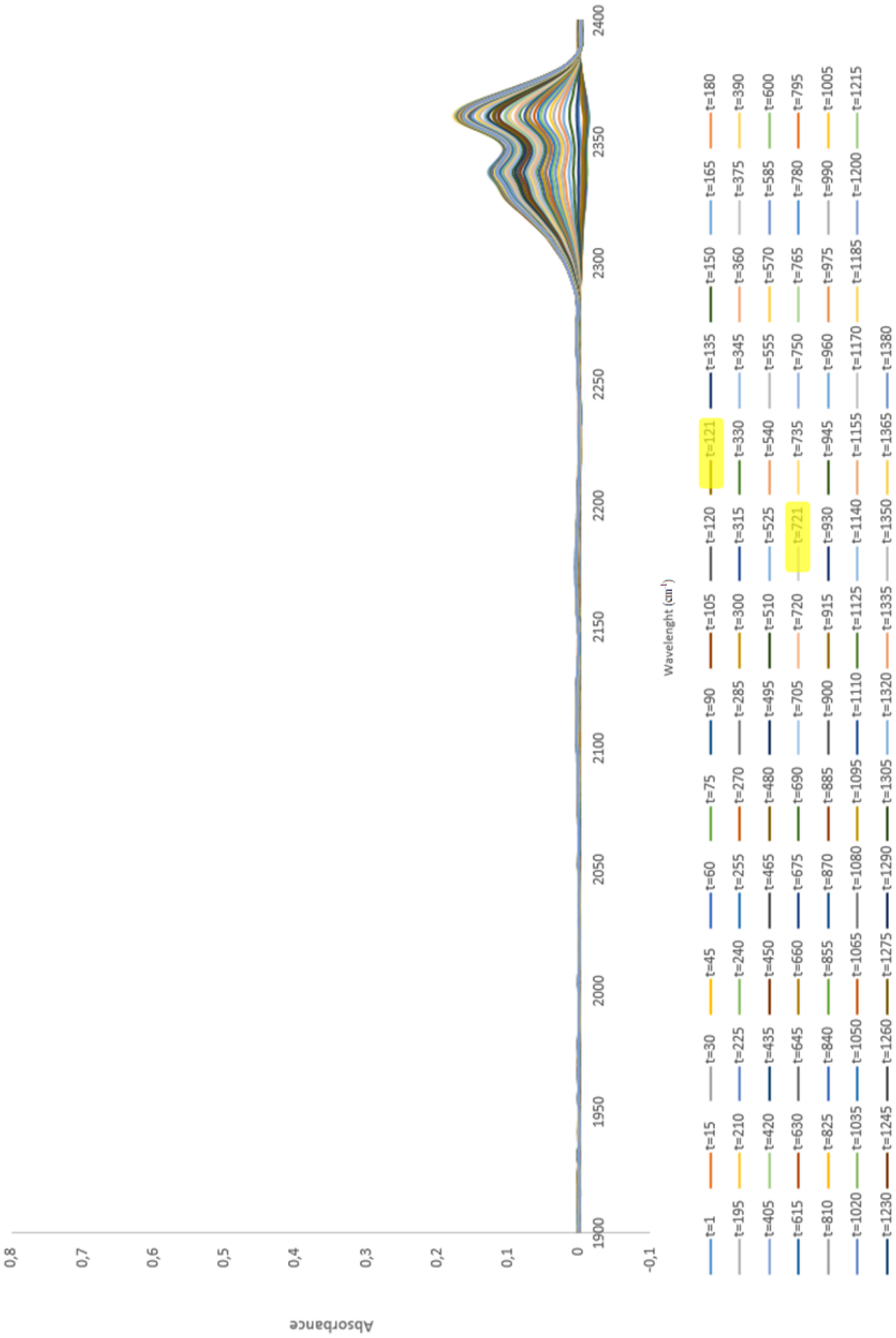

Figure 4.16 The Experiment Results of the Bare Cellulose Support wo CO

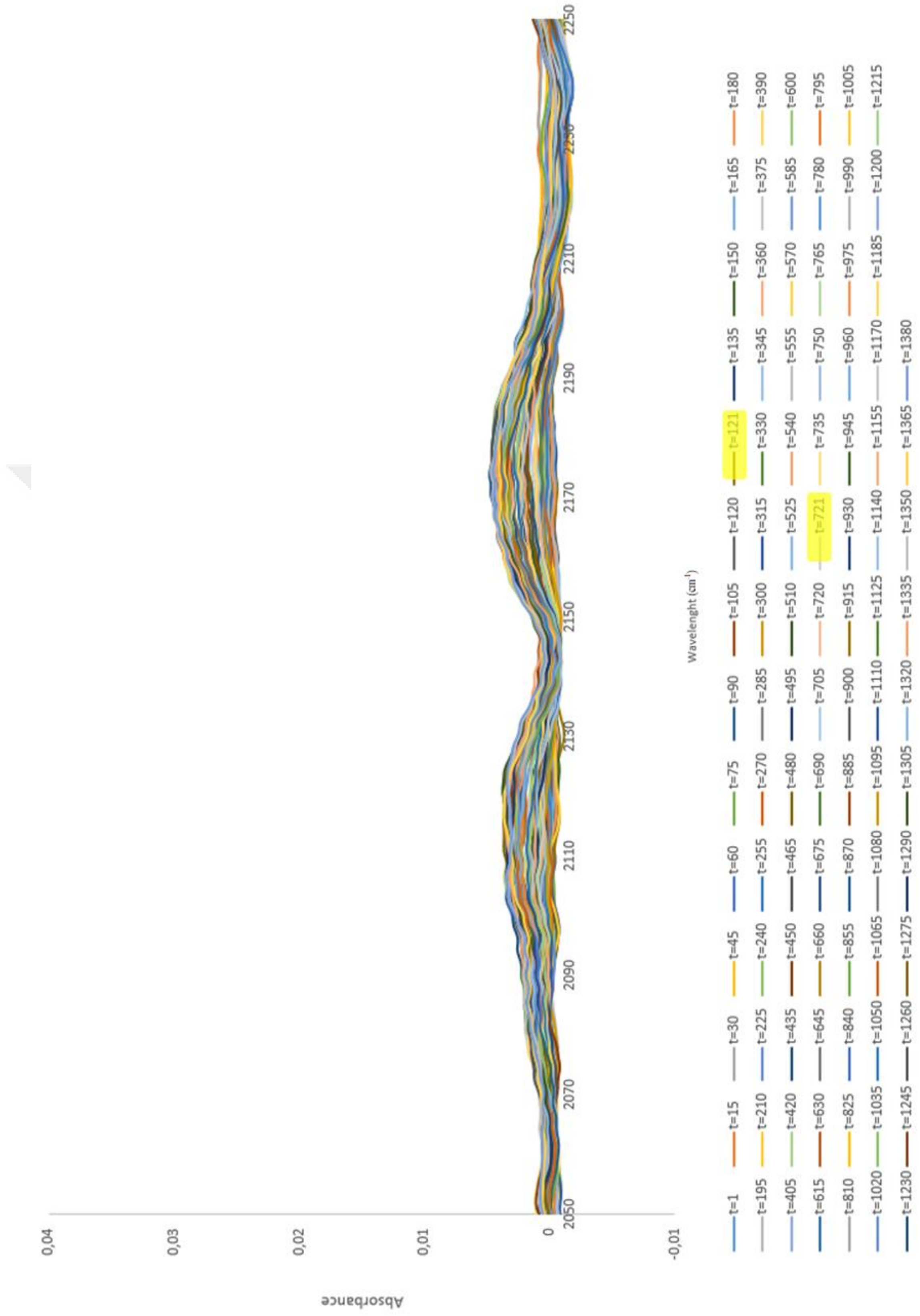

Figure 4.17 CO data extracted from Figure 4.16

With the assistance of the 3rd order calibration equation calculated in the preceding sections, the change in CO absorbance with respect to wavelength for the bare catalyst support data was converted to the CO and CO_2 Concentration vs. Absorbance data. The concentration data at room temperature for the remaining catalyst is calculated for the catalyst support alone.

The data was given in Table A.4 in appendices.

The CO and CO_2 concentration with time and percent conversion with respect to time graph can be found in Figure 4.18.

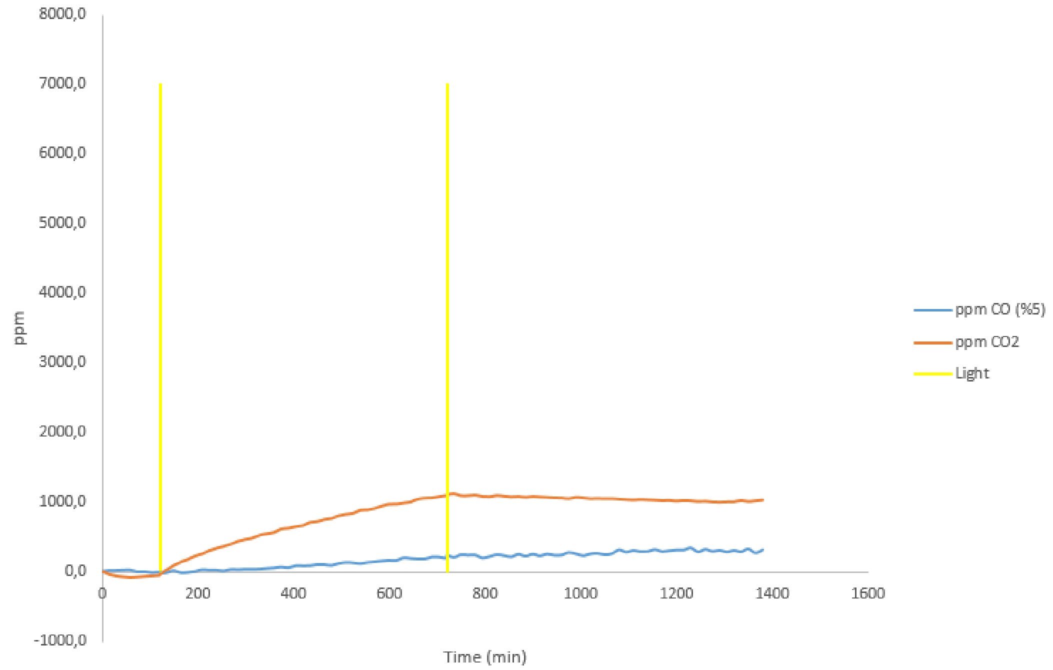

Figure 4.18 CO and CO_2 Concentration vs Time at Room Temperature for Bare Cellulose Catalyst Support wo CO

As a summary, after exposure to light, the CO_2 absorption bands (2250-2450 cm^{-1}) increased with time. The increase in CO_2 peak intensities, particularly in the light, is evidence of additional reaction when compared to data from a reactor that was empty and bare cellulose support material. With the cooler and the cooling period, the heat effects were also eliminated, but the decomposition of the cellulose seems obvious.

Under UV irradiation, it can be concluded that there is an additional increase in CO_2 and CO from the catalyst support material itself, which is cellulose. The increase in CO peak intensities demonstrates that the bare cellulose support decomposed to CO and CO_2 following illumination.

4.3.1.6 Sample TiO_2/SiO_2 C_3 without CO Experiments

After the conclusion in the previous section, the catalyst coated support material has been assessed without any CO intake to see any additional CO comes from the catalyst impurities or not.

The catalyst put into the reactor. Then, the system was filled with fresh air prior to experiment. That fresh air rinsed the system, and the fresh air was started to re-circulate by turning on the diaphragm pump.

During the re-circulation of fresh room air, the IR bands for CO and CO_2 against a wavenumber range of 1900-2500 cm^{-1} was followed by FT-IR with the help of OPUS® software.

The mixing period of air in the reaction system was performed and FT-IR spectrometer stability was assured by performing initial stage of experiments in dark to see the perfect mixing and stable FT-IR spectra were obtained during the dark initial period of the experiments. The dark initial period data was fixed to 2h. After the steady conditions assessed by FT-IR spectrum, the second phase of the experiments were started by turning on the light source in irradiation chamber. The light kept open for 10h and started at t=121min.

At the end, to eliminate any heat effect from the lamps, the system kept 11h in the dark. With that, the steady conditions have been reached. The dark period at the end kept in 11h.

As a summary.

- Dark: 2h
- Light: 10h
- Dark: 11h

In Figure 4.19 the time course FT-IR spectra of gas phase during the experiment of the catalyst is presented. In Figure 4.20, the separated CO peaks are given.

The comparison of CO absorbance with calibration work allowed us to observe any adsorption or reaction of CO over the surface in the dark period. As it is seen from the spectra there is no significant CO peak intensities (2025-2225 cm^{-1}) in the dark period. After light illuminated the CO peak intensities tend to increase. After the dark period at the end the value kept increasing and reached 863ppm.

Whereas The CO_2 value increased to a little in the dark period (2h) which can be neglected. After light illumination, CO_2 concentration increases to 5188ppm. After the last dark period, the CO_2 value decreased to 4634ppm. As a summary CO value increased from 0ppm to 4634ppm.

Without any cellulose filter and CO intake the CO value should be remained zero at the end, but it was observed as 853ppm. Thus, it can be concluded that the HC inside the catalyst due to (not-calcination) burned into CO and much more CO_2 as well and catalyst favors the decomposition reaction of cellulose.

The change of CO absorbance with respect to wavelength for the bare catalyst support data was converted to the CO and CO_2 Concentration vs Absorbance data with the help of the 3rd order calibration equation calculated in the previous sections. The concentration data under room temperature for catalyst afterwards is calculated for the bare catalyst support.

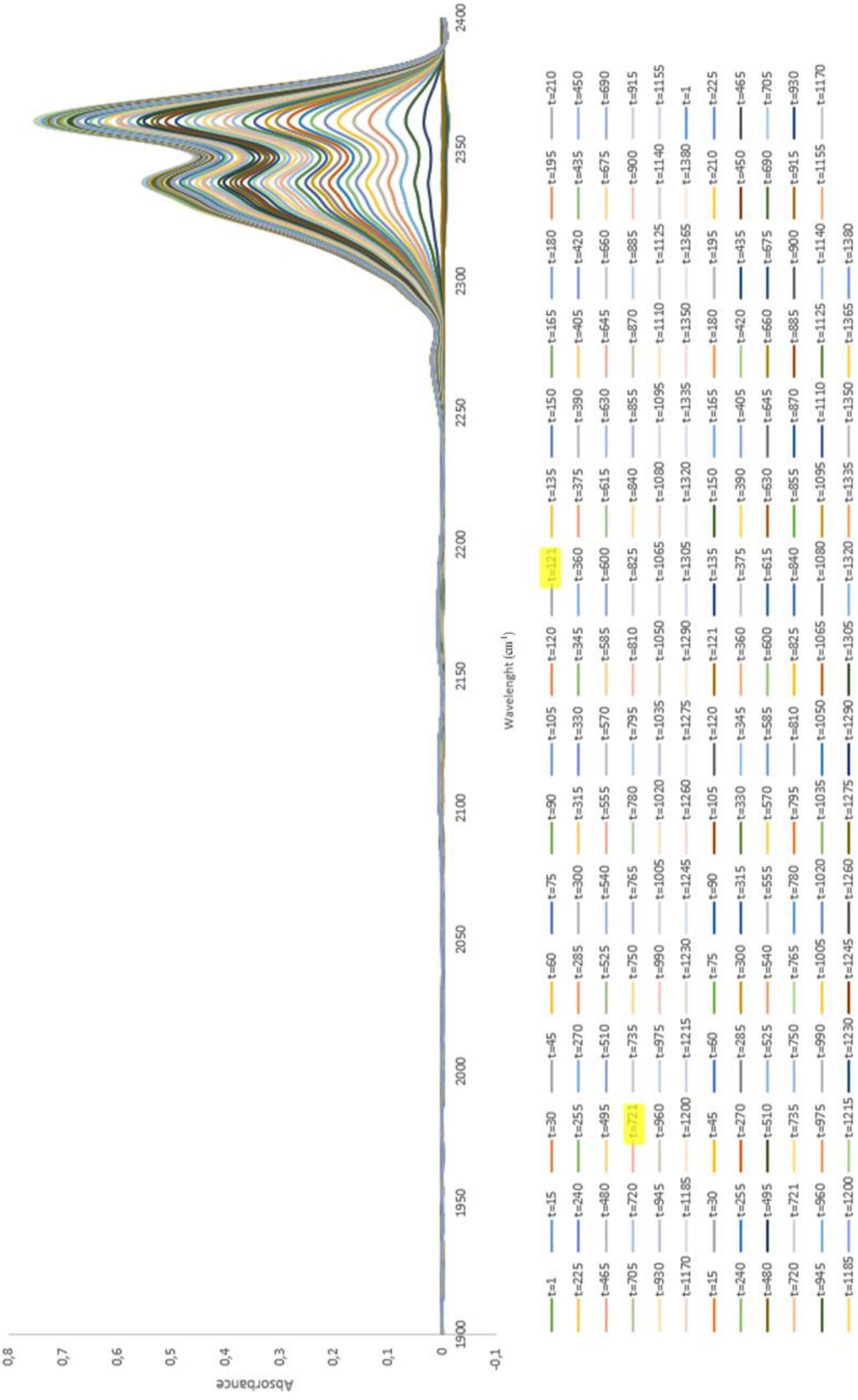

Figure 4.19 The Experiment Results of the Catalyst TiO_2/SiO_2 C_3 wo CO

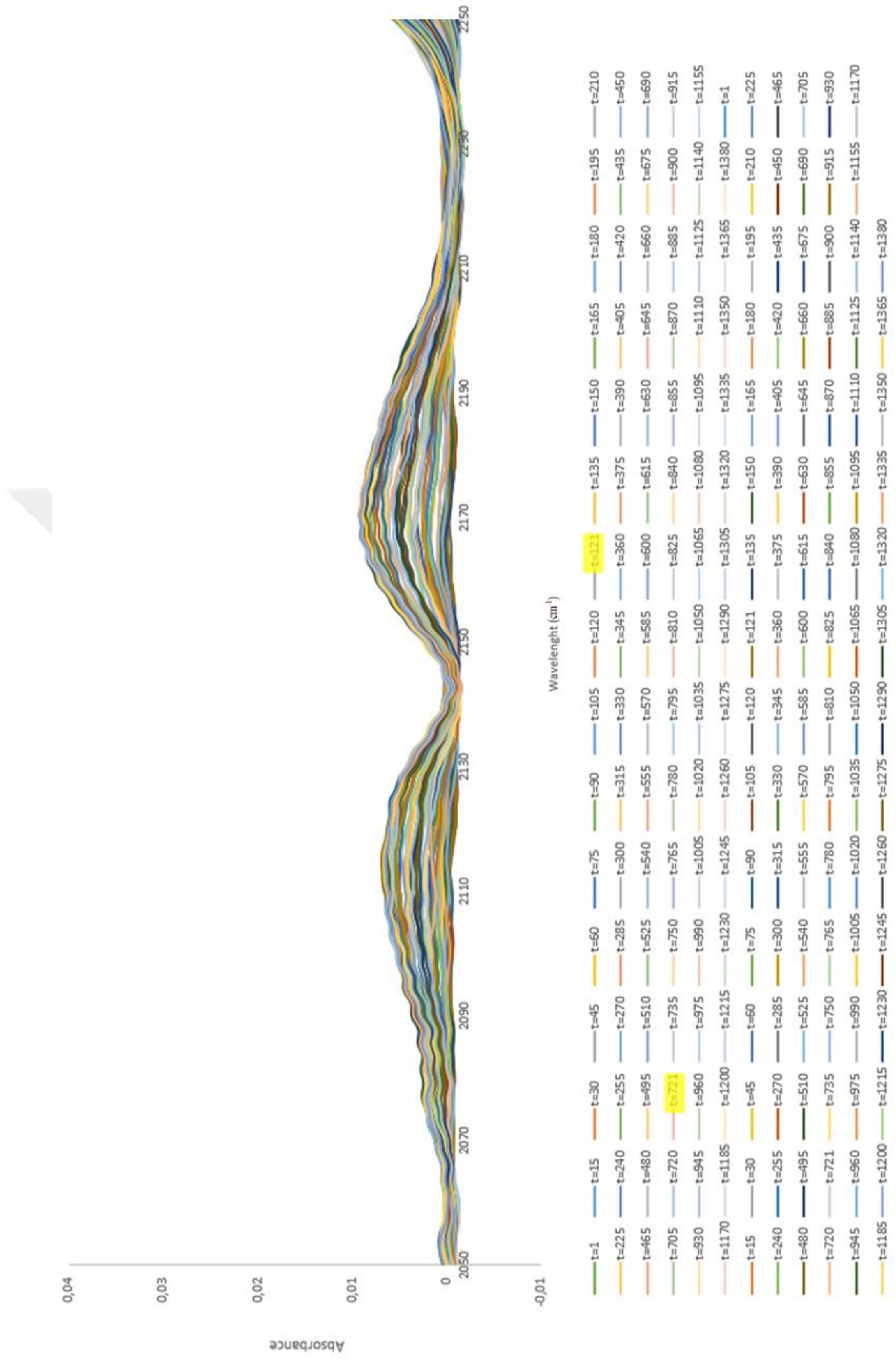

Figure 4.20 CO data extracted from Figure 4.19

The data was given in Table A.5 in Appendices.

The CO and CO_2 concentration with time and percent conversion with respect to time graph can be found in Figure 4.21.

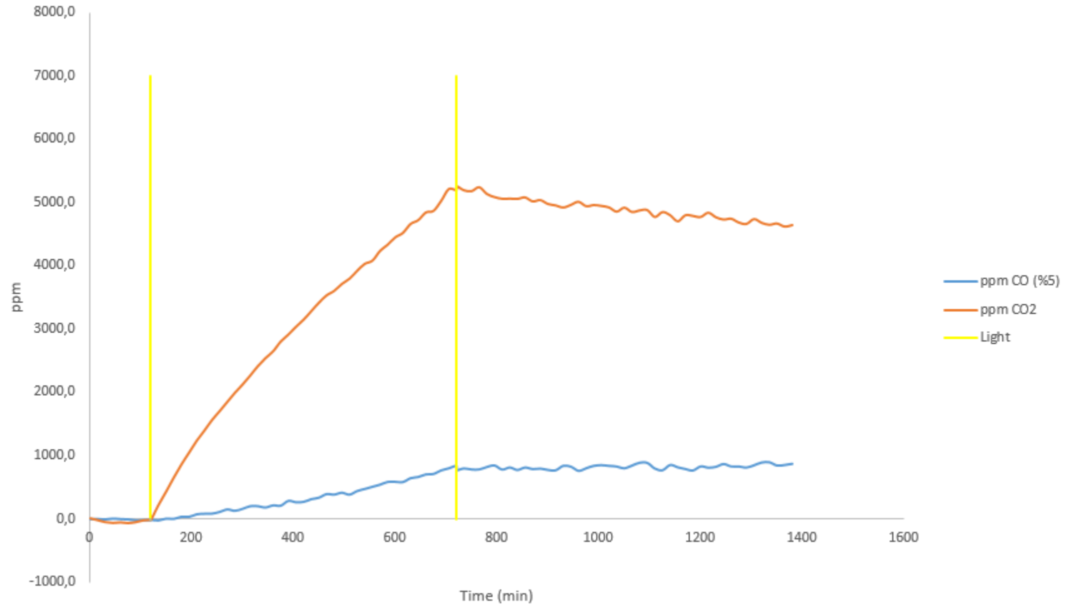

Figure 4.21 CO and CO_2 Concentration vs Time at Room Temperature for the Catalyst TiO_2/SiO_2 C_3

As a summary, after light illumination the CO_2 absorption bands (2250-2400 cm^{-1}) increased by time. The increase in the CO_2 peak intensities, especially in the light, is the evidence of the heat effect and additional reaction with comparison to the empty reactor and bare support material data. The heat effects also eliminated with the cooling period and the decomposition of the cellulose itself seems obvious.

It can be concluded that, there is an additional CO_2 and CO increase from the bare catalyst support material which comes from the cellulose itself under UV irradiation. The increase in the CO peak intensities show that the bare support produces CO and CO_2 after the light illumination.

This increase is more than the bare support; thus, this can be also concluded that there are some HCs tend to burn into CO and CO_2 with light illumination and catalyst favors the decomposition of cellulose.

A new catalyst support needed to be worked to eliminate the CO and CO_2 emissions which came from Cellulose itself. A new catalyst support is worked for further analysis, which is stainless steel wire mesh.

4.3.1.7 Control Experiments with Stainless Steel Wire Mesh Support under UV Irradiation TiO_2/SiO_2 S Ref

In order to understand the catalytic performance of the catalyst a bare support material test is a necessity when there may be an additional oxidation possibility as in the previous cellulose support. Thus, for that manner a new experiment has been planned. The lamp was remained during the experiments as UVC.

The catalyst removed from the reactor. And a new bare catalyst support (stainless steel mesh) added to the system. Then, the system was filled with fresh air prior to experiment. The proper volume of CO gas was injected into the system and the gas was started to re-circulate by turning on the diaphragm pump.

During the re-circulation of CO gas, the IR bands for CO and CO_2 against a wavenumber range of 1900-2500 cm^{-1} was followed by FT-IR with the help of OPUS® software.

The mixing period of CO with air in the reaction system was performed and FT-IR spectrometer stability was assured by performing initial stage of experiments in dark to see the perfect mixing, adsorption of CO over the surface and stable FT-IR spectra were obtained during the dark initial period of the experiments. The dark initial period data was fixed to 1h. After the steady conditions assessed by FT-IR spectrum, the second phase of the experiments were started by turning on the light source in irradiation chamber. The light kept open for 8,5h and started at t=61min.

At the end, to eliminate any heat effect from the lamps, the system kept 11h in the dark. With that, the steady conditions have been reached. The dark period at the end kept in 11h.

As a summary.

- Dark: 1h
- Light: 8,5h

In Figure 4.22 the time course FT-IR spectra of gas phase during the experiment of the catalyst is presented. In Figure 4.23, the separated CO peaks are given.

The comparison of CO absorbance with calibration work allowed us to observe any adsorption or reaction of CO over the surface in the dark period. As it is seen from the spectra, the CO peak intensities decreased slightly which is negligible as the empty reactor data in the dark period.

Whereas The CO_2 value has not changed. After the last dark period, the CO_2 value changes are ignorable. Without any catalyst the CO_2 value increase is also negligible. Thus, it can be concluded that the 304 stainless-steel wire mesh support material has no effect on CO_2 production and can be used safely.

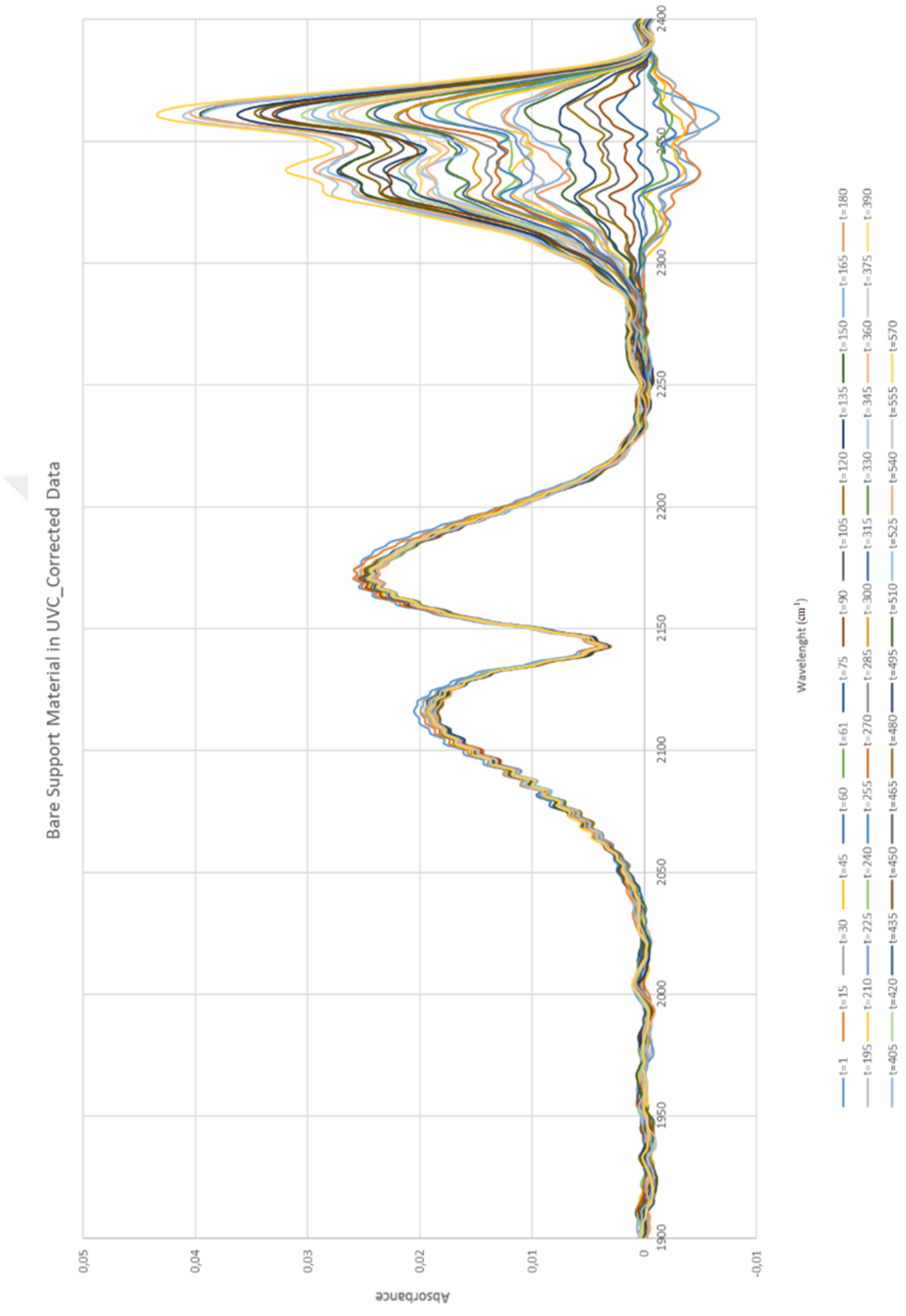
Bare Support Material in UVC_Corrected Data
Absorbance
0,05
0,04
0,03
0,02
0,01
0
-0,01
1900
1950
2000
2050
2100
2150
2200
2250
2300
2350
2400
Wavelenght (cm-1)
t=1
t=15
t=30
t=45
t=60
t=61
t=75
t=90
t=105
t=120
t=135
t=150
t=165
t=180
t=195
t=210
t=225
t=240
t=255
t=270
t=285
t=300
t=315
t=330
t=345
t=360
t=375
t=390
t=405
t=420
t=435
t=450
t=465
t=480
t=495
t=510
t=525
t=540
t=555
t=570

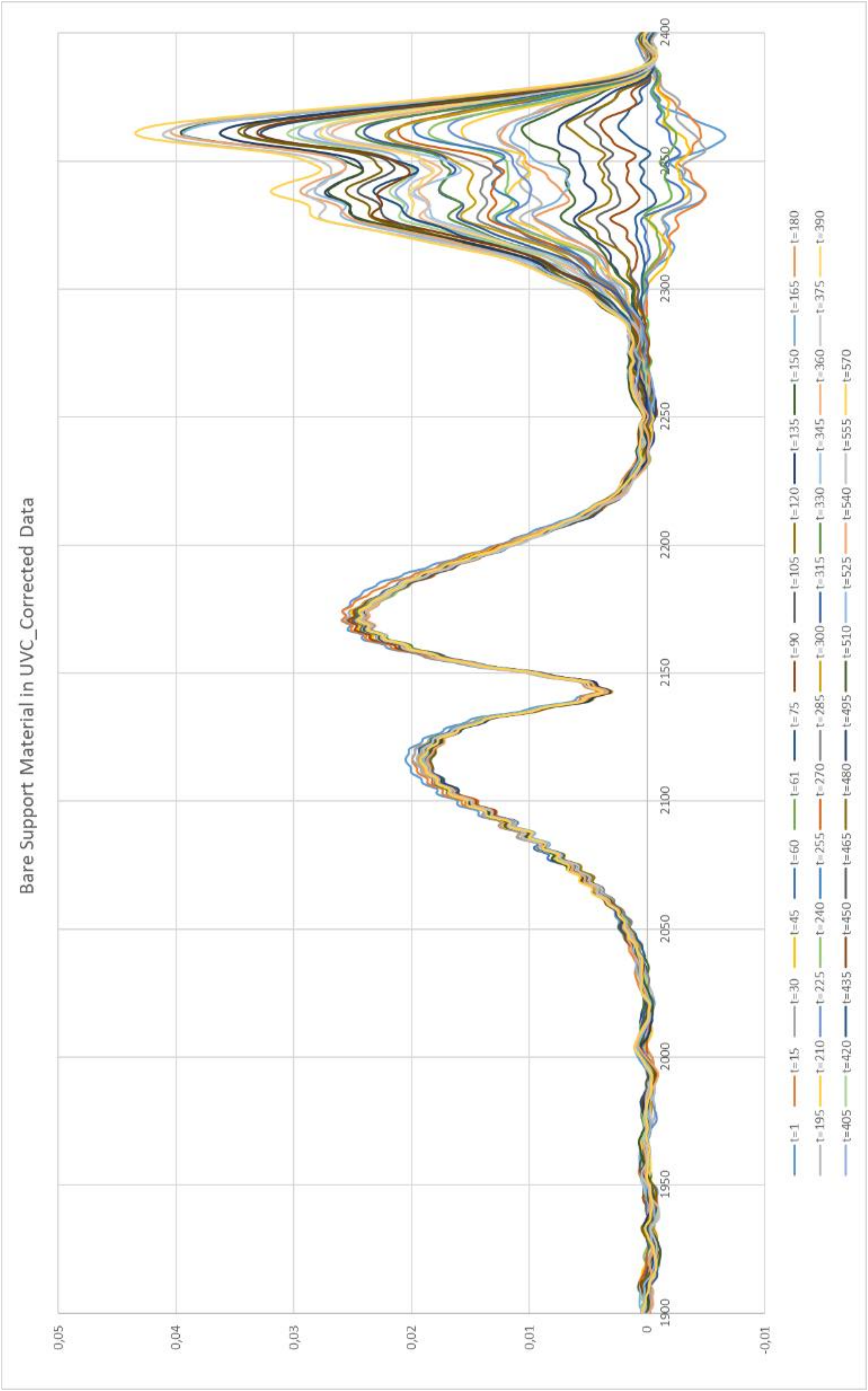

Figure 4.22 The Experiment Results of the Bare Catalyst Stainless Steel Support Material under UVC

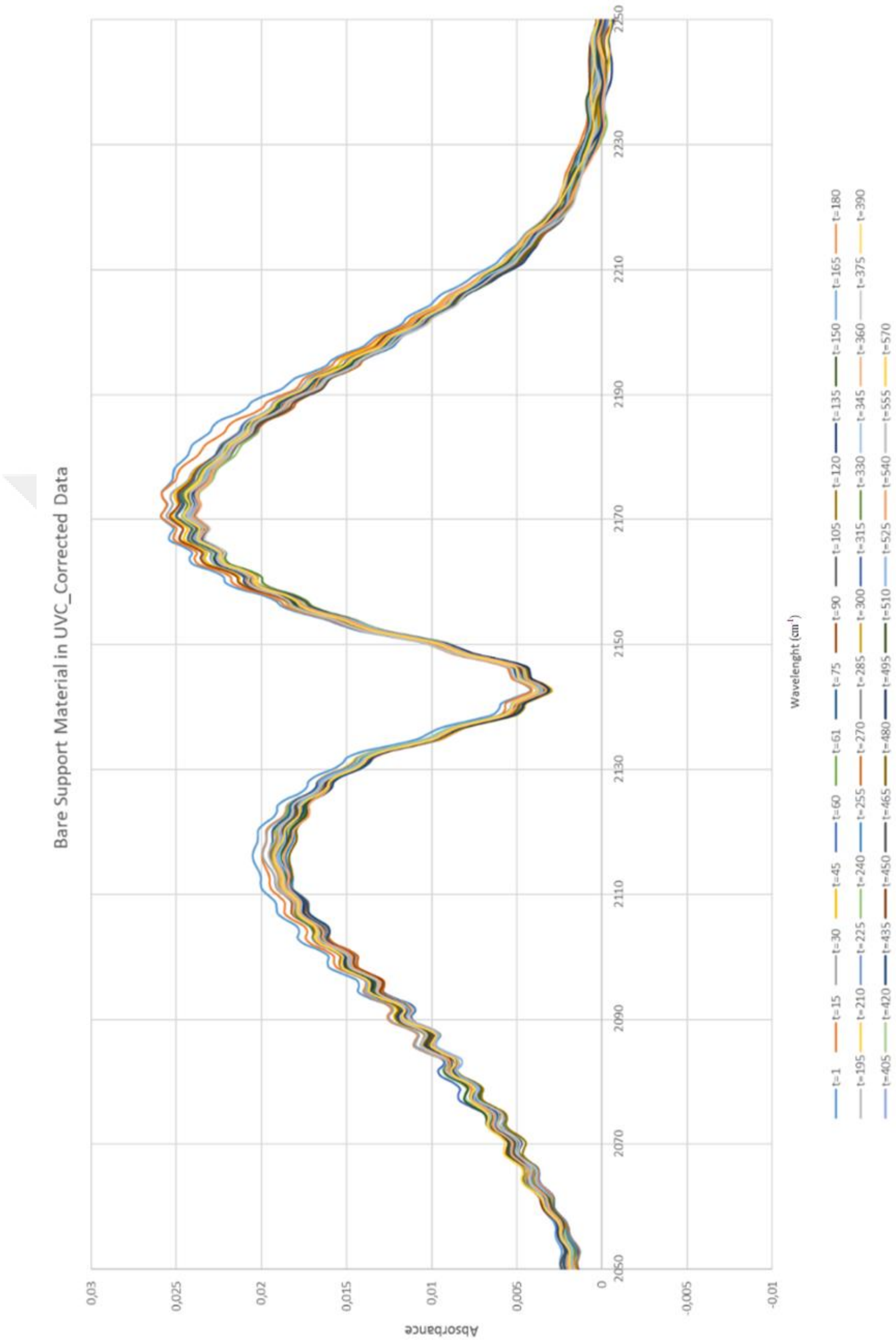

Figure 4.23 CO data extracted from Figure 4.22

The change of CO absorbance with respect to wavelength for the bare catalyst support data was converted to the CO and CO_2 Concentration vs Absorbance data with the help of the 3^{rd} order calibration equation calculated in the previous sections. The concentration data under room temperature for catalyst afterwards is calculated for the bare catalyst support.

The data was given in Table A.6 in appendices.

The CO and CO_2 concentration with time and percent conversion with respect to time graph can be found in Figure 4.24.

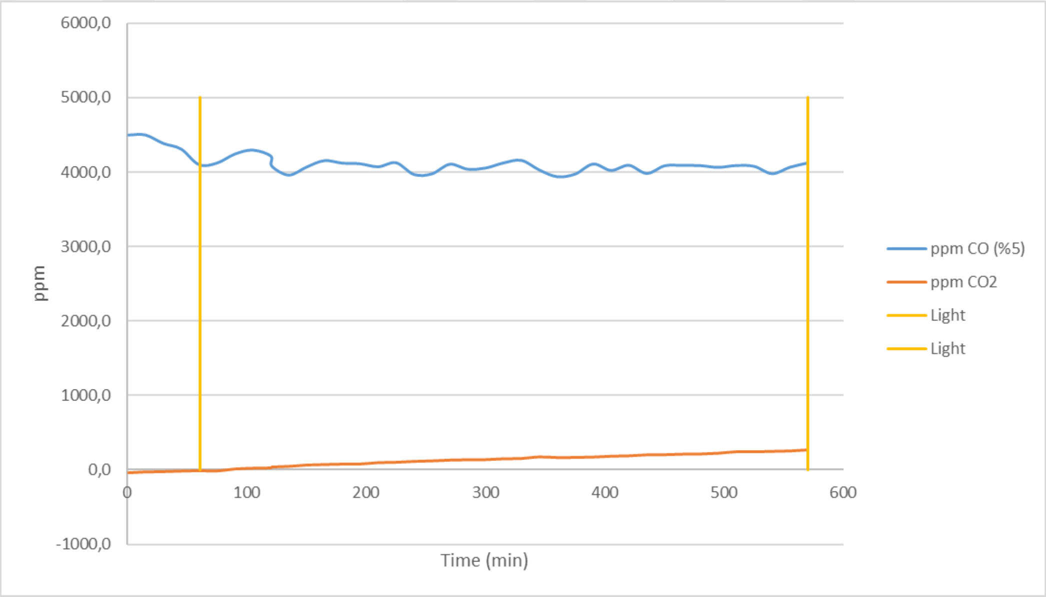

Figure 4.24 CO and CO_2 Concentration vs Time at Room Temperature for Bare Catalyst Stainless Steel Support on UVC

This stainless-steel wire mesh catalyst support material can be worked in order to understand the catalyst performance safely.

4.3.2 Photocatalytic Activity Results of the Catalyst on Different Support Materials Under UV Irradiation

4.3.2.1 TiO_2/SiO_2 C_3 Sample Photocatalytic Activity Test Results

The details of the system, the methodology for quantitative measurement of CO and CO_2 by using FT-IR spectrometer and the photocatalytic activity tests were explained in detail in Section 3.

The preliminary photocatalytic activity tests were performed by using the re-circulated closed system of the reactor coupled with FT-IR cell with the renewed system.

The catalyst TiO_2/ SiO_2 C_3 was used as the sample. The sample was placed in the reactor which was filled with fresh air prior to experiment. The proper volume of CO gas was injected into the reactor system with 4 Teflon samples and the gas was started to re-circulate by turning on the diaphragm pump.

During the re-circulation of CO gas, the IR bands for CO and CO_2 against a wavenumber range of 1900-2500 cm^{-1} was followed by FT-IR with the help of OPUS® software.

The mixing period of CO with air in the reaction system was performed and FT-IR spectrometer stability was assured by performing initial stage of experiments in dark to see the perfect mixing, adsorption of CO over catalyst surface and stable FT-IR spectra were obtained during the dark initial period of the experiments. The dark initial period data was fixed to 2h. After the steady conditions assessed by FT-IR spectrum, the second phase of the experiments were started by turning on the light source in irradiation chamber. The UV light kept open for 10h and started at t=121mins. After the light illumination, the light source switched off and the system kept 11h in dark again and started at t=721mins. With that, any increase in the temperature that caused by the light source is eliminated at the end.

As a summary.

- Dark: 2h
- Light: 10h
- Dark: 11h

In Figure 4.25 the time course FT-IR spectra of gas phase during the experiment of the catalyst is presented. In Figure 4.26, the separated CO peaks are given.

The comparison of CO absorbance with calibration work allowed us to observe any adsorption of CO over the catalyst surface in the dark period. As it is seen from the spectra, a considerable decrease was observed on the CO peak intensities in the dark period (2025-2225 cm^{-1}).

After light illumination, the CO_2 absorption bands (2250-2400 cm^{-1}) increased by time. The increase in the CO_2 peak intensities, especially in the light, is the evidence of the photo-oxidation. After light illumination, the CO adsorption peaks tend to increase which shows the desorption of the gas on the catalyst surface with heat and light. The increase continues as the CO_2 levels increase as well.

The CO decreased from 5120pm to 4585ppm in the dark period (2h). After light illumination, CO concentration increases to 5858ppm, which is more than the initial value. After the last dark period, the CO value decreased to 5556ppm. As a summary CO value increased from 5120ppm to 5556ppm.

Whereas The CO_2 value increased to 100ppm in the dark period (2h). After light illumination, CO_2 concentration increases to 5340ppm. After the last dark period, the CO_2 value decreased to 4855ppm. As a summary CO value increased from 0 ppm to 4855ppm.

The CO and CO_2 conversion should be equal at the end because of the stoichiometric ratio of the below reaction.

$$2\ CO(g) + O_2(g) \rightleftharpoons 2\ CO_2(g)$$

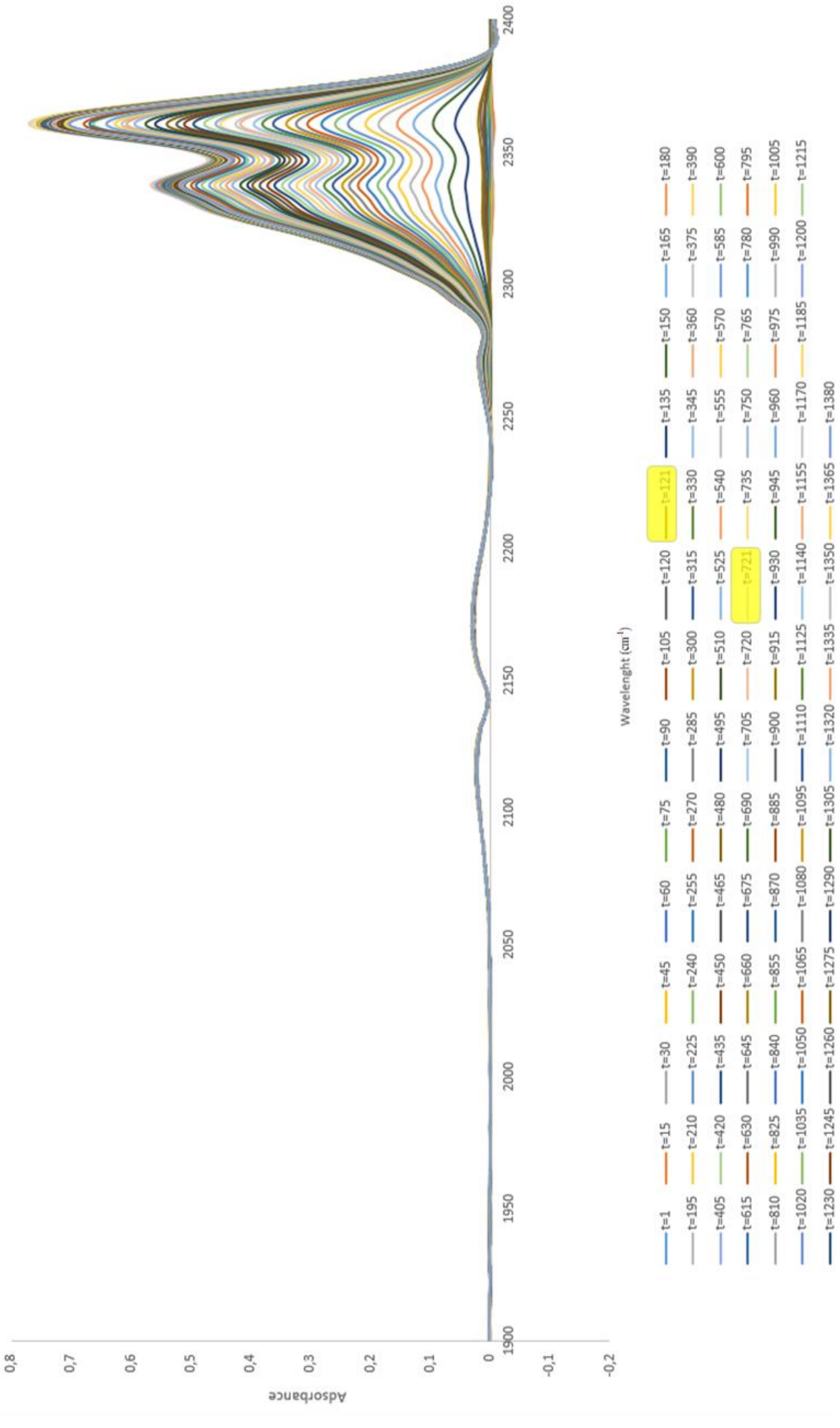

Figure 4.25 The Experiment Results Sample TiO_2/SiO_2 C_3

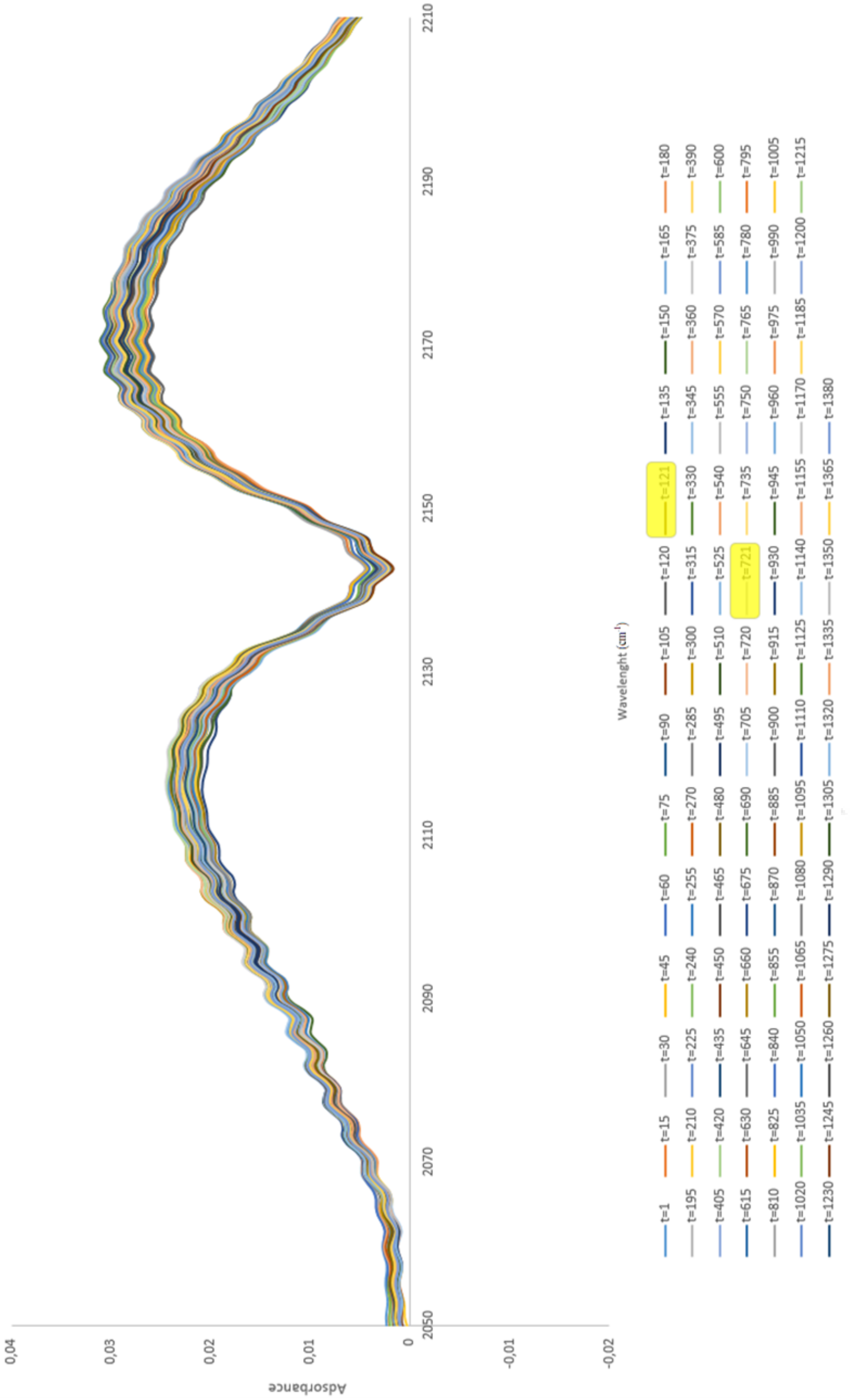

Figure 4.26 CO data extracted from Figure 4.25

The change of CO absorbance with respect to wavelength for TiO_2/ SiO_2 C_3 catalyst was converted to the CO, CO_2 Concentration vs Absorbance data with the help of the 3rd order calibration equation observed in the previous sections. The concentration data under room temperature for catalyst afterwards is calculated for TiO_2/ SiO_2 C_3. The light illuminated at t=121min.

The data was given in Table A.7 in appendices.

The CO and CO_2 concentration with respect to time graph can be found in Figure 4.27.

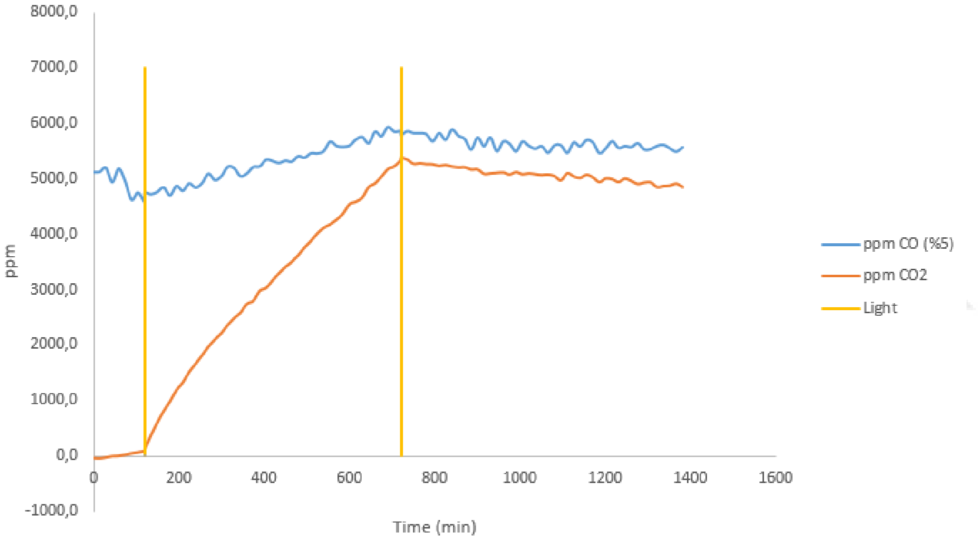

Figure 4.27 CO and CO_2 Concentration vs Time at Room Temperature for Sample TiO_2/SiO_2 C_3

As it is indicated in the control experiments, the CO and CO_2 increase is the evidence of the cellulose decomposition under UV irradiation. With the catalyst addition the concentration of CO and CO_2 is also increases, this shows that the catalyst is active and decomposes cellulose instead of CO in the glass cylinder.

The results are to be compared with the results by stainless steel wire mesh substrate.

4.3.2.2 TiO_2/SiO_2 S_1 Sample (Without Calcination) Photocatalytic Activity Test Results

The bare solution synthesis method was discussed in the Chapter 3. The stainless-steel wire mesh sample was not calcined prior to the experiment to see any impurities in the solution which may mislead the results.

The sample was placed in the reactor which was filled with fresh air prior to experiment. The proper volume of CO gas was injected into the reactor system and the gas was started to re-circulate by turning on the diaphragm pump.

During the re-circulation of CO gas, the IR bands for CO and CO_2 against a wavenumber range of 1900-2500 cm^{-1} was followed by FT-IR with the help of OPUS® software.

The mixing period of CO with air in the reaction system was performed and FT-IR spectrometer stability was assured by performing initial stage of experiments in dark to see the perfect mixing, adsorption of CO over catalyst surface and stable FT-IR spectra were obtained during the dark initial period of the experiments. The dark initial period data was fixed to 1h. After the steady conditions assessed by FT-IR spectrum, the second phase of the experiments were started by turning on the light source in irradiation chamber. The light kept open for 8,5h and started at t=61min.

As a summary.

- Dark: 1h
- Light: 8,5h

In Figure 4.28 the time course FT-IR spectra of gas phase during the experiment of the catalyst is presented. In Figure 4.29, the separated CO peaks are given.

The comparison of CO absorbance with calibration work allowed us to observe any adsorption of CO over the catalyst surface in the dark period. As it is seen from the spectra, a small decrease was observed on the CO peak intensities in the dark period. After light illuminated, the CO has not changed. Whereas, The CO_2 value has increased linearly, like a zero-order reaction with limitless reactant. That should be justified.

The change of CO absorbance with respect to wavelength for the catalyst was converted to the CO and CO_2 Concentration vs Absorbance data with the help of the 3rd order calibration equation calculated in the previous sections. The concentration data under room temperature for catalyst afterwards is calculated for the catalyst.

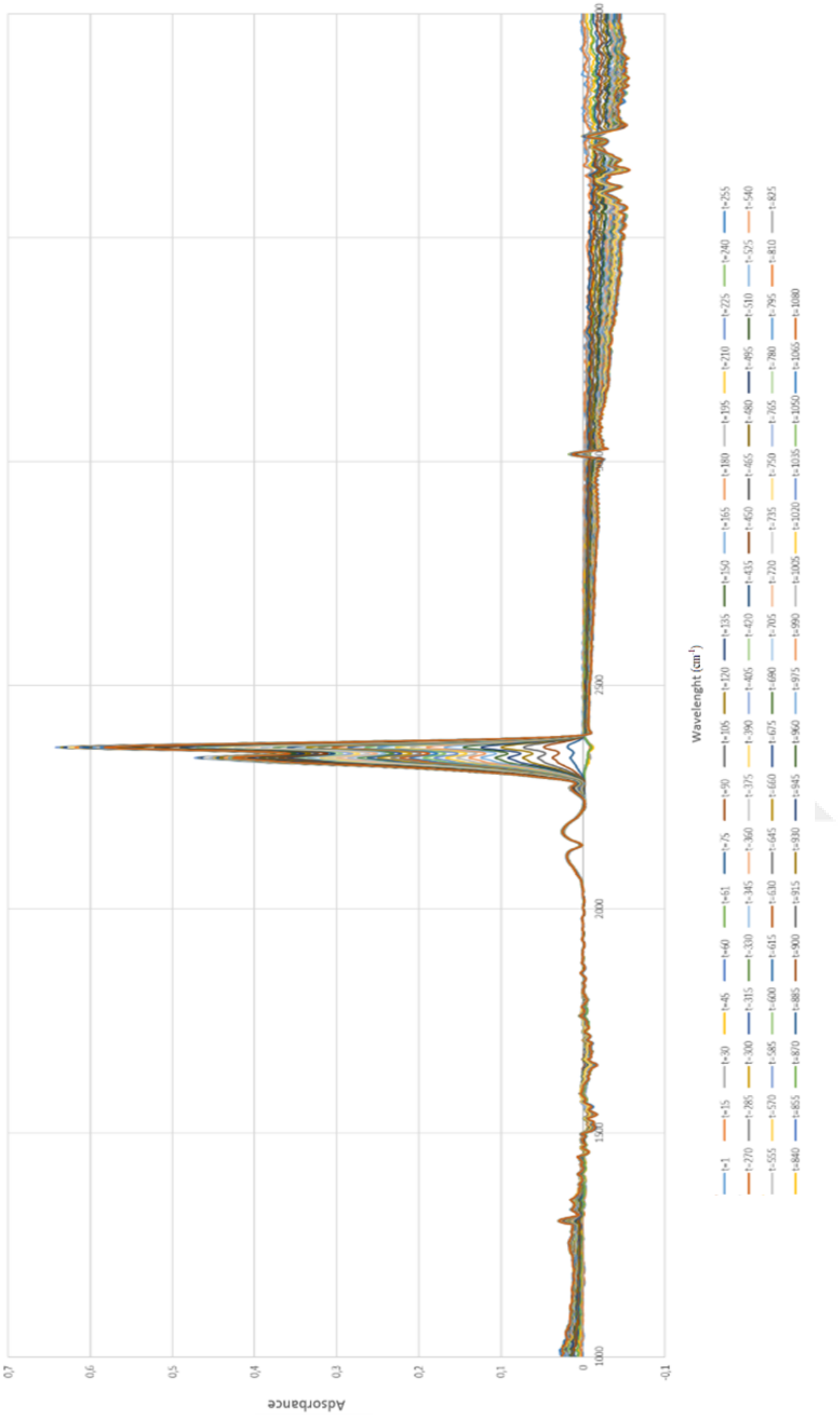

Figure 4.28 TiO_2/SiO_2 S_1 wo Calc with UVC Lamps

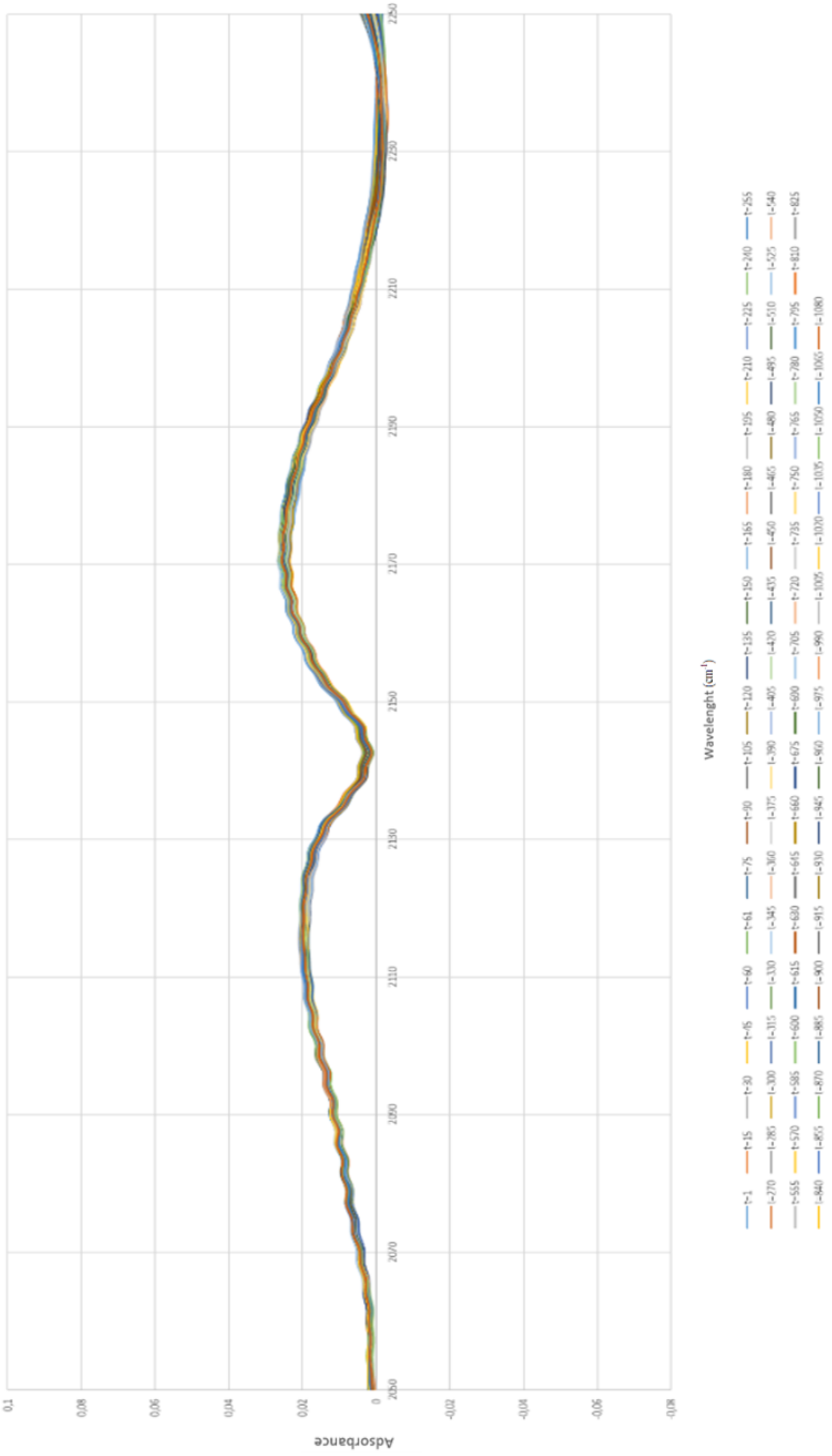

Figure 4.29 CO data extracted from Figure 4.28

The data was given in Table A.8 in appendices.

The CO and CO_2 concentration with time and percent conversion with respect to time graph can be found in Figure 4.30. The CO_2 conversion at the end was 90%.

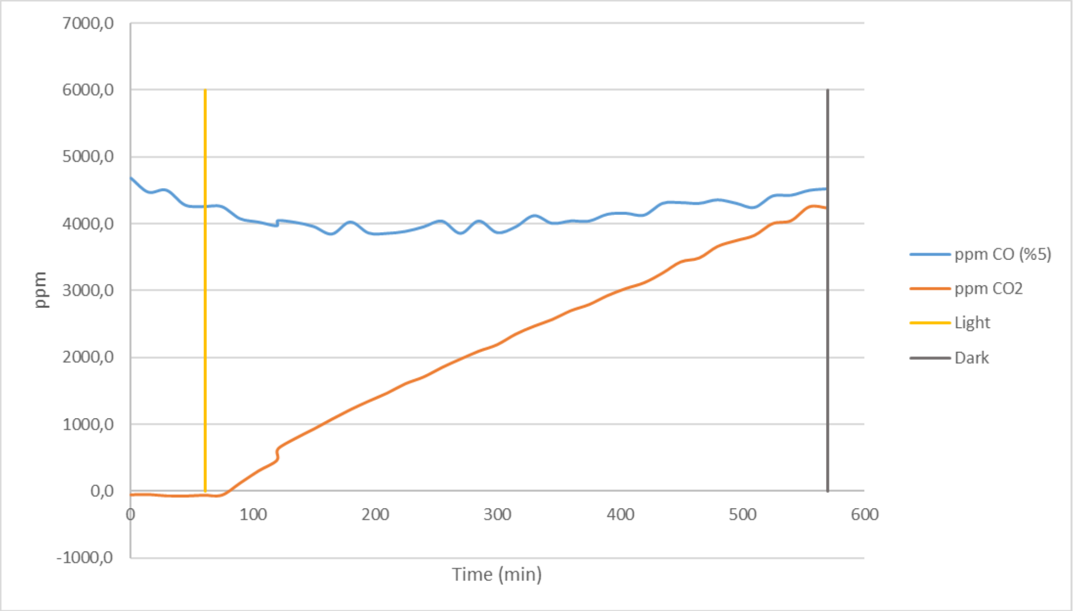

Figure 4.30 CO and CO_2 Concentration vs Time at Room Temperature for Sample TiO_2/SiO_2 S_1 wo Calc.

The impurities on 3000 indicates the additional HC's (hydrocarbons) in the catalyst which may lead the increase in carbon dioxide. Thus, the sample should be calcined accordingly. The unbalanced stoichiometry must be justified.

4.3.2.3 TiO_2/SiO_2 S_2 Sample (with Calcination) Photocatalytic Activity Test Results

The bare solution synthesis method was discussed in the Chapter 3. The sample was calcined prior to the experiment at 500°C for 30mins to see any impurities in the solution which may mislead the results and compare with the previous results.

The sample was placed in the reactor which was filled with fresh air prior to experiment. The proper volume of CO gas was injected into the reactor system and the gas was started to re-circulate by turning on the diaphragm pump.

During the re-circulation of CO gas, the IR bands for CO and CO_2 against a wavenumber range of 1900-2500 cm^{-1} was followed by FT-IR with the help of OPUS® software.

The mixing period of CO with air in the reaction system was performed and FT-IR spectrometer stability was assured by performing initial stage of experiments in dark to see the perfect mixing, adsorption of CO over catalyst surface and stable FT-IR spectra were obtained during the dark initial period of the experiments. The dark initial period data was fixed to 1h. After the steady conditions assessed by FT-IR spectrum, the second phase of the experiments were started by turning on the light source in irradiation chamber. The 2 light sources are 36 UVC lamps which were integrated to the reactor system. The light kept open for 8,5h and started at t=61min.

As a summary.

- Dark: 1h
- Light: 8,5h

In Figure 4.31 the time course FT-IR spectra of gas phase during the experiment of the catalyst is presented. In Figure 4.32, the separated CO peaks are given.

The comparison of CO absorbance with calibration work allowed us to observe any adsorption of CO over the catalyst surface in the dark period. As it is seen from the spectra, a small decrease was observed on the CO peak intensities in the dark period. After light illuminated, the CO has not changed. Whereas The CO_2 value has increased not linearly as the previous sample. The other impurities have been gone with the heat treatment. The catalyst activity must be worked more; the amount of the catalyst will be tried later on accordingly.

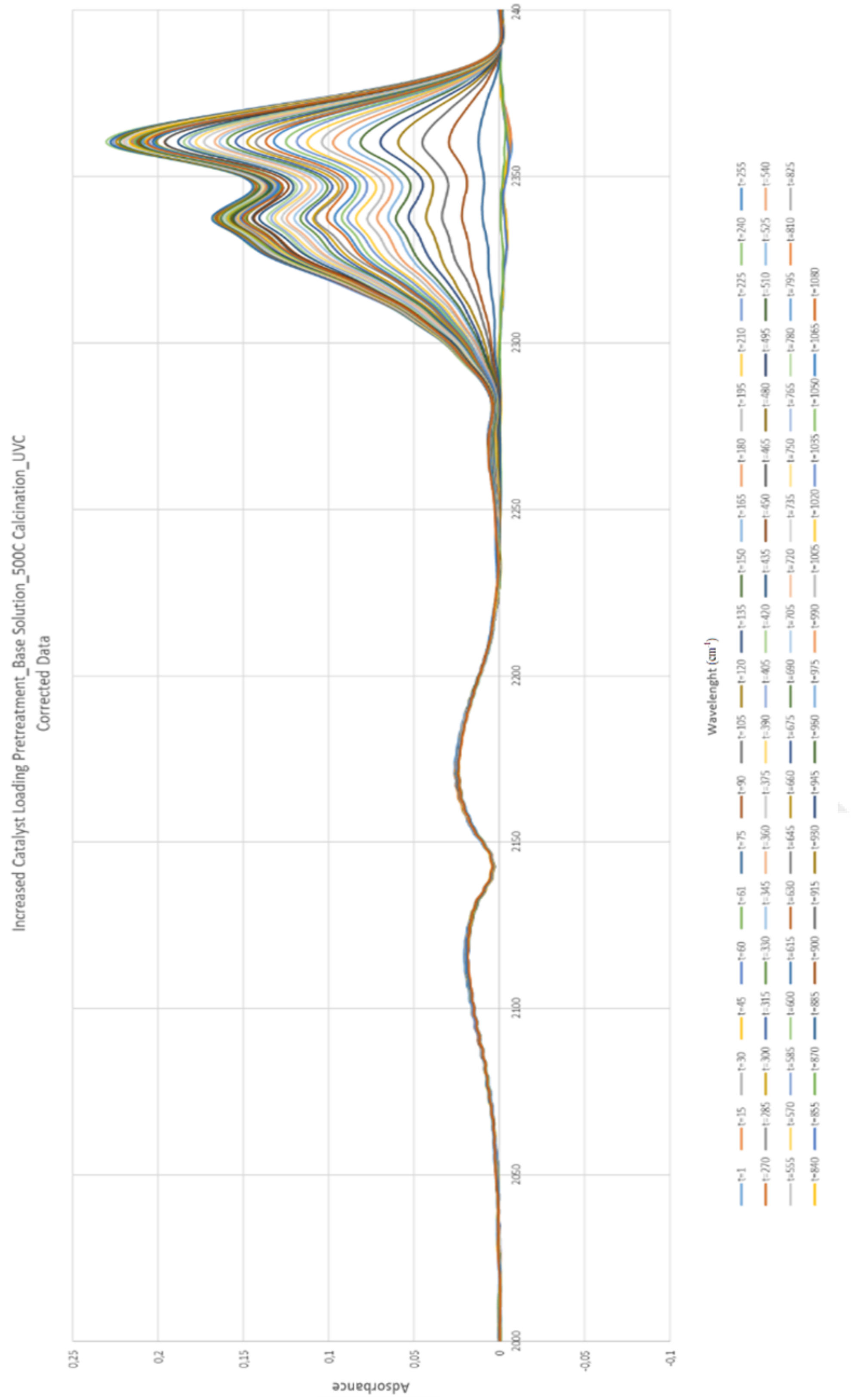

Figure 4.31 The Experiment Results Sample TiO_2/SiO_2 S_2 with Calcination

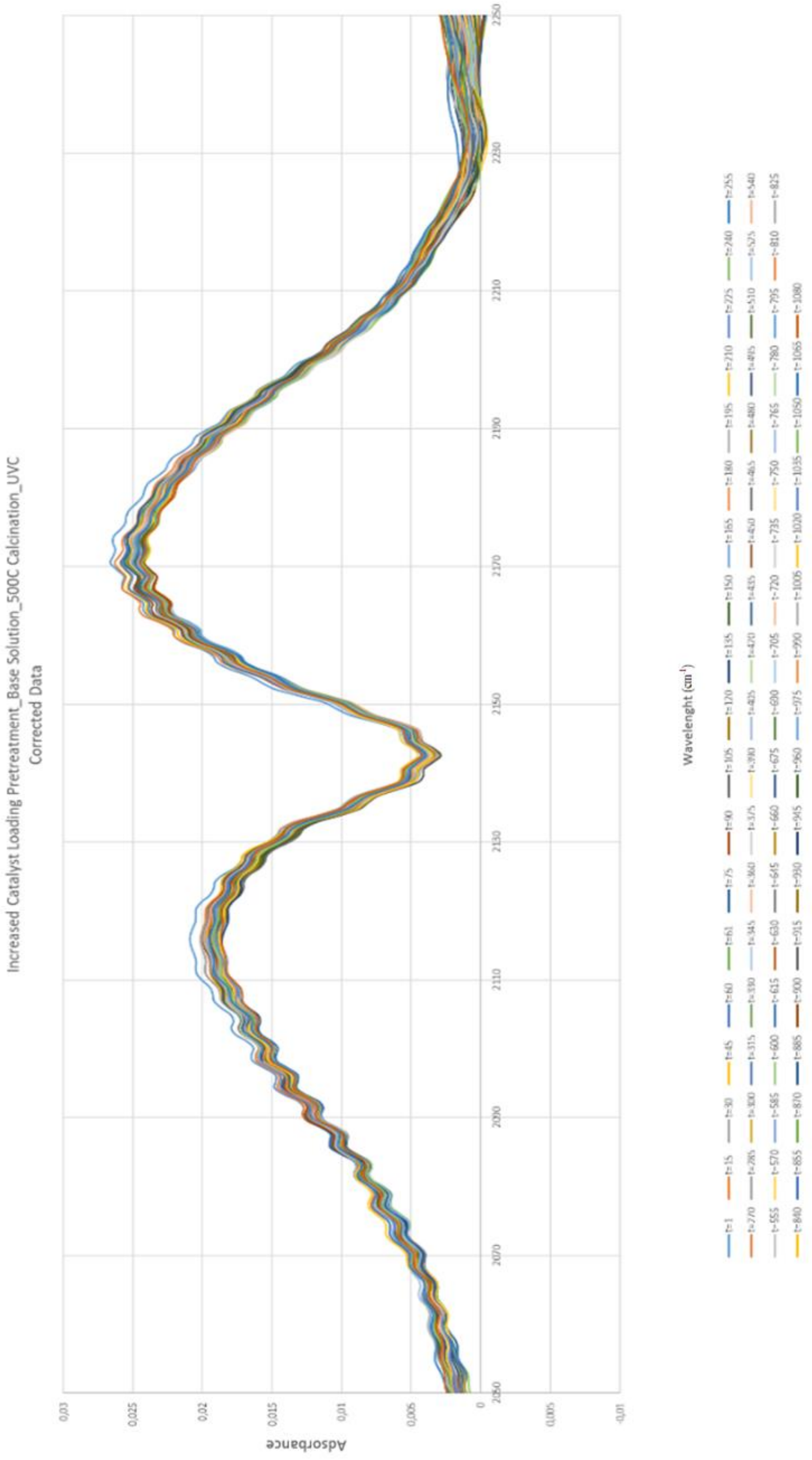

Figure 4.32 CO data extracted from Figure 4.31

The data was given in Table A.9 in appendices.

The CO and CO_2 concentration with time and percent conversion with respect to time graph can be found in Figure 4.33 The CO_2 conversion at the end was 30%.

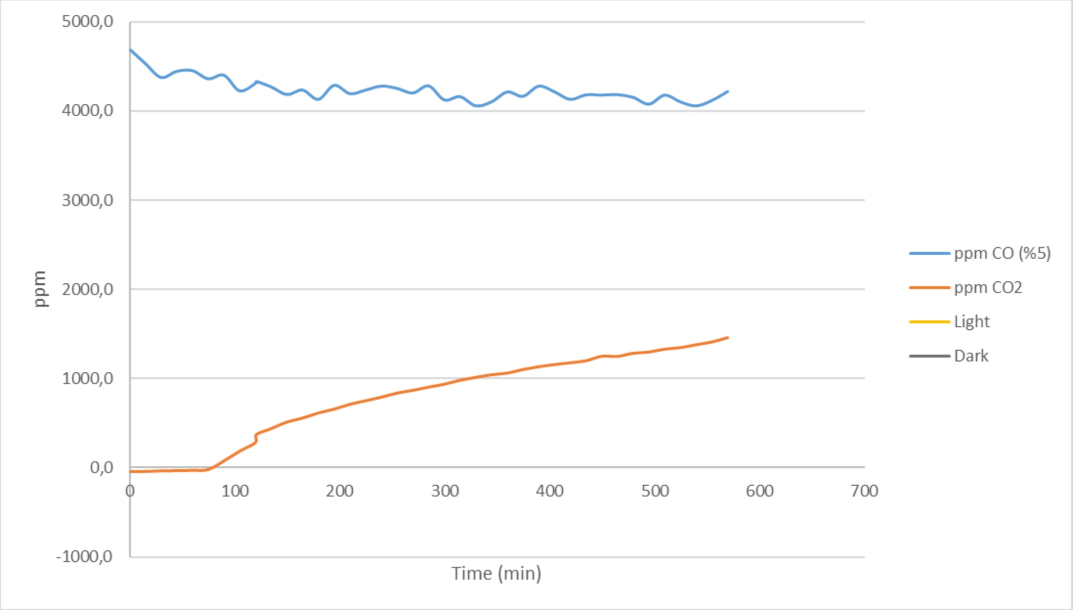

Figure 4.33 CO and CO_2 Concentration vs Time at Room Temperature for Sample TiO_2/ SiO_2 S_2 with Calcination

In conclusion, after the calcination the CO_2 conversion decreased from 90% to 30%. The decrease in CO is also less compared with the control experiments. Since the precision of CO is changing, it is a challenge to achieve the stoichiometric balance for CO and CO_2, which should be equal. The use of CO_2 values is more intensive and accurate. The most closed data for the stoichiometry is reached for the last calcined stainless steel catalyst substrate TiO_2/SiO_2 S_2.

CHAPTER 5

CONCLUSION

Under UV light and at room temperature, the photocatalytic degradation of carbon monoxide (CO) with a TiO_2-SiO_2 molar ratio of 0,5 catalyst over various support materials was investigated in this study. The coating solution is prepared using the sol-gel technique, and the catalysts were dip-coated on various support materials. Commercial PP filter paper, cellulosic filter paper and stainless-steel wire mesh was used and characterized as catalyst support materials. Thermal analysis, X-ray diffraction, and BET techniques were used to characterize the catalysts and support materials. For photocatalytic activity tests of synthesized catalysts, a re-circulated batch reactor system with FT-IR was constructed.

The effect of temperature on drying characteristics over cellulose catalyst supports held on by thermal analysis. For this purpose, to attain a specific calcination and drying temperature, TGA - DTA Analysis was held on with N_2. As a demonstration, reference commercial filter paper and cellulose filter paper has been utilized. The test held on up to 500 and 900°C degrees with 10°C/min intervals for commercial PP filter paper and cellulosic filter paper, respectly. As a result, it may be deduced that the commercial PP filter paper burns at about 250°C. For the TGA of the cellulosic filter paper at the beginning of the scan, there is a slight weight drop that can be attributed to water intake before. The significant weight loss objected at 357℃, indicates the decomposition of the cellulose filter paper substance. Hence, it may be determined that both types of filter papers ignite between 250°C and 357°C. As a result, the filter paper sample is ineligible for sample calcination after dip coating. The maximum acceptable drying temperature for commercial filter paper and cellulosic substrate are kept as 100°C for water evaporation.

The physical adsorption of gas molecules on a solid surface rule was utilized by BET (Brunaur-Emmett-Teller) for the assessment of the catalyst samples' specific surface area, pore size distribution, and pore volume. The nitrogen adsorption isotherms obtained at 77K were used for the assessment of the specific surface area values of photo catalysts and bare support materials using the BET technique. As a result the commercial filter paper the catalyst is not reached inside the pores. The specific surface area of the coated and bare supoort materials almost the same around 2-4 m^2/gr. The commercial filter paper is hydrophobic and can not be used for coating purposes. As a reccommendation the commercial filter paper could be worked for a pretreatment that allows hydrofhilic properties for further studies.

The alternative type of cellulose filter paper that is suspected to be used as a support material for catalys coating and is distinguished by its specific surface area. Therefore, it can be concluded that cellulose support can be coated and the surface area can be increased from 0,4 m^2/gr to 54 m^2/gr.

To investigate the crystalline phase, crystallite size, and crystal structure of TiO_2, X-ray diffraction analyses were performed on coated filter samples. The XRD patterns of coated samples indicated that titania crystallized as anatase, which has greater photocatalytic activity than rutile and brookite for the majority of photocatalytic reactions. Observed at 2θ 25,4° is a prominent peak attributable to the anatase phase. Samples exhibited only a broad peak at the start, indicating the presence of an amorphous structure. Overtones in the background indicated that all samples contained silica. It can be concluded that titania is depicted as anatase and amorphous silicate is depicted initially.

In the photocatalytic activity tests with the cellulosic filter paper support material, an unexpected CO_2 and CO increase observed under 36-Watts UVC radiation. To justify this result, a bunch of control experiments held on and as a result the connections and the reactor itself contributes no further oxidation as CO concentrations have not decreased significantly. The increase in both, also worked without any CO content in the glass cylinder for any difference will be detected with comparison to the CO reactant itself. Under UVC irradiation, it can be concluded that there is an additional increase in CO_2 and CO from the catalyst support material itself, which is cellulose. The increase in CO peak intensities demonstrates that the bare cellulose support decomposed to CO and CO_2 following illumination. With the catalyst involve the final CO_2 level is much higher than the bare one. This is why the catalyst influences cellulose degradation. Some HC peaks also detected around 3000cm^{-1}. A summary comparison graph is given below for the cellulose support.

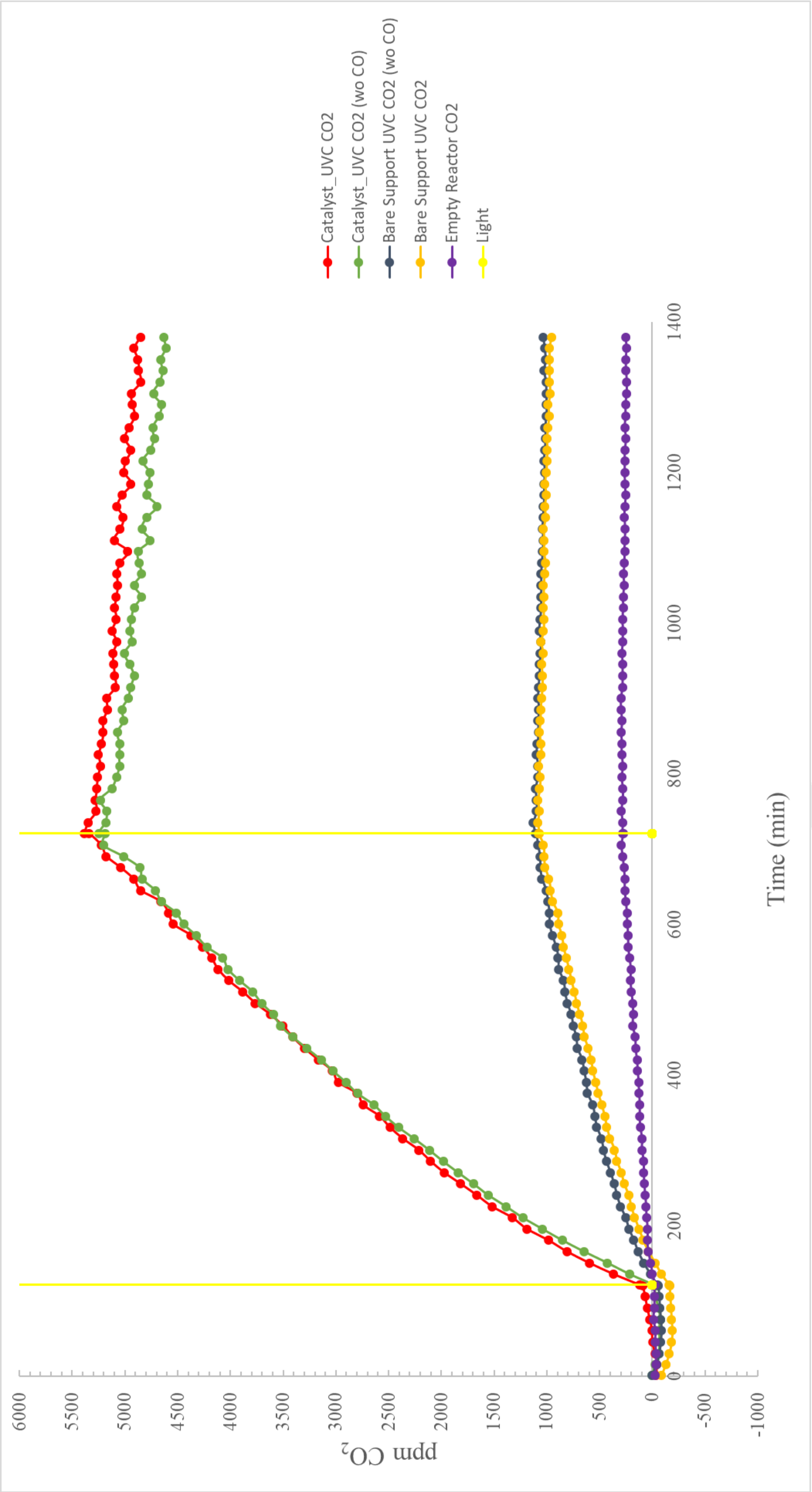

Figure 5.1 A Summary Comparison of the Experiments with Cellulosic Support

In conclusion with the experiments with cellulosic filter paper support material for catalyst coating, a new catalyst support introduced to eliminate the CO and CO_2 emissions which originated by cellulose itself. The viability of cellulose under UV illumination was examined via control experiments. The study utilizes a 304 stainless-steel wire mesh support material for this purpose. After conducting control experiments using stainless steel wire mesh support material, it has been established that the 304 stainless-steel wire mesh catalyst support material may be used to showcase the performance of the catalyst. To remove the hydrocarbons, a calcination period is included in the synthesis process, as the substance is non-flammable. The ultimate CO_2 conversion reached 30% following the calcination of the TiO_2-SiO_2 catalyst on a stainless-steel wire mesh support material. The CO values are challenging to evaluate any stochiometric balance in between the CO and CO_2 values. Precision of CO, also in control experiments are defined and CO_2 values are used for qualitative analysis. All conversion and volume data can be found in Appendices. Given that the catalyst loading is 0,026 gr/m^2, for stainless steel wire mesh substrate catalyst, which can be insufficient to detect any significant catalytic oxidation (30%), it is necessary to consider enhancement of the catalyst loading for future investigations. Metal doping can also increase the catalytic activity. An alternative methodology is presented in the Appendices B.

REFERENCES

Adjimi, S., Sergent, N., Roux, L.-C., Delpech, F., Pera-Titus, M., Chhor, K., . . . Thivel, P.-X. (2014). Photocatalytic paper based on sol–gel titania nanoparticles immobilized on porous silica for VOC abatement. Applied Catalysis B: Environmental(154-155), 123-133.

Bayram, B. (2009). Photocatalytic Activity of Titania-Silica Mixed Oxides Prepared With Co-Hydrolization. MSc Thesis, METU, Ankara, .

Brinker, C., & Scherer, G. (1990). Sol-gel Science: The Physics and Chemistry of Sol-gel Processing. Academic Press, 908.

Carp, O., Huisman, C., & Reller, A. (2004). Photoinduced reactivity of titanium dioxide. Progress in Solid State Chemistry, 32(1-2), 33-177.

Delimaris, D., & Ioannides, T. (2009). VOC oxidation over $CuO–CeO_2$ catalysts prepared by a combustion method. Applied Catalysis B: Environmental, 89(1-2), s. 295-302.

Gaoa, Z., Zhaib, X., Liua, F., Zhanga, M., Zanga, D., & Wanga, C. (2015). Fabrication of TiO_2/EP super-hydrophobic thin fillm on filter paper surface. Carbohydrate Polymers(128), 24-31.

Grela, M., Coronel, M., & Colussi, A. (1996). Quantitative Spin-Trapping Studies of Weakly Illuminated Titanium Dioxide Sols. Implications for the Mechanism of Photocatalysis,. (95), 3654, 16940-16946.

Huang, X., Wen, X., Cheng, J., & Yang, Z. (2012). Sticky superhydrophobic filter paper developed by dip-coating of fluorinated waterborne epoxy emulsion. Applied Surface Science(258), s. 8739-8746.

Hwang, S., Lee, M., & Choi, W. (2013). Highly enhanced photocatalytic oxidation of CO on titania deposited with Pt nanoparticles: kinetics and mechanism. Applied Catalysis B: Environmental, 1(46), 49-60.

Ivanova, I., Schneider, J., Gutzmann, H., Kliemann, J., Gärtner, F., Klassen, T., . . . Mendive, C. (2013). Photocatalytic degradation of oxalic and dichloroacetic acid on TiO_2. Catalysis Today(209), pp. 84-90.

Jinze, L., Zhu, L., & Burda, C. (2014). Considerations to iprove the adsorption and photocatalysis of low concentration air pollutants on TiO_2. Catalysis Today(225).

Kamagewa, T., Takeuchi, R., Matsuoka, M., & Anpo, M. (2006). Photocatalytic oxidation of CO with various oxidants by Mo oxide species highly dispersed on SiO_2 at 293 K. Catalysis Today, 111(3-4), 248-253.

Kirbas, T. (2014). Syntheis of CNT-Titania-Silica Nanocomposite Thin Films: The Effect of the Heat Treatment on the Catalytic Activity. MSC Thesis, METU, Ankara.

Li, R., Liu, J., Cai, N., Zhang, M., & Wang, P. (2010). Synchronously Reduced Surface States, Charge Recombination and Light Absorption Length for High-Performance Organic Dye-Sensitized Solar Cells. Journal of Physical Chemistry, 114(13), 4461-4464.

Mirkelamoglu, B., & Karakas, G. (2006). The role of alkali-metal promotion on CO oxidation over PdO/SnO_2 catalysts. Applied Catalysis A: General(299), s. 84-94.

Moretti, E., Storaro, L., Talon, A., Patrono, P., Pinzari, F., Montanari, T., . . . Lenarda, M. (2008). Preferential CO Oxidation (CO PROX) over CuO-ZnO/TiO_2 Catalysts. Journal of Applied Catatysis A: General(344), 165-174.

Shang, J., Li, W., & Zhu, Y. (2003). Structure and photocatalytic characteristics of TiO_2 film. Journal of Molecular Catalysis A: Chemical(202), s. 187-195.

Tartakovsky, L., Bibikov, V., Czerwinsky, J., Gutman, M., Kasper, M., Poposcu, D., . . . Zvirin, Y. (2013). In Vehicle Particle Air Pollution and its Mitigation. Atmospheric Environment 64, pp. 320-328.

Wang, J., Wenxia, L., Haidong, L., Huili, W., Wang, Z., Zhou, W., & Hong, L. (2012). Preparation of cellulose fiber–TiO_2 nanobelt–silver nanoparticle hierarchically structured hybrid paper and its photo catalytic and antibacterial properties. School of Chemistry and Chemical Engineering, South China University of Technology, Guangzhou 510640, China Applied Surface Science(258), 8739-8746.

Wang, S., Ang, H., & Tade, M. (2007). Volatile Organic Compounds in Indoor Environment and Photo catalytic Oxidation: State of Art. Environment International (33), 694-705.

Watson, A. (2004). Indoor Air Quality in Industrial Nations, Encyclopedia of Energy.

World Health Organization. (1983). Indoor Air Pollutants: Exposure and Health Effects. Vol-8, s. 1-42.

World Health Organization. (2002). Reducing Risks, Promoting Healthy Life.

World Health Organization. (2010). Guidelines for indoor air pollution: Selected Pollutants.

Yetisemeyen, P. (2010). Low Temperature Photo catalytic Oxidation of CO over Pd Doped Titania Catalysts. MSc Thesis, METU, Ankara.

Zhang, M., Jin, S., Zhang, J., Zhanh, Z., & Dang, H. (2005). Effect of Calcination and Reduction Treatment on The Photo catalytic Activity of CO Oxidaiton on Pt/TiO_2. Journal of Molecular Catalysis A: Chemical, 1(225), 59-63.

Zhao, J., & Yahn, X. (2003). Photo catalytic Oxidaiton for Indoor Air Purification: A Literature Review. Building and Environment(38), 645-654.

Zhong , L., Haghighat, F., Blondeau, P., & Kozinski, J. (2010). Modeling and Physical Interpretation of Photo catalytic Oxidation Efficiency in Indoor Air Applications, Building and Environment. 45(12), s. 2689-2697.

APPENDICES

A. Absorbance vs Conversion Data for Photocatalytic Activity Tests

Table A.1 Absorbance vs Conversion Data of wo Reactor & Catalyst Experiment

Time (min)	Absorbance CO (cm^{-1})	ppm CO	CO Conv (%)	Absorbance CO_2 (cm^{-1})	ppm CO_2	CO_2 Conv (%)
t=1	0,036069096	7610,34	0,0	-0,008998904	-56,8864	-0,7
t=15	0,036656986	7800,99	-2,5	-0,008539014	-53,9815	-0,7
t=30	0,036900192	7880,19	-3,5	-0,005807808	-36,7246	-0,5
t=45	0,036804575	7849,03	-3,1	-0,005201425	-32,8921	-0,4
t=60	0,036234411	7663,84	-0,7	-0,003723589	-23,5499	-0,3
t=75	0,036559603	7769,33	-2,1	-0,004674397	-29,5608	-0,4
t=90	0,036250521	7669,06	-0,8	-0,004391479	-27,7723	-0,4
t=105	0,036428658	7726,81	-1,5	-0,003967342	-25,091	-0,3
t=120	0,037068562	7935,13	-4,3	-0,003727438	-23,5743	-0,3
t=135	0,036399315	7717,29	-1,4	-0,005616685	-35,5167	-0,5
t=150	0,036536836	7761,94	-2,0	-0,005015164	-31,7148	-0,4
t=165	0,036208603	7655,48	-0,6	-0,003889397	-24,5982	-0,3
t=180	0,036510479	7753,38	-1,9	-0,005003521	-31,6412	-0,4
t=195	0,036389342	7714,06	-1,4	-0,003872658	-24,4924	-0,3
t=210	0,036266356	7674,19	-0,8	-0,004839644	-30,6053	-0,4
t=225	0,036370384	7707,91	-1,3	-0,002259616	-14,2929	-0,2
t=240	0,036445795	7732,37	-1,6	-0,004436205	-28,0551	-0,4
t=255	0,036037863	7600,24	0,1	-0,005388137	-34,0722	-0,4
t=270	0,035912808	7559,85	0,7	-0,005593192	-35,3682	-0,5
t=285	0,03560911	7461,97	1,9	-0,00519489	-32,8508	-0,4
t=300	0,036401644	7718,05	-1,4	-0,006104356	-38,5988	-0,5
t=315	0,036262315	7672,88	-0,8	-0,006839685	-43,2454	-0,6
t=330	0,036052192	7604,88	0,1	-0,006419808	-40,5922	-0,5

Table A.1 (continued) Absorbance vs Conversion Data of wo Reactor & Catalyst Experiment

t=345	0,036190849	7649,73	-0,5	-0,007989151	-50,5079	-0,7
t=360	0,036145712	7635,12	-0,3	-0,005358288	-33,8836	-0,4
t=375	0,035840945	7536,66	1,0	-0,006139055	-38,818	-0,5
t=390	0,036454863	7735,32	-1,6	-0,007545137	-47,7027	-0,6
t=405	0,036324507	7693,03	-1,1	-0,007381493	-46,6688	-0,6
t=420	0,035551411	7443,41	2,2	-0,006118589	-38,6887	-0,5
t=435	0,035944192	7569,98	0,5	-0,006895808	-43,6001	-0,6
t=450	0,035732904	7501,83	1,4	-0,005549096	-35,0895	-0,5
t=465	0,035596808	7458,01	2,0	-0,005565192	-35,1913	-0,5
t=480	0,036389192	7714,01	-1,4	-0,006716808	-42,469	-0,6
t=495	0,03597926	7581,31	0,4	-0,00576874	-36,4777	-0,5
t=510	0,035594932	7457,41	2,0	-0,006945068	-43,9113	-0,6
t=525	0,036415274	7722,47	-1,5	-0,006468726	-40,9014	-0,5
t=540	0,035887068	7551,54	0,8	-0,007802932	-49,3314	-0,6
t=555	0,03635963	7704,42	-1,2	-0,00641237	-40,5452	-0,5
t=570	0,035946274	7570,65	0,5	-0,005749726	-36,3576	-0,5
t=571	0,036304671	7686,6	-1,0	-0,005085329	-32,1583	-0,4
t=585	0,035843863	7537,6	1,0	-0,002796137	-17,6858	-0,2
t=600	0,036078973	7613,53	0,0	-0,000115027	-0,72774	0,0
t=615	0,036189767	7649,38	-0,5	0,000951767	6,022075	0,1
t=630	0,03661911	7788,68	-2,3	0,00390111	24,69008	0,3
t=645	0,036084466	7615,31	-0,1	0,003238466	20,49495	0,3
t=660	0,036437671	7729,74	-1,6	0,005949671	37,6626	0,5
t=675	0,036268041	7674,73	-0,8	0,007656041	48,47199	0,6
t=690	0,035892137	7553,18	0,8	0,007338137	46,45789	0,6
t=705	0,035965329	7576,81	0,4	0,008711329	55,15869	0,7
t=720	0,036339479	7697,89	-1,2	0,009647479	61,0916	0,8
t=735	0,03643389	7728,51	-1,6	0,01063389	67,34419	0,9
t=750	0,036366781	7706,74	-1,3	0,011666781	73,89265	1,0

Table A.1 (continued) Absorbance vs Conversion Data of wo Reactor & Catalyst Experiment

t=765	0,036026178	7596,47	0,2	0,012836178	81,3081	1,1
t=780	0,036210616	7656,13	-0,6	0,013440616	85,14165	1,1
t=795	0,036335466	7696,58	-1,1	0,014393466	91,18584	1,2
t=810	0,036339658	7697,94	-1,2	0,016157658	102,3795	1,3
t=825	0,036363658	7705,73	-1,3	0,017607658	111,5825	1,5
t=840	0,036228356	7661,88	-0,7	0,022058356	139,8467	1,8
t=855	0,035667575	7480,79	1,7	0,020233575	128,2555	1,7
t=870	0,036191521	7649,95	-0,5	0,020571521	130,4018	1,7
t=885	0,035693041	7488,99	1,6	0,022455041	142,3671	1,9
t=900	0,036516151	7755,22	-1,9	0,025574151	162,1911	2,1
t=915	0,036480397	7743,61	-1,8	0,026208397	166,2237	2,2
t=930	0,036725219	7823,19	-2,8	0,026391219	167,3862	2,2
t=945	0,036131	7630,36	-0,3	0,028899	183,3362	2,4
t=960	0,036370959	7708,09	-1,3	0,029522959	187,306	2,5
t=975	0,036130904	7630,33	-0,3	0,030416904	192,9943	2,5
t=990	0,036046096	7602,91	0,1	0,033096096	210,0484	2,8
t=1005	0,036478671	7743,05	-1,7	0,033270671	211,16	2,8
t=1020	0,037264123	7999,05	-5,1	0,034730123	220,4542	2,9
t=1035	0,036711712	7818,8	-2,7	0,036089712	229,1148	3,0
t=1050	0,036277178	7677,69	-0,9	0,037537178	238,3379	3,1
t=1065	0,036389014	7713,95	-1,4	0,040677014	258,3538	3,4
t=1080	0,036385384	7712,77	-1,3	0,041111384	261,1238	3,4
t=1095	0,036354548	7702,77	-1,2	0,042310548	268,7723	3,5
t=1110	0,036175849	7644,88	-0,5	0,043873849	278,7462	3,7
t=1125	0,036338137	7697,45	-1,1	0,043074137	273,6436	3,6
t=1140	0,036510301	7753,32	-1,9	0,044934301	285,5136	3,8
t=1155	0,036445712	7732,35	-1,6	0,045641712	290,029	3,8
t=1170	0,03597074	7578,56	0,4	0,04806874	305,5253	4,0
t=1185	0,036569452	7772,53	-2,1	0,049339452	313,6418	4,1

Table A.1 (continued) Absorbance vs Conversion Data of wo Reactor & Catalyst Experiment

t=1200	0,036469795	7740,16	-1,7	0,051067795	324,6848	4,3
t=1215	0,036485233	7745,18	-1,8	0,051335233	326,3939	4,3
t=1230	0,036140986	7633,59	-0,3	0,050758986	322,7114	4,2
t=1245	0,035932644	7566,25	0,6	0,054488644	346,5534	4,6
t=1260	0,036665027	7803,61	-2,5	0,053945027	343,0772	4,5
t=1275	0,036116932	7625,81	-0,2	0,060198932	383,0929	5,0
t=1290	0,03618437	7647,63	-0,5	0,06084037	387,2002	5,1
t=1305	0,03666589	7803,89	-2,5	0,06086589	387,3636	5,1
t=1320	0,036498726	7749,56	-1,8	0,061240726	389,764	5,1
t=1335	0,036820479	7854,21	-3,2	0,062254479	396,2569	5,2
t=1350	0,036408301	7720,21	-1,4	0,063860301	406,5449	5,3
t=1365	0,036763589	7835,68	-3,0	0,066123589	421,0509	5,5
t=1380	0,036460342	7737,1	-1,7	0,065762342	418,7351	5,5
t=1395	0,03651574	7755,08	-1,9	0,06644174	423,0906	5,6
t=1410	0,035907288	7558,07	0,7	0,071199288	453,6082	6,0
t=1425	0,036777877	7840,34	-3,0	0,072443877	461,5968	6,1
t=1440	0,036312137	7689,02	-1,0	0,075504137	481,249	6,3
t=1455	0,03616526	7641,45	-0,4	0,07504926	478,3271	6,3
t=1470	0,036006466	7590,1	0,3	0,077928466	496,8267	6,5
t=1485	0,036039808	7600,87	0,1	0,079759808	508,5996	6,7
t=1500	0,036190205	7649,52	-0,5	0,080152205	511,1228	6,7
t=1515	0,035852945	7540,53	0,9	0,085038945	542,5637	7,1
t=1530	0,035558041	7445,54	2,2	0,086522041	552,1125	7,3
t=1545	0,034656055	7156,91	6,0	0,091470055	583,9931	7,7
t=1560	0,034448479	7090,91	6,8	0,099054479	632,9296	8,3
t=1575	0,034198808	7011,73	7,9	0,100276808	640,8243	8,4
t=1590	0,03410089	6980,74	8,3	0,10765289	688,5114	9,0
t=1605	0,032918534	6609,52	13,2	0,115804534	741,3079	9,7

Table A.2 Absorbance vs Conversion Data of the Empty Reactor on UVC

Time (min)	Absorbance CO (cm^{-1})	ppm CO (%5)	CO Conv (%)	Absorbance CO_2 (cm^{-1})	ppm CO_2	CO_2 Conv (%)
t=1	0,027462849	4977,0	0,0	-0,009537151	-60,3	-1,2
t=15	0,026874137	4809,8	3,4	-0,010907863	-68,9	-1,4
t=30	0,026322849	4654,9	6,5	-0,012697151	-80,2	-1,6
t=45	0,025913233	4541,0	8,8	-0,010774767	-68,1	-1,4
t=60	0,026016836	4569,7	8,2	-0,010151164	-64,2	-1,3
t=75	0,025712932	4485,6	9,9	-0,007493068	-47,4	-1,0
t=90	0,025685137	4477,9	10,0	-0,006094863	-38,5	-0,8
t=105	0,025608973	4457,0	10,4	-0,005047027	-31,9	-0,6
t=120	0,025103082	4318,5	13,2	-0,001926918	-12,2	-0,2
t=135	0,024963384	4280,5	14,0	0,001853384	11,7	0,2
t=150	0,025367151	4390,6	11,8	0,001057151	6,7	0,1
t=165	0,024782151	4231,4	15,0	0,001544151	9,8	0,2
t=180	0,024436781	4138,4	16,8	0,004456781	28,2	0,6
t=195	0,025006863	4292,3	13,8	0,006794863	43,0	0,9
t=210	0,024790562	4233,7	14,9	0,006322562	40,0	0,8
t=225	0,024716959	4213,8	15,3	0,006980959	44,2	0,9
t=240	0,024810726	4239,1	14,8	0,006606726	41,8	0,8
t=255	0,024699603	4209,1	15,4	0,006983603	44,2	0,9
t=270	0,025083466	4313,1	13,3	0,007709466	48,8	1,0
t=285	0,024794479	4234,8	14,9	0,006160479	39,0	0,8
t=300	0,024634986	4191,7	15,8	0,008898986	56,3	1,1
t=315	0,024280466	4096,6	17,7	0,008342466	52,8	1,1
t=330	0,024904726	4264,6	14,3	0,008306726	52,6	1,1
t=345	0,025106219	4319,3	13,2	0,008996219	57,0	1,1
t=360	0,02484226	4247,7	14,7	0,00854626	54,1	1,1

Table A.2 (continued) Absorbance vs Conversion Data of the Empty Reactor on UVC

t=375	0,024475534	4148,8	16,6	0,008643534	54,7	1,1
t=390	0,024799233	4236,0	14,9	0,007397233	46,8	0,9
t=405	0,025313123	4375,8	12,1	0,010001123	63,3	1,3
t=420	0,024515959	4159,7	16,4	0,008971959	56,8	1,1
t=435	0,024725986	4216,2	15,3	0,008999986	57,0	1,1
t=450	0,024523644	4161,7	16,4	0,008417644	53,3	1,1
t=465	0,025226548	4352,1	12,6	0,007318548	46,3	0,9
t=480	0,024659603	4198,3	15,6	0,006029603	38,2	0,8
t=495	0,025224808	4351,7	12,6	0,006884808	43,6	0,9
t=510	0,024605849	4183,9	15,9	0,007513849	47,6	1,0
t=525	0,024988452	4287,3	13,9	0,006520452	41,3	0,8
t=540	0,024797644	4235,6	14,9	0,007217644	45,7	0,9
t=555	0,024904055	4264,4	14,3	0,006316055	40,0	0,8
t=570	0,024667849	4200,6	15,6	0,005911849	37,4	0,8
t=585	0,025192466	4342,8	12,7	0,006602466	41,8	0,8
t=600	0,024939685	4274,1	14,1	0,006881685	43,6	0,9
t=615	0,025485247	4423,0	11,1	0,005095247	32,3	0,6
t=630	0,024985795	4286,6	13,9	0,005429795	34,4	0,7
t=645	0,024393425	4126,8	17,1	0,004005425	25,4	0,5
t=660	0,02466526	4199,9	15,6	0,00580326	36,7	0,7
t=675	0,024873575	4256,2	14,5	0,004697575	29,7	0,6
t=690	0,025249411	4358,4	12,4	0,004687411	29,7	0,6
t=705	0,024897041	4262,5	14,4	0,004917041	31,1	0,6
t=720	0,02466289	4199,2	15,6	0,00425089	26,9	0,5
t=735	0,024498247	4154,9	16,5	0,010990247	69,6	1,4
t=750	0,02419337	4073,3	18,2	0,01427137	90,4	1,8
t=765	0,02460189	4182,8	16,0	0,01700389	107,8	2,2

Table A.2 (continued) Absorbance vs Conversion Data of the Empty Reactor on UVC

t=780	0,024027479	4029,2	19,0	0,017515479	111,0	2,2
t=795	0,023958397	4010,8	19,4	0,021368397	135,5	2,7
t=810	0,024009397	4024,4	19,1	0,023887397	151,5	3,0
t=825	0,024106603	4050,2	18,6	0,024474603	155,2	3,1
t=840	0,023649068	3929,1	21,1	0,024213068	153,5	3,1
t=855	0,023970671	4014,1	19,3	0,026274671	166,6	3,3
t=870	0,023794808	3967,5	20,3	0,027270808	173,0	3,5
t=885	0,023966137	4012,9	19,4	0,026950137	170,9	3,4
t=900	0,023612616	3919,5	21,2	0,027746616	176,0	3,5
t=915	0,023990685	4019,4	19,2	0,028054685	178,0	3,6
t=930	0,024025288	4028,6	19,1	0,027923288	177,1	3,6
t=945	0,024034027	4030,9	19,0	0,029696027	188,4	3,8
t=960	0,024052575	4035,8	18,9	0,028068575	178,1	3,6
t=975	0,024131521	4056,8	18,5	0,028955521	183,7	3,7
t=990	0,023947082	4007,8	19,5	0,028785082	182,6	3,7
t=1005	0,023854712	3983,4	20,0	0,029150712	184,9	3,7
t=1020	0,023805205	3970,3	20,2	0,029185205	185,2	3,7
t=1035	0,024131041	4056,7	18,5	0,029041041	184,2	3,7
t=1050	0,02386963	3987,3	19,9	0,03128163	198,5	4,0
t=1065	0,023846822	3981,3	20,0	0,030874822	195,9	3,9
t=1080	0,024080534	4043,3	18,8	0,031912534	202,5	4,1
t=1095	0,02420189	4075,6	18,1	0,03106589	197,1	4,0
t=1110	0,02397626	4015,6	19,3	0,03385826	214,9	4,3
t=1125	0,023972438	4014,6	19,3	0,032746438	207,8	4,2
t=1140	0,02410537	4049,9	18,6	0,03407537	216,3	4,3
t=1155	0,02379274	3967,0	20,3	0,03183074	202,0	4,1
t=1170	0,023557644	3905,0	21,5	0,032625644	207,1	4,2

Table A.2 (continued) Absorbance vs Conversion Data of the Empty Reactor on UVC

t=1185	0,024087548	4045,1	18,7	0,034643548	219,9	4,4
t=1200	0,024026918	4029,0	19,0	0,033524918	212,8	4,3
t=1215	0,023969603	4013,8	19,4	0,033089603	210,0	4,2
t=1230	0,023995068	4020,6	19,2	0,034325068	217,9	4,4
t=1245	0,024368178	4120,0	17,2	0,035444178	225,0	4,5
t=1260	0,023973192	4014,8	19,3	0,034499192	219,0	4,4
t=1275	0,024175137	4068,5	18,3	0,035549137	225,7	4,5
t=1290	0,024001603	4022,3	19,2	0,035035603	222,4	4,5
t=1305	0,024284356	4097,6	17,7	0,034372356	218,2	4,4
t=1320	0,024426425	4135,7	16,9	0,035346425	224,4	4,5
t=1335	0,024403795	4129,6	17,0	0,034785795	220,8	4,4
t=1350	0,024542493	4166,8	16,3	0,036410493	231,2	4,6
t=1365	0,024123507	4054,7	18,5	0,036969507	234,7	4,7
t=1380	0,02431137	4104,8	17,5	0,03645537	231,4	4,7
t=1395	0,024555247	4170,2	16,2	0,035927247	228,1	4,6
t=1410	0,024313425	4105,4	17,5	0,034853425	221,2	4,4
t=1425	0,024075767	4042,0	18,8	0,037607767	238,8	4,8
t=1440	0,024424904	4135,2	16,9	0,037092904	235,5	4,7

Table A.3 Absorbance vs Conversion Data of the Bare Cellulose Support Material

Time (min)	Absorbance CO (cm^{-1})	ppm CO (%5)	CO Conv (%)	Absorbance CO_2 (cm^{-1})	ppm CO_2	CO_2 Conv (%)
t=1	0,02850974	5279,0	0,0	-0,01373226	-86,8	-1,6
t=15	0,028799808	5363,7	-1,6	-0,019834192	-125,3	-2,4
t=30	0,02814011	5171,7	2,0	-0,02538989	-160,3	-3,0
t=45	0,027822342	5080,0	3,8	-0,028711658	-181,2	-3,4
t=60	0,027480685	4982,1	5,6	-0,029775315	-187,9	-3,6
t=75	0,027139932	4885,0	7,5	-0,028384068	-179,1	-3,4
t=90	0,02654174	4716,2	10,7	-0,02765226	-174,5	-3,3
t=105	0,026550808	4718,7	10,6	-0,026511192	-167,3	-3,2
t=120	0,025889479	4534,4	14,1	-0,025862521	-163,2	-3,1
t=121	0,025961055	4554,2	13,7	-0,024596945	-155,3	-2,9
t=135	0,026414945	4680,7	11,3	-0,013273055	-83,9	-1,6
t=150	0,025599178	4454,3	15,6	-0,003650822	-23,1	-0,4
t=165	0,025924644	4544,1	13,9	0,006268644	39,7	0,8
t=180	0,026099918	4592,8	13,0	0,014071918	89,1	1,7
t=195	0,025537014	4437,2	15,9	0,020297014	128,7	2,4
t=210	0,025846986	4522,6	14,3	0,026652986	169,1	3,2
t=225	0,025871849	4529,5	14,2	0,031967849	202,9	3,8
t=240	0,02538889	4396,5	16,7	0,03573289	226,8	4,3
t=255	0,025498027	4426,5	16,1	0,042534027	270,2	5,1
t=270	0,025644808	4466,8	15,4	0,046692808	296,7	5,6
t=285	0,025961849	4554,4	13,7	0,053041849	337,3	6,4
t=300	0,025928589	4545,2	13,9	0,056496589	359,4	6,8
t=315	0,025590808	4452,0	15,7	0,063330808	403,2	7,6
t=330	0,025508466	4429,3	16,1	0,068130466	433,9	8,2
t=345	0,026112397	4596,3	12,9	0,071240397	453,9	8,6

Table A.3 (continued) Absorbance vs Conversion Data of the Bare Cellulose Support Material

t=360	0,02571563	4486,3	15,0	0,07567963	482,4	9,1
t=375	0,025950301	4551,2	13,8	0,080882301	515,8	9,8
t=390	0,025980164	4559,5	13,6	0,084558164	539,5	10,2
t=405	0,026184863	4616,4	12,6	0,088916863	567,5	10,8
t=420	0,026582233	4727,6	10,4	0,091398233	583,5	11,1
t=435	0,026165863	4611,1	12,7	0,095593863	610,6	11,6
t=450	0,026484096	4700,0	11,0	0,101160096	646,5	12,2
t=465	0,026144082	4605,1	12,8	0,103456082	661,4	12,5
t=480	0,026022973	4571,4	13,4	0,107822973	689,6	13,1
t=495	0,026105315	4594,3	13,0	0,112729315	721,4	13,7
t=510	0,026133082	4602,0	12,8	0,116021082	742,7	14,1
t=525	0,026282479	4643,6	12,0	0,120134479	769,4	14,6
t=540	0,026614233	4736,6	10,3	0,123632233	792,1	15,0
t=555	0,026429425	4684,7	11,3	0,127761425	818,9	15,5
t=570	0,026551616	4719,0	10,6	0,131813616	845,3	16,0
t=585	0,026454315	4691,7	11,1	0,134076315	860,0	16,3
t=600	0,026601945	4733,1	10,3	0,139185945	893,3	16,9
t=615	0,026674233	4753,4	10,0	0,139832233	897,5	17,0
t=630	0,026912671	4820,7	8,7	0,147618671	948,3	18,0
t=645	0,026663288	4750,3	10,0	0,150411288	966,6	18,3
t=660	0,027270767	4922,2	6,8	0,152906767	982,9	18,6
t=675	0,026692301	4758,5	9,9	0,158242301	1017,8	19,3
t=690	0,02718163	4896,9	7,2	0,16012363	1030,2	19,5
t=705	0,026838973	4799,8	9,1	0,160476973	1032,5	19,6
t=720	0,027017397	4850,3	8,1	0,167973397	1081,7	20,5
t=721	0,027467397	4978,3	5,7	0,166895397	1074,6	20,4
t=735	0,027312288	4934,1	6,5	0,168570288	1085,6	20,6

Table A.3 (continued) Absorbance vs Conversion Data of the Bare Cellulose Support Material

t=750	0,027353425	4945,8	6,3	0,166953425	1075,0	20,4
t=765	0,027232356	4911,3	7,0	0,168552356	1085,5	20,6
t=780	0,027096397	4872,7	7,7	0,166066397	1069,2	20,3
t=795	0,027079836	4868,0	7,8	0,165603836	1066,1	20,2
t=810	0,027222671	4908,5	7,0	0,167628671	1079,4	20,4
t=825	0,02739174	4956,7	6,1	0,16386974	1054,7	20,0
t=840	0,027109589	4876,4	7,6	0,164531589	1059,1	20,1
t=855	0,027011164	4848,5	8,2	0,166739164	1073,6	20,3
t=870	0,026749685	4774,7	9,6	0,165011685	1062,2	20,1
t=885	0,026614589	4736,7	10,3	0,164862589	1061,3	20,1
t=900	0,027113192	4877,5	7,6	0,163731192	1053,8	20,0
t=915	0,026780589	4783,4	9,4	0,162272589	1044,3	19,8
t=930	0,026771973	4780,9	9,4	0,162285973	1044,4	19,8
t=945	0,02696789	4836,3	8,4	0,16342989	1051,9	19,9
t=960	0,027592068	5014,0	5,0	0,161420068	1038,7	19,7
t=975	0,027260932	4919,4	6,8	0,164064932	1056,0	20,0
t=990	0,027648178	5030,0	4,7	0,160528178	1032,8	19,6
t=1005	0,026928616	4825,2	8,6	0,160142616	1030,3	19,5
t=1020	0,026655753	4748,2	10,1	0,160901753	1035,3	19,6
t=1035	0,027056247	4861,3	7,9	0,160350247	1031,7	19,5
t=1050	0,027077274	4867,3	7,8	0,160477274	1032,5	19,6
t=1065	0,027107548	4875,8	7,6	0,159265548	1024,6	19,4
t=1080	0,026801767	4789,3	9,3	0,157847767	1015,3	19,2
t=1095	0,027282123	4925,5	6,7	0,160418123	1032,1	19,6
t=1110	0,026886479	4813,3	8,8	0,159618479	1026,9	19,5
t=1125	0,026944712	4829,7	8,5	0,160520712	1032,8	19,6
t=1140	0,027098849	4873,4	7,7	0,157758849	1014,7	19,2

Table A.3 (continued) Absorbance vs Conversion Data of the Bare Cellulose Support Material

t=1155	0,026933178	4826,5	8,6	0,159051178	1023,1	19,4
t=1170	0,02686789	4808,0	8,9	0,15698789	1009,6	19,1
t=1185	0,026899589	4817,0	8,8	0,158645589	1020,5	19,3
t=1200	0,026924904	4824,1	8,6	0,157060904	1010,1	19,1
t=1215	0,02648274	4699,7	11,0	0,15578474	1001,8	19,0
t=1230	0,026778932	4782,9	9,4	0,155552932	1000,2	18,9
t=1245	0,026957068	4833,2	8,4	0,155571068	1000,4	18,9
t=1260	0,027076151	4866,9	7,8	0,154506151	993,4	18,8
t=1275	0,027114082	4877,7	7,6	0,152624082	981,1	18,6
t=1290	0,027375014	4951,9	6,2	0,153793014	988,7	18,7
t=1305	0,026847466	4802,2	9,0	0,150911466	969,9	18,4
t=1320	0,026886699	4813,3	8,8	0,152198699	978,3	18,5
t=1335	0,02708911	4870,6	7,7	0,15225111	978,6	18,5
t=1350	0,02699126	4842,9	8,3	0,15180726	975,7	18,5
t=1365	0,027093425	4871,8	7,7	0,152157425	978,0	18,5
t=1380	0,027166164	4892,5	7,3	0,148948164	957,0	18,1

Table A.4 Absorbance vs Conversion Data of the Bare Cellulose Support wo CO

Time (min)	Absorbance CO (cm^{-1})	ppm CO (%5)	Absorbance CO$_2$ (cm^{-1})	ppm CO$_2$
t=1	5,00137E-05	2,3	0,000604014	3,8
t=15	0,000300123	14,5	-0,006221877	-39,3
t=30	0,000312548	15,2	-0,010381452	-65,6
t=45	0,000403151	19,8	-0,012182849	-77,0
t=60	0,000431315	21,2	-0,013654685	-86,3
t=75	-0,000119562	-5,5	-0,012699562	-80,3
t=90	-5,87671E-05	-2,7	-0,011146767	-70,5
t=105	-0,00041226	-18,2	-0,01007826	-63,7
t=120	-0,000265849	-12,0	-0,008887849	-56,2
t=121	-0,000573329	-24,7	-0,007147329	-45,2
t=135	-0,000454767	-20,0	0,003207233	20,3
t=150	0,000245082	11,8	0,013179082	83,5
t=165	-0,000443288	-19,5	0,021608712	137,0
t=180	-0,000335233	-15,0	0,027740767	176,0
t=195	-8,35616E-07	0,0	0,035151164	223,1
t=210	0,00052374	26,1	0,04012374	254,8
t=225	0,000365781	17,9	0,047799781	303,8
t=240	0,000385329	18,9	0,053121329	337,8
t=255	0,000162397	7,7	0,057230397	364,1
t=270	0,00060537	30,4	0,06249137	397,8
t=285	0,000534438	26,6	0,068838438	438,5
t=300	0,000669233	33,9	0,072935233	464,8
t=315	0,000622274	31,3	0,076050274	484,8
t=330	0,000688233	34,9	0,082662233	527,3
t=345	0,000851699	44,0	0,085955699	548,5
t=360	0,000994699	52,3	0,088820699	566,9

Table A.4 (continued) Absorbance vs Conversion Data of the Bare Cellulose Support wo CO

t=375	0,001223438	65,9	0,096523438	616,6
t=390	0,001038274	54,8	0,098058274	626,5
t=405	0,001540918	85,9	0,101910918	651,4
t=420	0,00149537	83,0	0,10423537	666,4
t=435	0,001530644	85,3	0,111306644	712,2
t=450	0,001781575	101,9	0,112983575	723,0
t=465	0,001765685	100,8	0,117653685	753,3
t=480	0,001590986	89,2	0,120246986	770,1
t=495	0,002028123	118,9	0,126298123	809,4
t=510	0,002245575	134,5	0,129503575	830,3
t=525	0,002153918	127,8	0,131685918	844,5
t=540	0,001993068	116,4	0,138523068	889,0
t=555	0,002233644	133,6	0,139199644	893,4
t=570	0,002363466	143,2	0,142525466	915,1
t=585	0,002529466	155,7	0,148047466	951,2
t=600	0,002645288	164,6	0,151917288	976,4
t=615	0,002616151	162,3	0,152058151	977,4
t=630	0,003119425	202,6	0,154603425	994,0
t=645	0,002995411	192,4	0,156823411	1008,6
t=660	0,002922808	186,5	0,163066808	1049,5
t=675	0,002916041	186,0	0,165406041	1064,8
t=690	0,003268836	215,1	0,165948836	1068,4
t=705	0,00323811	212,5	0,16873611	1086,7
t=720	0,003054808	197,3	0,171154808	1102,6
t=721	0,003565699	240,7	0,172649699	1112,4
t=735	0,003198973	209,2	0,175130973	1128,7
t=750	0,003635575	246,9	0,170797575	1100,2

Table A.4 (continued) Absorbance vs Conversion Data of the Bare Cellulose Support wo CO

t=765	0,003578699	241,8	0,170774699	1100,1
t=780	0,003597575	243,5	0,172177575	1109,3
t=795	0,003083712	199,6	0,169023712	1088,6
t=810	0,00334363	221,5	0,16838963	1084,4
t=825	0,003656301	248,7	0,171172301	1102,7
t=840	0,003496822	234,7	0,169632822	1092,6
t=855	0,003283959	216,4	0,168103959	1082,5
t=870	0,003716082	254,0	0,168854082	1087,5
t=885	0,003399986	226,3	0,167265986	1077,0
t=900	0,003727781	255,1	0,168813781	1087,2
t=915	0,003455329	231,1	0,167863329	1081,0
t=930	0,003749562	257,0	0,166997562	1075,3
t=945	0,003551315	239,4	0,166079315	1069,2
t=960	0,003586137	242,5	0,165724137	1066,9
t=975	0,004014932	281,3	0,164192932	1056,9
t=990	0,003799438	261,5	0,167055438	1075,6
t=1005	0,003466767	232,1	0,165872767	1067,9
t=1020	0,003780055	259,8	0,164240055	1057,2
t=1035	0,003868274	267,8	0,164512274	1059,0
t=1050	0,00365437	248,5	0,16406237	1056,0
t=1065	0,003804315	262,0	0,164362315	1058,0
t=1080	0,004438205	321,6	0,163252205	1050,7
t=1095	0,004060986	285,6	0,162088986	1043,1
t=1110	0,004329068	311,0	0,161277068	1037,7
t=1125	0,004137301	292,7	0,162293301	1044,4
t=1140	0,004172808	296,1	0,161572808	1039,7
t=1155	0,004473877	325,1	0,160715877	1034,1

Table A.4 (continued) Absorbance vs Conversion Data of the Bare Cellulose Support wo CO

t=1170	0,004156589	294,6	0,159814589	1028,2
t=1185	0,004294438	307,7	0,160208438	1030,7
t=1200	0,004395384	317,4	0,158859384	1021,9
t=1215	0,004399411	317,8	0,160003411	1029,4
t=1230	0,004719904	349,5	0,159347904	1025,1
t=1245	0,004093493	288,6	0,157679493	1014,2
t=1260	0,004503767	328,0	0,158261767	1018,0
t=1275	0,004200041	298,7	0,156850041	1008,7
t=1290	0,004353562	313,4	0,156235562	1004,7
t=1305	0,004085753	287,9	0,156927753	1009,2
t=1320	0,004329384	311,0	0,157055384	1010,1
t=1335	0,004121479	291,3	0,160077479	1029,9
t=1350	0,004567027	334,2	0,157733027	1014,5
t=1365	0,003946658	275,0	0,159328658	1025,0
t=1380	0,004439096	321,7	0,161013096	1036,0

Table A.5 Absorbance vs Conversion Data of the Catalyst TiO_2/ SiO_2 C_3 wo CO

Time (min)	Absorbance CO (cm^{-1})	ppm CO (%5)	Absorbance CO_2 (cm^{-1})	ppm CO_2
t=1	1,37397E-05	0,6	1,73973E-06	0,0
t=15	5,6726E-05	2,7	-0,004409274	-27,9
t=30	-6,67671E-05	-3,1	-0,009356767	-59,1
t=45	0,000185712	8,9	-0,011418288	-72,2
t=60	3,42192E-05	1,6	-0,010151781	-64,2
t=75	-6,74658E-05	-3,1	-0,011841466	-74,8
t=90	-0,000439836	-19,3	-0,009517836	-60,2
t=105	-0,000319397	-14,3	-0,005063397	-32,0
t=120	-0,000348096	-15,5	-0,003676096	-23,2
t=121	-0,000251452	-11,3	-0,001899452	-12,0
t=135	-0,000427685	-18,8	0,033764315	214,3
t=150	0,000191603	9,2	0,066843603	425,7
t=165	0,000102329	4,8	0,101248329	647,1
t=180	0,000747712	38,2	0,133041712	853,3
t=195	0,000727	37,0	0,161715	1040,6
t=210	0,00138363	75,9	0,19007763	1227,3
t=225	0,001528616	85,1	0,214170616	1386,9
t=240	0,001558274	87,1	0,239284274	1554,5
t=255	0,001945507	113,1	0,260235507	1695,2
t=270	0,002477356	151,7	0,281783356	1840,8
t=285	0,00219074	130,5	0,30288674	1984,3
t=300	0,002604699	161,4	0,321996699	2115,1
t=315	0,003122164	202,8	0,342504164	2256,3
t=330	0,003124219	203,0	0,363964219	2405,1
t=345	0,00286763	182,1	0,38203763	2531,3
t=360	0,003275479	215,7	0,397555479	2640,2

Table A.5 (continued) Absorbance vs Conversion Data of the Catalyst TiO_2/ SiO_2 C_3 wo CO

t=375	0,003217699	210,8	0,419309699	2793,9
t=390	0,004065315	286,0	0,434891315	2904,6
t=405	0,003820945	263,5	0,452116945	3027,8
t=420	0,003899562	270,7	0,467875562	3141,2
t=435	0,004338836	312,0	0,486322836	3274,7
t=450	0,004580493	335,6	0,504646493	3408,3
t=465	0,00512789	391,4	0,52030789	3523,1
t=480	0,005050329	383,3	0,530022329	3594,7
t=495	0,005337603	413,7	0,544793603	3704,1
t=510	0,005045699	382,8	0,555923699	3786,9
t=525	0,005567014	438,6	0,572471014	3910,7
t=540	0,005858658	471,0	0,587180658	4021,4
t=555	0,006157452	505,2	0,593857452	4071,9
t=570	0,006441479	538,6	0,613969479	4224,7
t=585	0,006795986	581,4	0,626989986	4324,4
t=600	0,006811425	583,3	0,642117425	4440,8
t=615	0,006779411	579,3	0,651223411	4511,2
t=630	0,007263726	639,9	0,669253726	4651,4
t=645	0,007409151	658,5	0,676939151	4711,5
t=660	0,007717918	698,8	0,692447918	4833,3
t=675	0,007767507	705,4	0,695675507	4858,8
t=690	0,008181	761,1	0,715303	5014,3
t=705	0,008415493	793,4	0,738837493	5202,6
t=720	0,008686726	831,5	0,737018726	5188,0
t=721	0,008219534	766,3	0,744281534	5246,4
t=735	0,008402685	791,6	0,736524685	5184,0
t=750	0,008287699	775,7	0,734887699	5170,9

Table A.5 (continued) Absorbance vs Conversion Data of the Catalyst TiO_2/ SiO_2 C_3 wo CO

t=765	0,008294507	776,6	0,742658507	5233,3
t=780	0,008567986	814,7	0,729207986	5125,3
t=795	0,008734959	838,3	0,723190959	5077,2
t=810	0,008277397	774,3	0,719839397	5050,5
t=825	0,008515658	807,4	0,720119658	5052,7
t=840	0,008229918	767,8	0,719611918	5048,7
t=855	0,008510342	806,6	0,722404342	5070,9
t=870	0,008334123	782,1	0,714620123	5008,9
t=885	0,008383452	788,9	0,717197452	5029,4
t=900	0,008239575	769,1	0,709467575	4967,9
t=915	0,008193082	762,7	0,706557082	4944,9
t=930	0,008695685	832,8	0,702431685	4912,2
t=945	0,008606986	820,2	0,707654986	4953,6
t=960	0,008133205	754,5	0,713805205	5002,4
t=975	0,008427342	795,0	0,705077342	4933,1
t=990	0,008693342	832,4	0,707291342	4950,7
t=1005	0,008765671	842,7	0,705623671	4937,5
t=1020	0,008693274	832,4	0,702553274	4913,1
t=1035	0,008618493	821,8	0,694126493	4846,6
t=1050	0,008425452	794,8	0,702237452	4910,6
t=1065	0,008722329	836,5	0,693388329	4840,7
t=1080	0,009034411	881,4	0,696550411	4865,7
t=1095	0,009016945	878,9	0,697336945	4871,9
t=1110	0,008394123	790,4	0,683492123	4762,9
t=1125	0,008201164	763,8	0,693269164	4839,8
t=1140	0,008789137	846,1	0,687035137	4790,7
t=1155	0,008534288	810,0	0,674704288	4694,0

Table A.5 (continued) Absorbance vs Conversion Data of the Catalyst TiO_2/ SiO_2 C_3 wo CO

t=1170	0,008336205	782,4	0,686946205	4790,0
t=1185	0,008180863	761,0	0,685498863	4778,6
t=1200	0,008628068	823,2	0,683368068	4761,9
t=1215	0,008496329	804,7	0,691982329	4829,7
t=1230	0,00858489	817,1	0,68282689	4757,6
t=1245	0,008890384	860,6	0,678348384	4722,5
t=1260	0,008626603	823,0	0,679980603	4735,3
t=1275	0,008619384	822,0	0,672199384	4674,4
t=1290	0,008506027	806,0	0,669446027	4652,9
t=1305	0,00875789	841,6	0,67925189	4729,6
t=1320	0,009058493	884,9	0,671562493	4669,4
t=1335	0,009082493	888,4	0,667750493	4639,7
t=1350	0,008725548	837,0	0,670241548	4659,1
t=1365	0,008786986	845,8	0,664052986	4610,8
t=1380	0,008913082	863,8	0,667057082	4634,3

Table A.6 Absorbance vs Conversion Data of the Bare 304 Stainless Steel Wire Mesh Material Under UVC

Time (min)	Absorbance CO (cm^{-1})	ppm CO (%5)	CO Conv (%)	Absorbance CO_2 (cm^{-1})	ppm CO_2	CO_2 Conv (%)
t=1	0,025764808	4499,9	0,0	-0,006401192	-40,5	-0,9
t=15	0,025766534	4500,4	0,0	-0,004505466	-28,5	-0,6
t=30	0,025357055	4387,8	2,5	-0,003914945	-24,8	-0,6
t=45	0,025077247	4311,4	4,2	-0,002688753	-17,0	-0,4
t=60	0,02430763	4103,8	8,8	-0,00184237	-11,7	-0,3
t=61	0,024392438	4126,5	8,3	-0,002399562	-15,2	-0,3
t=75	0,024837616	4246,4	5,6	0,001899616	12,0	0,3
t=90	0,025029411	4298,4	4,5	0,003435411	21,7	0,5
t=105	0,024738548	4219,6	6,2	0,004252548	26,9	0,6
t=120	0,024231836	4083,6	9,3	0,005987836	37,9	0,8
t=135	0,023784904	3964,9	11,9	0,007522904	47,6	1,1
t=150	0,02419011	4072,5	9,5	0,01037211	65,7	1,5
t=165	0,024511863	4158,6	7,6	0,011475863	72,7	1,6
t=180	0,02438463	4124,4	8,3	0,01236863	78,3	1,7
t=195	0,024352123	4115,7	8,5	0,012626123	80,0	1,8
t=210	0,024205082	4076,5	9,4	0,015607082	98,9	2,2
t=225	0,024405397	4130,0	8,2	0,016321397	103,4	2,3
t=240	0,023815753	3973,1	11,7	0,018279753	115,8	2,6
t=255	0,023850562	3982,3	11,5	0,019358562	122,7	2,7
t=270	0,024329945	4109,8	8,7	0,020961945	132,9	3,0
t=285	0,024081644	4043,6	10,1	0,021737644	137,8	3,1
t=300	0,024140877	4059,3	9,8	0,021984877	139,4	3,1
t=315	0,024396589	4127,7	8,3	0,023774589	150,8	3,4
t=330	0,024522247	4161,4	7,5	0,024460247	155,1	3,4

Table A.6 (continued) Absorbance vs Conversion Data of the Bare 304 Stainless Steel Wire Mesh Material Under UVC

t=345	0,024043493	4033,4	10,4	0,027937493	177,2	3,9
t=360	0,023704726	3943,8	12,4	0,026488726	168,0	3,7
t=375	0,023838603	3979,1	11,6	0,026774603	169,8	3,8
t=390	0,024342521	4113,2	8,6	0,027520521	174,6	3,9
t=405	0,024024055	4028,3	10,5	0,029300055	185,9	4,1
t=420	0,024278493	4096,1	9,0	0,030172493	191,4	4,3
t=435	0,023870603	3987,6	11,4	0,032424603	205,8	4,6
t=450	0,024255055	4089,8	9,1	0,032711055	207,6	4,6
t=465	0,024271726	4094,2	9,0	0,033791726	214,5	4,8
t=480	0,024261671	4091,6	9,1	0,034233671	217,3	4,8
t=495	0,02417374	4068,1	9,6	0,03589574	227,9	5,1
t=510	0,024268795	4093,5	9,0	0,039044795	247,9	5,5
t=525	0,024225438	4081,9	9,3	0,038945438	247,3	5,5
t=540	0,023858945	3984,5	11,5	0,039822945	252,9	5,6
t=555	0,024183315	4070,6	9,5	0,040707315	258,5	5,7
t=570	0,024397027	4127,8	8,3	0,042969027	273,0	6,1

Table A.7 Absorbance vs Conversion Data for TiO_2/SiO_2 C_3

Time (min)	Absorbance CO (cm^{-1})	ppm CO (%5)	CO Conv (%)	Absorbance CO_2 (cm^{-1})	ppm CO_2	CO_2 Conv (%)
t=1	0,027960932	5120,0	0,0	-0,005501068	-34,8	-0,7
t=15	0,027963699	5120,8	0,0	-0,006884301	-43,5	-0,9
t=30	0,028227589	5197,0	-1,5	-0,003828411	-24,2	-0,5
t=45	0,027321644	4936,7	3,6	-0,000284356	-1,8	0,0
t=60	0,028173808	5181,5	-1,2	0,000609808	3,9	0,1
t=75	0,027382466	4954,1	3,2	0,003696466	23,4	0,5
t=90	0,02618937	4617,7	9,8	0,00773137	48,9	1,0
t=105	0,026664438	4750,7	7,2	0,010584438	67,0	1,3
t=120	0,026074397	4585,7	10,4	0,014888397	94,3	1,8
t=121	0,026657685	4748,8	7,2	0,019283685	122,2	2,4
t=135	0,026553452	4719,5	7,8	0,057681452	367,0	7,2
t=150	0,026698616	4760,3	7,0	0,093866616	599,4	11,7
t=165	0,026994219	4843,7	5,4	0,126308219	809,5	15,8
t=180	0,026480658	4699,1	8,2	0,153408658	986,2	19,3
t=195	0,02707837	4867,6	4,9	0,18418237	1188,3	23,2
t=210	0,026780685	4783,4	6,6	0,205366685	1328,4	25,9
t=225	0,027244685	4914,8	4,0	0,234376685	1521,6	29,7
t=240	0,026979397	4839,5	5,5	0,255807397	1665,4	32,5
t=255	0,02725637	4918,1	3,9	0,27835237	1817,5	35,5
t=270	0,027857658	5090,2	0,6	0,301497658	1974,8	38,6
t=285	0,027453918	4974,5	2,8	0,320271918	2103,3	41,1
t=300	0,027690644	5042,2	1,5	0,336548644	2215,2	43,3
t=315	0,028282301	5212,9	-1,8	0,358270301	2365,6	46,2
t=330	0,028205589	5190,7	-1,4	0,375995589	2489,0	48,6
t=345	0,027695932	5043,7	1,5	0,390053932	2587,5	50,5

Table A.7 (continued) Absorbance vs Conversion Data for TiO_2/SiO_2 C_3

t=360	0,027872603	5094,5	0,5	0,412300603	2744,2	53,6
t=375	0,028275644	5211,0	-1,8	0,420227644	2800,4	54,7
t=390	0,028311425	5221,3	-2,0	0,445493425	2980,4	58,2
t=405	0,028728849	5342,9	-4,4	0,453046849	3034,5	59,3
t=420	0,028647027	5319,0	-3,9	0,471823027	3169,7	61,9
t=435	0,028524219	5283,2	-3,2	0,489804219	3300,0	64,5
t=450	0,02866926	5325,5	-4,0	0,50519126	3412,2	66,6
t=465	0,028609014	5307,9	-3,7	0,517703014	3504,0	68,4
t=480	0,02894174	5405,3	-5,6	0,53403774	3624,4	70,8
t=495	0,028853055	5379,3	-5,1	0,552997055	3765,1	73,5
t=510	0,029126137	5459,4	-6,6	0,568870137	3883,7	75,9
t=525	0,029114562	5456,0	-6,6	0,586820562	4018,7	78,5
t=540	0,029259589	5498,8	-7,4	0,600135589	4119,5	80,5
t=555	0,029840452	5671,0	-10,8	0,608262452	4181,3	81,7
t=570	0,029564712	5589,0	-9,2	0,619362712	4265,9	83,3
t=585	0,02951637	5574,7	-8,9	0,63356237	4374,9	85,4
t=600	0,029584836	5595,0	-9,3	0,655448836	4543,9	88,7
t=615	0,029957192	5705,8	-11,4	0,661215192	4588,8	89,6
t=630	0,030108452	5751,0	-12,3	0,670840452	4663,8	91,1
t=645	0,029737164	5640,2	-10,2	0,695035164	4853,7	94,8
t=660	0,030427644	5846,7	-14,2	0,703507644	4920,7	96,1
t=675	0,030163027	5767,3	-12,6	0,718755027	5041,8	98,5
t=690	0,030711959	5932,3	-15,9	0,735739959	5177,7	101,1
t=705	0,030431712	5847,9	-14,2	0,742051712	5228,4	102,1
t=720	0,030467041	5858,5	-14,4	0,755853041	5339,9	104,3
t=721	0,030233452	5788,4	-13,1	0,761277452	5383,9	105,2
t=735	0,030457973	5855,8	-14,4	0,757239973	5351,1	104,5
t=750	0,030348233	5822,8	-13,7	0,747668233	5273,7	103,0

Table A.7 (continued) Absorbance vs Conversion Data for TiO_2/SiO_2 C_3

t=765	0,03034489	5821,8	-13,7	0,74884689	5283,2	103,2
t=780	0,030281137	5802,7	-13,3	0,746977137	5268,1	102,9
t=795	0,02985574	5675,5	-10,9	0,74643774	5263,8	102,8
t=810	0,030343329	5821,3	-13,7	0,742927329	5235,5	102,3
t=825	0,029947082	5702,7	-11,4	0,744957082	5251,8	102,6
t=840	0,030550959	5883,8	-14,9	0,741430959	5223,4	102,0
t=855	0,030183589	5773,4	-12,8	0,739553589	5208,3	101,7
t=870	0,029988781	5715,2	-11,6	0,740000781	5211,9	101,8
t=885	0,029352205	5526,1	-7,9	0,734742205	5169,7	101,0
t=900	0,030077603	5741,7	-12,1	0,735119603	5172,7	101,0
t=915	0,029558219	5587,1	-9,1	0,725036219	5092,0	99,5
t=930	0,030082452	5743,2	-12,2	0,726104452	5100,5	99,6
t=945	0,029246986	5495,1	-7,3	0,727302986	5110,1	99,8
t=960	0,029844808	5672,3	-10,8	0,728216808	5117,4	99,9
t=975	0,029698397	5628,7	-9,9	0,723616397	5080,6	99,2
t=990	0,029241575	5493,5	-7,3	0,729059575	5124,1	100,1
t=1005	0,02984311	5671,7	-10,8	0,72406511	5084,2	99,3
t=1020	0,029576863	5592,6	-9,2	0,726012863	5099,8	99,6
t=1035	0,029401452	5540,7	-8,2	0,724181452	5085,1	99,3
t=1050	0,029555301	5586,2	-9,1	0,722389301	5070,8	99,0
t=1065	0,029155685	5468,1	-6,8	0,723457685	5079,3	99,2
t=1080	0,029614205	5603,7	-9,4	0,719868205	5050,7	98,6
t=1095	0,029613219	5603,4	-9,4	0,710211219	4973,9	97,1
t=1110	0,029145753	5465,2	-6,7	0,726547753	5104,0	99,7
t=1125	0,029780014	5653,0	-10,4	0,719262014	5045,9	98,6
t=1140	0,029544877	5583,1	-9,0	0,715714877	5017,6	98,0
t=1155	0,029926247	5696,5	-11,3	0,723020247	5075,9	99,1
t=1170	0,029785479	5654,6	-10,4	0,717063479	5028,3	98,2

Table A.7 (continued) Absorbance vs Conversion Data for TiO_2/SiO_2 C_3

t=1185	0,029129219	5460,4	-6,6	0,706363219	4943,3	96,6
t=1200	0,029422616	5546,9	-8,3	0,714852616	5010,7	97,9
t=1215	0,02985711	5675,9	-10,9	0,71287111	4995,0	97,6
t=1230	0,029444959	5553,5	-8,5	0,706686959	4945,9	96,6
t=1245	0,02955874	5587,2	-9,1	0,71432274	5006,5	97,8
t=1260	0,029501068	5570,2	-8,8	0,708909068	4963,5	96,9
t=1275	0,029733356	5639,1	-10,1	0,702031356	4909,0	95,9
t=1290	0,029356644	5527,4	-8,0	0,705224644	4934,3	96,4
t=1305	0,029374932	5532,8	-8,1	0,705774932	4938,7	96,5
t=1320	0,029569329	5590,4	-9,2	0,694941329	4853,0	94,8
t=1335	0,029638192	5610,8	-9,6	0,697066192	4869,8	95,1
t=1350	0,029425534	5547,8	-8,4	0,698155534	4878,4	95,3
t=1365	0,029225945	5488,8	-7,2	0,702707945	4914,4	96,0
t=1380	0,029487699	5566,2	-8,7	0,695191699	4855,0	94,8

Table A.8 Absorbance vs Conversion Data of Catalyst wo Calcination

Time (min)	Absorbance CO (cm^{-1})	ppm CO (%5)	CO Conv (%)	Absorbance CO_2 (cm^{-1})	ppm CO_2	CO_2 Conv (%)
t=1	0,026434247	4686,1	0,0	-0,008945753	-56,6	-1,2
t=15	0,025683411	4477,5	4,5	-0,008102589	-51,2	-1,1
t=30	0,025786795	4506,0	3,8	-0,011423205	-72,2	-1,5
t=45	0,024976932	4284,2	8,6	-0,012029068	-76,0	-1,6
t=60	0,024889288	4260,4	9,1	-0,009758712	-61,7	-1,3
t=61	0,024889288	4260,4	9,1	-0,009758712	-61,7	-1,3
t=75	0,024213808	4078,8	13,0	0,018709808	118,6	2,5
t=90	0,02402089	4027,4	14,1	0,04729089	300,6	6,4
t=105	0,023808918	3971,3	15,3	0,071956918	458,5	9,8
t=120	0,024101384	4048,8	13,6	0,098449384	629,0	13,4
t=135	0,024004836	4023,2	14,1	0,122742836	786,3	16,8
t=150	0,023770959	3961,2	15,5	0,144150959	925,7	19,8
t=165	0,023339712	3847,9	17,9	0,166937712	1074,9	22,9
t=180	0,02402826	4029,4	14,0	0,18861026	1217,6	26,0
t=195	0,023395945	3862,6	17,6	0,207949945	1345,6	28,7
t=210	0,023374247	3857,0	17,7	0,225976247	1465,5	31,3
t=225	0,023488699	3886,9	17,1	0,247012699	1606,3	34,3
t=240	0,023753507	3956,6	15,6	0,262331507	1709,3	36,5
t=255	0,024076288	4042,1	13,7	0,283320288	1851,2	39,5
t=270	0,023376301	3857,5	17,7	0,301746301	1976,5	42,2
t=285	0,024081822	4043,6	13,7	0,318967822	2094,3	44,7
t=300	0,023421534	3869,3	17,4	0,333179534	2192,0	46,8
t=315	0,023745219	3954,4	15,6	0,355759219	2348,1	50,1
t=330	0,024380315	4123,3	12,0	0,372928315	2467,6	52,7
t=345	0,023948973	4008,3	14,5	0,387458973	2569,3	54,8

Table A.8 (continued) Absorbance vs Conversion Data of Catalyst wo Calcination.

t=360	0,024083767	4044,1	13,7	0,405949767	2699,4	57,6
t=375	0,024076082	4042,1	13,7	0,419070082	2792,2	59,6
t=390	0,024459808	4144,6	11,6	0,437873808	2925,9	62,4
t=405	0,024514247	4159,2	11,2	0,452744247	3032,3	64,7
t=420	0,024411479	4131,6	11,8	0,464793479	3119,0	66,6
t=435	0,02506437	4307,9	8,1	0,48477837	3263,5	69,6
t=450	0,025105082	4319,0	7,8	0,507927082	3432,3	73,2
t=465	0,025064315	4307,9	8,1	0,515856315	3490,4	74,5
t=480	0,025259973	4361,3	6,9	0,539259973	3663,0	78,2
t=495	0,025070301	4309,6	8,0	0,550816301	3748,9	80,0
t=510	0,024841521	4247,5	9,4	0,561481521	3828,4	81,7
t=525	0,025470521	4418,9	5,7	0,584972521	4004,8	85,5
t=540	0,025510603	4429,9	5,5	0,590830603	4049,0	86,4
t=555	0,025778863	4503,8	3,9	0,618270863	4257,6	90,9
t=570	0,02586511	4527,6	3,4	0,61565111	4237,6	90,4

Table A.9 Absorbance vs Conversion Data of Catalyst TiO_2/SiO_2 S_2 with Calc.

Time (min)	Absorbance CO (cm^{-1})	ppm CO (%5)	CO Conv (%)	Absorbance CO_2 (cm^{-1})	ppm CO_2	CO_2 Conv (%)
t=1	0,026430137	4684,9	0,0	-0,006845863	-43,3	-0,9
t=15	0,025888479	4534,1	3,2	-0,006395521	-40,4	-0,9
t=30	0,025319603	4377,6	6,6	-0,005360397	-33,9	-0,7
t=45	0,02556737	4445,5	5,1	-0,00491463	-31,1	-0,7
t=60	0,025595397	4453,2	4,9	-0,004530603	-28,7	-0,6
t=61	0,025260055	4361,3	6,9	-0,002979945	-18,8	-0,4
t=75	0,025411685	4402,8	6,0	0,012311685	78,0	1,7
t=90	0,024762904	4226,2	9,8	0,029434904	186,7	4,0
t=105	0,025074548	4310,7	8,0	0,044792548	284,6	6,1
t=120	0,025150411	4331,4	7,5	0,058730411	373,7	8,0
t=135	0,024930233	4271,5	8,8	0,069094233	440,1	9,4
t=150	0,024613	4185,8	10,7	0,080621	514,1	11,0
t=165	0,024798096	4235,7	9,6	0,087604096	559,1	11,9
t=180	0,02440811	4130,7	11,8	0,09648611	616,3	13,2
t=195	0,024995329	4289,2	8,4	0,103107329	659,1	14,1
t=210	0,024647918	4195,2	10,5	0,111483918	713,3	15,2
t=225	0,024796836	4235,4	9,6	0,117668836	753,4	16,1
t=240	0,024962041	4280,1	8,6	0,123940041	794,1	17,0
t=255	0,024866342	4254,2	9,2	0,130896342	839,3	17,9
t=270	0,024675973	4202,8	10,3	0,135641973	870,2	18,6
t=285	0,024970603	4282,5	8,6	0,141268603	906,9	19,4
t=300	0,024386671	4125,0	12,0	0,146244671	939,4	20,1
t=315	0,024524438	4162,0	11,2	0,152948438	983,2	21,0
t=330	0,024136493	4058,2	13,4	0,157992493	1016,2	21,7
t=345	0,024305959	4103,4	12,4	0,162455959	1045,5	22,3

Table A.9 (continued) Absorbance vs Conversion Data of Catalyst TiO_2/SiO_2 S_2 with Calc.

t=360	0,024717658	4214,0	10,1	0,165255658	1063,8	22,7
t=375	0,024539808	4166,1	11,1	0,171407808	1104,2	23,6
t=390	0,024959836	4279,5	8,7	0,176187836	1135,7	24,2
t=405	0,024723671	4215,6	10,0	0,179901671	1160,1	24,8
t=420	0,024411726	4131,7	11,8	0,182913726	1180,0	25,2
t=435	0,024599178	4182,1	10,7	0,186335178	1202,5	25,7
t=450	0,024587384	4178,9	10,8	0,194011384	1253,2	26,8
t=465	0,024605877	4183,9	10,7	0,193759877	1251,6	26,7
t=480	0,024492836	4153,5	11,3	0,199076836	1286,8	27,5
t=495	0,024208	4077,2	13,0	0,201118	1300,3	27,8
t=510	0,024588534	4179,2	10,8	0,206046534	1333,0	28,5
t=525	0,02430363	4102,8	12,4	0,20861763	1350,0	28,8
t=540	0,024136521	4058,2	13,4	0,213508521	1382,5	29,5
t=555	0,024365863	4119,4	12,1	0,218117863	1413,2	30,2
t=570	0,024738205	4219,5	9,9	0,225404205	1461,7	31,2

B. Catalyst Loading Work on Stainless Steel Wire Mesh Substrate

In order to get the proper amount of the catalyst, different methodologies have been followed to increase the catalyst loading. The following parameters has been tried for this purpose.

- Increasing The Number of Immersion
- Increasing the Time of the Mixing of the Sol
- Drying in between the Coatings

In conclusion, independent from the pretreatment and withdrawal rate, increasing the gelation time (mixing of the sol), increases the amount of the catalyst reached. Intermediate drying in each of the steps also a key step for a thicker film in the end.

The cumulative coating for some resembles samples are given in the graph below as Figure B.1 and Figure B.2.

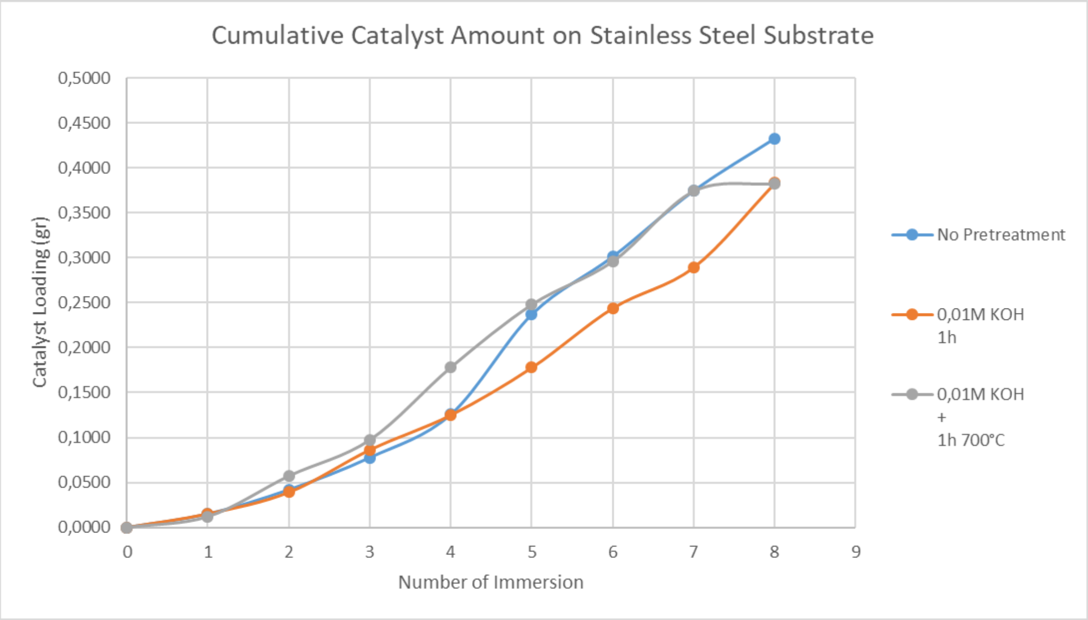

Figure B.1 Cumulative Catalyst Amount on Stainless Steel Substrate

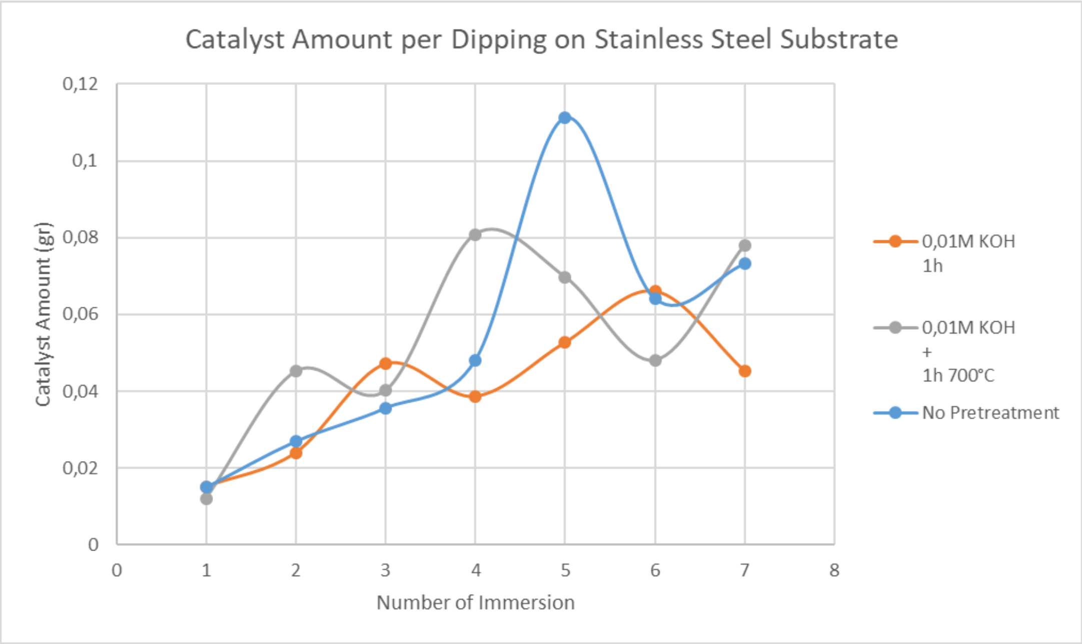

Figure B.2 Catalyst Amount per Dipping

Table B.1 Catalyst Loading Study

Sample No	Name	Pretreatment of The Substrate	Number of Immersion	Sol-Gel Mixing Time	Dipping Rate (In Equip.)	Withdrawal Rate (in Equip.)	Drying Time (mins) @100°C	Total Weight of The Catalyst with Support (gr)	Weight of Coating per Immersion (gr)	Cumulative Total Catalyst Amount (gr)	Total Catalyst Amount (gr)	Catalyst Loading (gr/cm^2)
1	**TiO$_2$/SiO$_2$ S_NP_1**	No Pretreatment	0 Bare	-	-	-	-	0,4995	0	0,0000	0,4325	0,026
			1 Coating	overnight	20	2	60	0,5145	0,015	0,0150		
			2 Coating	9days	20	2	45	0,5415	0,027	0,0420		
			3 Coating	9days	20	2	45	0,5772	0,0357	0,0777		
			4 Coating	9days	20	2	45	0,6253	0,0481	0,1258		
			5 Coating	9days	20	20	45	0,7365	0,1112	0,2370		
			6 Coating	9days	20	20	45	0,8007	0,0642	0,3012		
			7 Coating	9days	20	20	45	0,8739	0,0732	0,3744		
			8 Coating	9days	20	20	overnight	0,932	0,058	0,4325		
2	**TiO2/SiO$_2$ S_AP_2**	0,01M KOH 1h	0 Bare	-	-	-	-	0,4965	0	0,0000	0,383	0,023
			1 Coating	overnight	20	2	60	0,5116	0,0151	0,0151		
			2 Coating	9days	20	2	45	0,5356	0,024	0,0391		
			3 Coating	9days	20	2	45	0,5828	0,0472	0,0863		
			4 Coating	9days	20	2	45	0,6215	0,0387	0,1250		
			5 Coating	9days	20	20	45	0,6743	0,0528	0,1778		
			6 Coating	9days	20	20	45	0,7405	0,0662	0,2440		
			7 Coating	9days	20	20	45	0,7859	0,0454	0,2894		
			8 Coating	9days	20	20	overnight	0,8795	0,094	0,3830		
3	**TiO2/SiO$_2$ S_APT_3**	0,01M KOH + 1h 700°C	0 Bare	-	-	-	-	0,5068	0	0,0000	0,3827	0,023
			1 Coating	overnight	20	2	60	0,5189	0,0121	0,0121		
			2 Coating	9days	20	2	45	0,5641	0,0452	0,0573		
			3 Coating	9days	20	2	45	0,6043	0,0402	0,0975		
			4 Coating	9days	20	2	45	0,6852	0,0809	0,1784		
			5 Coating	9days	20	20	45	0,755	0,0698	0,2482		
			6 Coating	9days	20	20	45	0,8031	0,0481	0,2963		
			7 Coating	9days	20	20	45	0,8812	0,0781	0,3744		
			8 Coating	9days	20	20	overnight	0,8895	0,008	0,3827		